$\Upsilon(nS)$ Cross Section Measurement in pp collisions at $\sqrt{s} = 7$ TeV with the CMS Detector

Bora Akgün

Department of Physics

Carnegie Mellon University

A thesis submitted for the degree of

Doctor of Philosophy

February 2012

Abstract

The Υ production cross sections are measured with the CMS detector using 36.7 ± 1.5 pb^{-1} of proton-proton collisions at $\sqrt{s} = 7$ TeV. The observed yields of the $\Upsilon(1S)$, $\Upsilon(2S)$, and $\Upsilon(3S)$ reconstructed in the di-muon decay channel are: 73569 ± 465, 23390 ± 364, and 13359 ± 130, respectively. Integrated over the rapidity range $|y| \leq 2.4$, the product of the $\Upsilon(nS)$ production cross section (unpolarized scenario) and the di-muon branching ratio are measured to be

$$\sigma(pp \to \Upsilon(1S)X) \cdot \mathcal{B}(\Upsilon(1S) \to \mu^+\mu^-) =$$
$$8.347 \pm 0.056 \text{ (stat.) } {}^{+0.365}_{-0.350} \text{ (syst.)} \pm 0.334 \text{ (lumi.) nb}\,, \tag{1}$$
$$\sigma(pp \to \Upsilon(2S)X) \cdot \mathcal{B}(\Upsilon(2S) \to \mu^+\mu^-) =$$
$$2.274 \pm 0.034 \text{ (stat.) } {}^{+0.138}_{-0.130} \text{ (syst.)} \pm 0.086 \text{ (lumi.) nb}\,, \tag{2}$$
$$\sigma(pp \to \Upsilon(3S)X) \cdot \mathcal{B}(\Upsilon(3S) \to \mu^+\mu^-) =$$
$$1.175 \pm 0.021 \text{ (stat.) } {}^{+0.101}_{-0.098} \text{ (syst.)} \pm 0.046 \text{ (lumi.) nb}\,. \tag{3}$$

where the first uncertainty is statistical, the second is systematic, and the third is associated with the estimation of the integrated luminosity of the data sample. The cross sections are obtained assuming unpolarized-Υ production. Assuming fully transverse or fully longitudinal polarization leads to variations in the cross sections by about 20%. The $\Upsilon(1S)$, $\Upsilon(2S)$, and $\Upsilon(3S)$ differential cross sections in transverse momentum and rapidity, along with respective cross section ratios, are presented. Comparison to theory predictions and previous experimental measurements are provided.

Acknowledgements

There are a lot of people whose help made my time in graduate school pleasant and this thesis possible. It is not possible to acknowledge everyone, but a few deserve special thanks.

First of all, I'd like to thank my advisor Prof. Thomas Ferguson for his guidance, support, good judgement and professionalism. Throughout the time we've worked together, he has maintained a balance between guiding me and allowing me independence. I thank him for being involved and supportive.

I sincerely thank Dr. Urs Langenegger who helped me getting started with the analysis and guided me throughout the way. I truly appreciate his help, advice and friendship. I'm definitely going to miss the PSI visits I had during my Ph.D..

I would like to thank Prof. Helmut Vogel and Prof. Manfred Paulini who have always been there for physics/non-physics conversations. I also thank them for being in my thesis committee.

I would like to thank my office-mate Dr. Igor Vorobiev not only for his kindness and patience but also for his ability to get things done at CERN.

On the personal side, I would like to thank my many friends both in Pittsburgh and Geneva. In particular, I thank my fellow CMU graduate student friend Ryan Carroll for always putting a smile on my face. I thank my friends in Pittsburgh for dragging me away from what I was working on and forcing me to enjoy life. I also thank my friends in Geneva for making life bearable when things went hectic at CERN.

Lastly, I thank my parents and sister for their infinite support and encouragement.

Contents

List of Figures

List of Tables

Chapter 1

Introduction

The era of heavy quarkonia started with the discoveries of the J/ψ resonance in November 1974 at BNL [17] and SLAC [18]. The J/ψ is the second-lowest-mass particle in the $c\bar{c}$ system, the bound states of which are named "charmonium".

In 1977, a new heavy-quark resonance Υ(Upsilon) was discovered at Fermilab [19]. The $\Upsilon(1S)$ resonance is similarly the second-lowest-mass particle in the $b\bar{b}$ system; the $b\bar{b}$ bound states are named "bottomonium". The 2S and 3S states were found soon thereafter [20] at Fermilab. The 4S state was discovered at the Cornell e^+e^- storage ring (CESR) with the CLEO detector [21], and from its width, was determined to be above the threshold for the production of $B\bar{B}$ mesons.

Even though it has been more than 30 years since its discovery, the production mechanisms of quarkonia in hadronic environments are not well understood. The existing theories fail to reproduce both the differential cross section and the polarization measurements of the charmonium and bottomonium states. Most recently, the Υ resonances cross sections have been measured at the Tevatron at center-of-mass energies of $\sqrt{s} = 1.8$ TeV and $\sqrt{s} = 1.96$ TeV by the CDF [3] and D0 [2] experiments. Studying quarkonium production at higher center-of-mass energies could elucidate our understanding of the process. The Υ resonance measurements are particularly important, since the theoretical calculations for bottomonium are more robust than for charmonium, because of the higher mass of the bottom quark compared to the charm quark and the absence of b-hadron feed-down.

The Large Hadron Collider (LHC) is a proton-proton collider that has been designed to operate at a center-of-mass energy of up to $\sqrt{s} = 14$ TeV. The LHC became operational in December 2009, and after short runs of data taking at center-of-mass energies of 900 GeV and 2.36 TeV, the LHC began to deliver collisions with a center-of-mass energy of 7 TeV.

The Compact Muon Solenoid (CMS) detector is designed for high transverse-momentum (p_T) physics, but it is also very well suited to quarkonia physics, thanks to its muon system, which has the potential to identify low-momentum muons from high-mass quarkonia resonances (J/ψ, Υ, ...), and the excellent inner tracking detectors. Measuring the Υ resonances production cross sections with CMS will allow important tests of several theories, including non-relativistic quantum chromodynamics [22] (QCD). These measurements also allow the calibration of the detector for low-p_T muons.

In this thesis, inclusive production cross sections of the Υ resonances have been measured, using data collected by the CMS detector in the 2010 LHC run. The $\Upsilon(nS) \rightarrow \mu^+\mu^-$ decay channels are used. The theoretical framework for the cross-section measurement is introduced in Chapter 2, which includes a review of the main ideas of QCD, its application to hadronic collisions, and a brief overview of quarkonia physics. Chapter 3 gives an overview of the LHC and the CMS experiment. Chapter 4 introduces the Monte Carlo event generators used in the analysis. Chapter 5 describes the CMS trigger system, the trigger scheme that is used for Υ selection, and the data samples used in the analysis. Chapter 6 explains the analysis procedure, including details of the muon and Υ reconstruction performance and efficiency studies. The determination of various systematical uncertainties are presented in Chapter 7. The final results are given in Chapter 8. Chapter 9 compares the results with the theoretical expectations and measurements from other experiments. A summary and conclusions are given in Chapter 10.

The results that are presented in this thesis are not official CMS measurements. CMS has published Υ cross sections with the first 3 pb^{-1} of data, and will have a publication using these data and the results that are presented in this thesis will be used as a cross-check.

Chapter 2

Theoretical Motivations

This chapter begins with a brief summary of the Standard Model of particle physics. It continues with the properties of $b\bar{b}$ states. An introduction to the production mechanism of bottomonium is then presented. The chapter concludes with a summary of past measurements on bottomonium from different experiments, and their comparison with theoretical models.

2.1 Standard Model

The Standard Model (SM) [23] is an effective field theory comprising both quantum mechanics and special relativity. It describes three of the four known forces, excluding gravity, namely: the strong, the electromagnetic, and the weak forces. Both the building blocks of matter, fermions, and the force mediators, bosons, are described by the SM. Gluons are the mediators of the strong force, photons for the electromagnetic, and the W and Z for the weak force.

The SM incorporates the unified theory of the electroweak interaction, which describes the weak and electromagnetic interactions, and quantum chromodynamics, which describes the strong interaction. These are gauge field theories describing the coupling of fermions to bosons, with bosons mediating the forces between fermions.

The spin-$\frac{1}{2}$ fermions are divided into two categories: quarks and leptons. Quarks (up, down, charm, strange, top, and bottom) carry fractional electric charge, weak isospin, and color charge, and interact via the electromagnetic, weak, and strong interactions. Quarks bind to each other via the strong interaction in a color-neutral form.

The color-neutral group is called a baryon if the group consists of three quarks. It is called a meson if the group consists of a quark-antiquark pair. Leptons (electron, muon, tau, and their corresponding neutrinos) are colorless and do not interact strongly, but only via the electromagnetic and weak interactions. The electron, muon, and tau are charged leptons, whereas neutrinos carry no electric charge and, therefore, only interact via the weak interaction, which makes them very difficult to detect.

All the fermions have a corresponding anti-particle with the same mass and opposite electric charge. Other quantum numbers are reversed for anti-particles also, such as the color charge. The quarks and the leptons are arranged in three generations in order of increasing particle masses within the SM. The first-generation particles constitute most of the matter in the known universe. The second and third generations are the replica of the first generation with unstable heavier particles decaying into lighter ones. Table 2.1 summarizes the three generations of fundamental fermions in the SM.

Table 2.1: Three generations of leptons and quarks in the Standard Model [1].

Generation	Symbol	Electric Charge [e]	Color	Mass [MeV/c^2]
1st generation	u	+2/3	r,b,g	1.5 - 3.3
	d	-1/3	r,b,g	3.5 - 6.0
	e	-1	——	0.511
	ν_e	0	——	$< 2\times10^{-6}$
2nd generation	c	+2/3	r,b,g	$1.27\ ^{+0.07}_{-0.11}\times10^3$
	s	-1/3	r,b,g	$104\ ^{+26}_{-34}$
	μ	-1	——	105.6
	ν_μ	0	——	< 0.170
3rd generation	t	+2/3	r,b,g	$(171.2 \pm 2.1)\times10^3$
	b	-1/3	r,b,g	$(4.2\ ^{+0.17}_{-0.07})\times10^3$
	τ	-1	——	1776.8
	ν_τ	0	——	< 18.2

Some properties of the bosons are given in Table 2.2. The boson of the strong force is the massless, neutral gluon. The gluons carry color charges and since there are eight independent color states, there exists eight types of gluons. The gluons can interact with themselves due to their own color charge (red (r), blue (b), green (g)). The photon is the boson of the electromagnetic interaction, and is massless and neutral. It only interacts with electrically charged particles, and since it does not carry electric charge, it does not interact with itself. Unlike the gluon and photon, the bosons of the weak interaction, W and Z, are massive. The W bosons carry an electric charge as well.

Table 2.2: Properties of bosons [1].

Boson Name	Force	Symbol	Electric Charge [e]	Mass [GeV/c^2]
Gluon	Strong	g	0	0
Photon	Electromagnetic	γ	0	0
W boson	Weak	$W^{\pm}$	± 1	80.398 $\pm$ 0.025
Z boson	Weak	Z^0	0	91.1876 $\pm$ 0.0021

2.2 Quantum Chromodynamics

Quantum chromodynamics (QCD) [24, 25, 26, 27] is the field theory describing the strong interactions of colored quarks and gluons. Color charge comes in three versions (red, green and blue) that form a fundamental representation of the $SU(3)$ group, and is carried by both the quarks and gluons. Analogous to electric charge in quantum electrodynamics (QED) [28, 29], color charge is conserved in QCD, but since the gluons carry color charge, they can interact with other gluons. This is not possible in QED, as photons do not carry electric charge. The existence of self-coupling in QCD has important implications for the scale dependence of the strong coupling.

In quantum field theory, the coupling constant describing the interaction between two particles is an effective constant, which is dependent on the energy-scale Q^2 of the interaction. In QED this dependence is only a weak one; in QCD, however, it is very strong. The reason is the self-coupling of the gluons. The dependence of the strong coupling constant $\alpha_s(Q^2)$ on Q^2 is known as a running coupling constant. In perturbative QCD (pQCD), a first-order approximation yields:

$$\alpha_s(Q^2) = \frac{1}{\beta_0\ ln(\frac{Q^2}{\Lambda^2_{QCD}})}, \text{ where } \beta_0 = \frac{33 - n_f}{12\pi}. \tag{2.1}$$

Here, n_f denotes the number of quark types with mass below Q^2, and Λ_{QCD} represents the characteristic scale of confinement. Λ_{QCD} is determined by comparing predictions with experimental data and is found to be on the order of 250 MeV [30].

The Q^2-dependence of the coupling strength corresponds to a dependence on quark separation. For very small distances and corresponding high values of Q^2, the strong coupling decreases, vanishing asymptotically as $Q^2 \to \infty$. In the limit $Q^2 \to \infty$, quarks can be considered to be "free"; this phenomenon is called asymptotic freedom. In contrast, at large distances, the strong coupling increases substantially so that it is not possible to detach individual quarks from hadrons. This phenomenon is called confinement. In this regime, perturbation theory breaks down.

Quarks and gluons are not seen in experiments. Instead, they turn into hadrons, which are observed in the detectors. This process is called hadronization. Hadronization of quarks happens at a later time ($t \sim \frac{1}{\Lambda_{QCD}}$) than the production process ($t \sim \frac{1}{Q}$). This is why the calculations of hadronic cross sections can be factorized into perturbative and non-perturbative parts.

2.2.1 Bottomonium Family

The production of a heavy-quark pair occurs at short distances and can be calculated in a perturbative manner due to the large scale of the quark masses, while the non-perturbative QCD effects that bind the heavy quark-antiquark pair into quarkonium can only be factorized into a universal wave function. The technique of separating the production process into two parts is known as factorization and is an essential component of QCD calculations of high-energy collisions.

Heavy quarkonia have been produced in a variety of collisions with different types of colliders: e^+e^-, ep, and pp. The highest energies are achieved in pp collisions, where heavy-quark pairs are produced by $q\bar{q}$ and gg interactions between the components of the proton. At high collision energies, due to asymptotic freedom the incoming hadrons behave like independent quarks and gluons. The momentum distributions of the quarks and gluons within hadrons are described by a set of parton distribution functions (PDF), which give the probability density for finding a parton with a certain longitudinal momentum fraction at a given momentum transfer. Both the longitudinal momentum fraction and the momentum transfer depend on the energy scale of the production process. Therefore, the inclusive heavy-quark production cross section depends on the PDFs and the amplitudes for $q\bar{q}$ and gg collisions to produce heavy quarks.

The mass spectra of the $b\bar{b}$ system and the transitions between them are shown in Figure 2.1. The $\Upsilon(4S)$ and the higher-mass resonances are above open-flavor threshold, $2m_B \simeq 10.56$ GeV for bottomonia, and decay rapidly to $B\bar{B}$ mesons. Table 2.3 summarizes the characteristics of the observed states below open-flavor threshold.

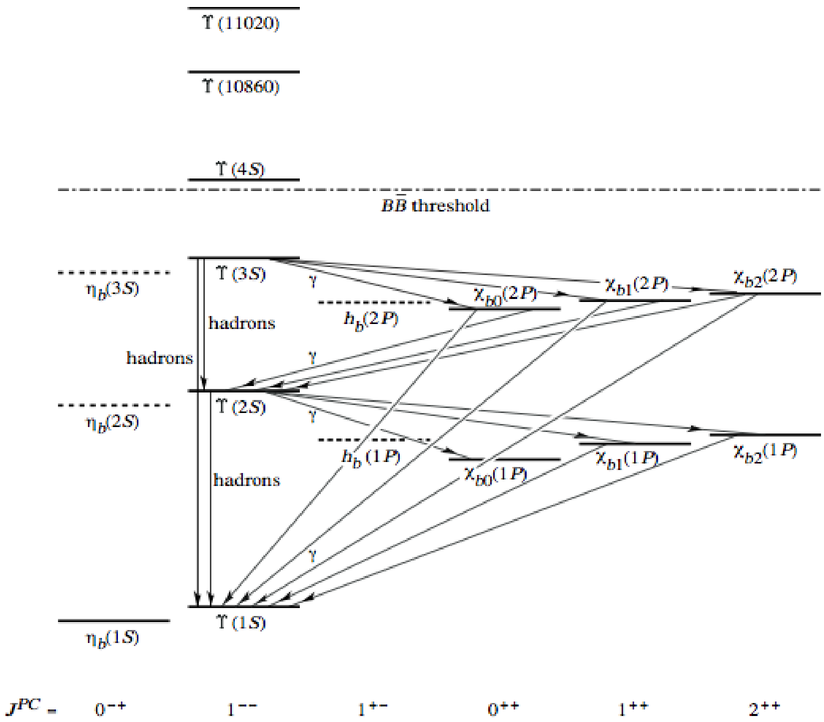

Figure 2.1: Spectrum and transitions of the bottomium family [1].

2.3 Bottomonium Production

Two processes dominate the production of bottomonium states in high-energy hadron collisions. The first is called direct production, in which a $b\bar{b}$ pair is produced in the particle collision, and the two quarks combine, producing a colorless $\Upsilon(nS)$ meson. The second is called indirect production, which involves the production of a heavier bottomonium state that then decays to a $\Upsilon(nS)$ meson. The production of a $\Upsilon(1S)$ meson in the decay of a χ_b or $\Upsilon(2S)$ is an example of the latter process. This phenomenon is also known as feed-down. Both types of bottomonium production occur at the interaction point and are known as prompt production. Bottomonium production does not have a non-prompt component that could come, for example, from the decay

Table 2.3: Properties of the bound-state bottomonia [1, 12].

Meson	$n^{2S+1}L_J$	J^{PC}	Mass [GeV/c^2]	$\Gamma_{\mu\mu}$[keV/c^2]
$\eta_b(1S)$	1^3S_0	0^{-+}	9.392	N/A
$\Upsilon(1S)$	1^3S_1	1^{--}	9.460	1.26
$h_b(1P)$	1^3P_1	1^{+-}	9.898	N/A
χ_{b0}, χ_{b1}, $\chi_{b2}(1P)$	$1^3P_{0,1,2}$	0^{++}, 1^{++}, 2^{++}	9.859, 9.893, 9.912	N/A
$\eta_b(2S)$	2^3S_0	0^{-+}	N/A	N/A
$\Upsilon(2S)$	2^3S_1	1^{--}	10.023	0.32
$h_b(2P)$	2^3P_1	1^{+-}	10.259	N/A
χ_{b0}, χ_{b1}, $\chi_{b2}(2P)$	$2^3P_{0,1,2}$	0^{++}, 1^{++}, 2^{++}	10.232, 10.255, 10.269	N/A
$\eta_b(3S)$	3^3S_0	0^{-+}	N/A	N/A
$\Upsilon(3S)$	3^3S_1	1^{--}	10.355	0.48

of a meson containing a top quark. Because of the very short lifetime of the top quark, the formation of a meson with a top quark in it does not occur. Table 2.4 summarizes the different production processes.

Table 2.4: Different processes involved in $\Upsilon(nS)$ (n= 1, 2, 3) production.

1^{st} Step	2^{nd} Step	3^{rd} Step	Type
	$b\bar{b}\rightarrow\Upsilon(nS)$	——	Prompt, Direct
$p\bar{p}\rightarrow b\bar{b}$+X	$b\bar{b}\rightarrow\chi_b$	$\chi_b\rightarrow\Upsilon(nS)+\gamma$	Prompt, Indirect
	$b\bar{b}\rightarrow\Upsilon(n'S)$	$\Upsilon(n'S)\rightarrow\Upsilon(nS)$+X	Prompt, Indirect

There are three types of models describing quarkonium production: the color-singlet model, the color-evaporation model, and the color-octet mechanism. In the color-singlet model, the color and the spin of the $b\bar{b}$ pair do not change during the binding. Since physical states are colorless, the pair is produced in a color-singlet state. In the color-evaporation model, the $b\bar{b}$ pair produced by the perturbative interaction is not assumed to be in a color-singlet state. The color and the spin of the $b\bar{b}$ pair are randomized by numerous soft interactions occurring after its production, and, as a consequence, the quarkonium meson is not constrained to have the same J^{PC} quantum numbers as the $b\bar{b}$ pair produced in the hard scatter. The color-octet mechanism extends the color-singlet approach by taking into account the production of $b\bar{b}$ pairs in a color-octet configuration. The color-octet state is then transformed into a color-singlet state with the emission of soft gluons.

Factorization is the key part in all the above-mentioned models. They treat the production of the $b\bar{b}$ pair separately from its evolution into a bound state. Next, the three main models for bottomonium production will be presented in their historical order.

2.3.1 Color-Evaporation Model

This model was first developed in 1977 [31, 32] and was revived in 1996 [33, 34]. In this method, the sum of the cross sections of all $b\bar{b}$ bound states σ_{onium} is given by the integral of the cross section for $b\bar{b}$ production, $\sigma_{b\bar{b}}$, from the threshold of $2m_b$ up to the threshold for the production of two beauty mesons, $2m_B$:

$$\sigma_{onium} = \frac{1}{9}\int_{2m_b}^{2m_B} \frac{d\sigma_{b\bar{b}}}{dm} dm \ , \tag{2.2}$$

where $\sigma_{b\bar{b}}$ is calculated with perturbation theory. The factor $\frac{1}{9}$ represents the probability that the $b\bar{b}$ pair will eventually be in a color-singlet state. Calculating the cross section for the production of a definite state, e.g., $\Upsilon(1S)$, is equivalent to "distributing" the cross sections among all states:

$$\sigma_{\Upsilon(1S)} = \rho_{\Upsilon(1S)} \ \sigma_{onium}. \tag{2.3}$$

The value for $\rho_{\Upsilon(1S)}$ depends on the number of quarkonium states lying between $2m_b$ and $2m_B$, factors arising from spin-multiplicity arguments, and the mass differences between the produced and final states [35].

The final transition to the color-singlet state proceeds via multiple soft-gluon interactions, which degrade the information on the polarization of the heavy-quark pair. That is the reason why this model, by construction, is unable to give information about the polarization of the produced quarkonium state, which is an important test for the other models [36].

2.3.2 Color-Singlet Model

The color-singlet model (CSM) [37, 38], initiated in the early 1980's, was the first to present quantitative predictions for bottomonium production in hadron-hadron and electron-proton collisions. The model decomposes the quarkonium production into two steps; first, the creation of two heavy quarks (b and $\bar{b}$), and then their binding to make the meson. Since the production process has a distance scale of $\frac{1}{Q}$, the first step is calculable by an expansion in powers of α_s. The second step, the long-distance part, is expressed as a universal wave function, which can be determined from data on decay processes. In this model, one assumes that the color and the spin of the $b\bar{b}$ pair do not change during the binding.

The long-distance part is related to the leptonic decay width Γ_{ll} of the bottomonium state, which at leading order (LO) can be expressed as [39]:

$$\Gamma_{ll} = \Gamma(\Upsilon \to l^+l^-) = \frac{4\alpha_s^2}{9m_\Upsilon^2}|R_\Upsilon(0)|^2 \ , \tag{2.4}$$

where $R_\Upsilon(0)$ is the Υ wave function at the origin.

In high-energy hadronic collisions, at lower values of $p_T(\leq 10$ GeV/c) the leading contribution comes from a gluon-fusion process; as the energy of the collider increases, so does the number of gluons. Figure 2.2 shows the dominant gluon-fusion processes; the one on the left, shows the primary contribution to $\Upsilon(nS)$ production at lower p_T, and the one on the right, is the other main contribution, where higher-mass $b\bar{b}$ states with various quantum numbers contribute to $\Upsilon(nS)$ production, via $\chi_b \to \Upsilon(nS) + \gamma$ decays, for example.

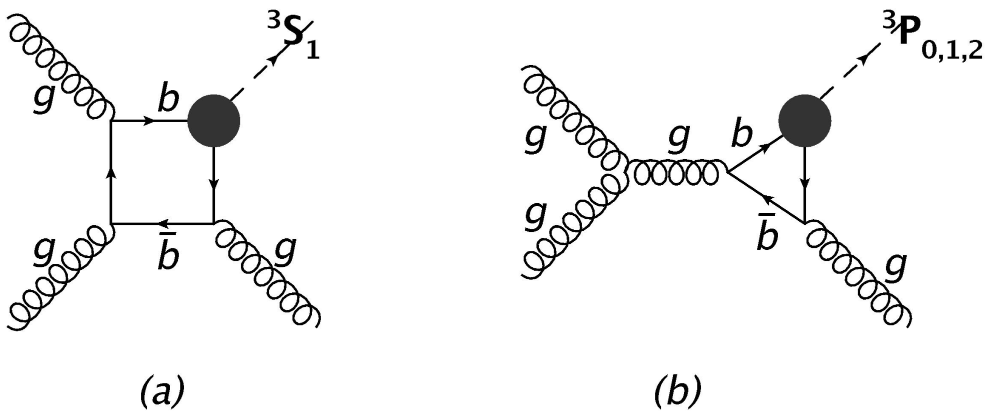

Figure 2.2: The diagrams for $gg \to {}^3S_1 g$ (a), and $gg \to {}^3P_{0,1,2} g$ (b) for LO in CSM.

The above leading-order diagrams occur at order α_s^3 and they scale as p_T^{-8}. At higher $p_T(\geq 15$ GeV/c), two other processes make a significant contribution to the bottomonium production. One is the next-to-leading order (NLO) [40] t-channel gluon-exchange process shown in Figure 2.3(a), which occurs at order α_s^4 and scales as p_T^{-6}, and the other is the gluon fragmentation process [41] displayed in Figure 2.3(b), which occurs at order α_s^5 and scales as p_T^{-4}.

For sufficiently large $p_T (\geq 15$ GeV/c), the more-constant p_T behavior of both processes can easily compensate for their α_s suppression compared to the LO (α_s^3) contributions. They are therefore expected to dominate over the LO diagrams at high p_T.

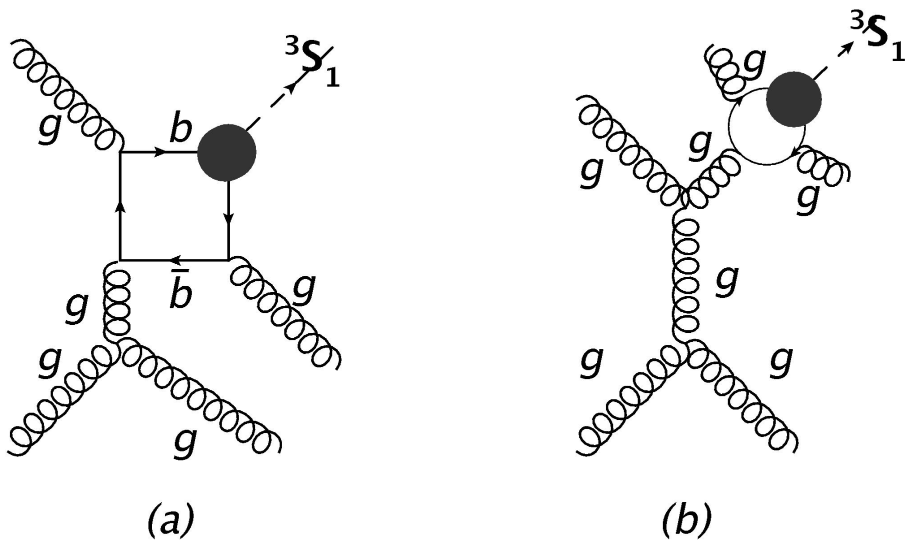

Figure 2.3: Example diagrams for t-channel gluon exchange (left) and gluon fragmentation (right) in the color-singlet mechanism.

2.3.3 NRQCD and Color-Octet Mechanism

This approach, also known as the non-relativistic QCD (NRQCD) factorization formalism, was first introduced in the early 1990's [22]. NRQCD [42] is an effective field theory that treats quarkonium as a non-relativistic system. In this model, bottomonium production is described as a two-step process: $b\bar{b}$ pair production at the perturbative level, followed by the evolution to a colorless quarkonium state through soft-gluon emission in the non-perturbative region. This effective theory is based on a systematic expansion in both α_s and v, which is the relative velocity of the quarks within the bound state.

For bottomonium $v_b^2 \simeq 0.08\ c^2$ [35]. In the color-octet formulation [43, 44], the wave function of physical quarkonium states can be decomposed into Fock states [45]. The wave function for an S-wave quarkonium state can be expressed as:

$$\begin{aligned} |\Psi_Q\rangle = \mathcal{O}(1)|Q\bar{Q}[^3S_1^{(1)}]\rangle + \mathcal{O}(v)|Q\bar{Q}[^3P_j^{(8)}g]\rangle + \\ \mathcal{O}(v^2)|Q\bar{Q}[^1S_0^{(8)}g]\rangle + \mathcal{O}(v^2)|Q\bar{Q}[^3S_1^{(1,8)}gg]\rangle + \dots \quad . \end{aligned} \tag{2.5}$$

The usual notation, ${}^{2S+1}L_J$, is used, and the color state is indicated with ${}^{(1)}$ for the singlet state and ${}^{(8)}$ for the octet state. The $\mathcal{O}(v^n)$ factors indicate the order in the velocity expansion at which the corresponding Fock state participates in the quarkonia production. Similarly, the wave function for P-wave quarkonium with total angular momentum J can be expressed as:

$$|\Psi_{Q_J}\rangle = \mathcal{O}(1)|Q\bar{Q}[^3P_J^{(1)}]\rangle + \mathcal{O}(v)|Q\bar{Q}[^3S_1^{(8)}]\rangle + \dots \quad . \tag{2.6}$$

In this formalism, the cross section for the inclusive production of a quarkonium state Q and other hadrons X is expressed as:

$$\sigma(Q + X) = \sum \hat{\sigma}(Q\bar{Q}[^{2S+1}L_J^{(1,8)}] + X)\langle \mathcal{O}^Q[^{2S+1}L_J^{(1,8)}]\rangle \ , \tag{2.7}$$

where the sum is over S, L, J, and color. The first term in the summation contains the short-distance quantities, while the second term has the long-distance quantities (matrix elements) that depend on the non-perturbative dynamics of the initial hadrons.

If one retains the color-singlet contributions at leading order in v for each quarkonium state in Eq. 2.7, then one obtains the CSM. However, such a truncation leads to inconsistencies because of the uncanceled divergences in the production rates of P-wave and other higher-orbital-angular-momentum quarkonium states.

The long-distance matrix elements (LDME's) $\langle \mathcal{O}^Q[^{2S+1}L_J^{(1,8)}]\rangle$ describe the transition between the quark-antiquark pair and the final physical state. Three intermediate color-octet states are considered in the description of ${}^3S_1$ production. These are the ${}^1S_0^{(8)}$, ${}^3P_0^{(8)}$, and ${}^3S_1^{(8)}$. The corresponding LDME's that give the probability of transition between these states and the physical color-singlet ${}^3S_1$ state can be extracted from experimental measurements, as described below.

An important property of the matrix elements is that they are universal, and thus process independent. Therefore, a matrix element measured by one experiment can be used to make predictions for a different experiment, e.g., CDF data [46] was used to measure the three different LDMEs (${}^1S_0^{(8)}$, ${}^3P_0^{(8)}$, ${}^3S_1^{(8)}$) for $\Upsilon(1S)$ production by two different theoretical groups [44, 47] and with different PDFs [48, 49, 50]. These LDMEs can then be applied to make predictions for other experiments.

2.4 Bottomonium Decays

One would naively expect a strongly interacting object such as bottomonia to decay "strongly". However, astonishingly enough, electromagnetic decays can also occur at an observable rate. The three ways in which bottomonia decay are summarized below.

2.4.1 A change of excitation level via photon emission (radiative decay)

This is an electromagnetic decay which is part of the $\Upsilon(nS)$ production as was summarized in Table 2.4. An example is:

$$\chi_b \to \Upsilon(nS) + \gamma.$$

2.4.2 Quark-antiquark annihilation into a virtual photon or gluons

The electromagnetic decays, despite the smallness of α, compete with the strong coupling α_s, since in the strong case three gluons must be exchanged to conserve color and parity. A factor of α_s^3 thus lowers this decay probability. States such as η_b, which have $J = 0$, can decay into two gluons or two real photons. The decay of the $\Upsilon(1S)$ $(J = 1)$ is mediated by three gluons or a single virtual photon, Figure 2.4.

$$\Upsilon(1S) \to ggg \to \text{hadrons}$$
$$\Upsilon(1S) \to \gamma^* \to \text{hadrons}$$
$$\Upsilon(1S) \to \gamma^* \to \text{leptons}$$

There are also feed-down affects like $\Upsilon(2S) \to \Upsilon(1S) + X$ and $\Upsilon(3S) \to \Upsilon(1S) + X$ as summarized in Table 2.4.

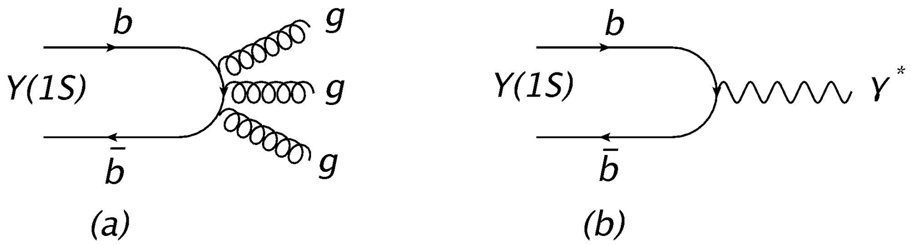

Figure 2.4: Diagrams for $\Upsilon(1S)$ strong decay into three gluons (left), electromagnetic decay through a virtual photon (right).

2.4.3 Creation of one or more light $q\bar{q}$ pairs from the vacuum to form B mesons

$$\Upsilon(4S) \rightarrow B + \bar{B}$$

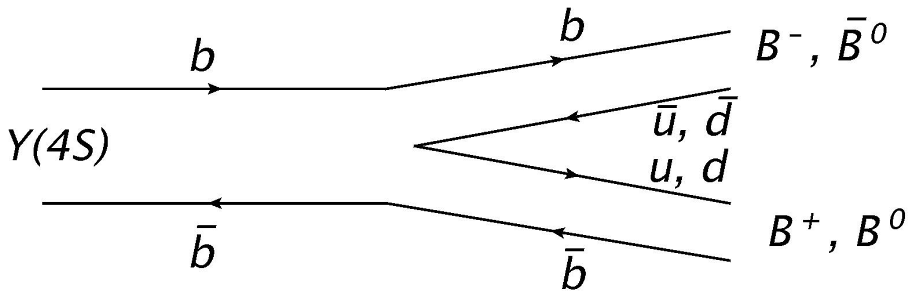

Figure 2.5: Diagram for the $\Upsilon(4S)$ strong decay into B mesons.

This strong decay shown in Figure 2.5 is, in principle, the most likely. But it can only take place above $B\bar{B}$ threshold since light $q\bar{q}$ pairs need to be created from the quarkonia binding energy. Hence, only options mentioned in Sections.2.4.1 and 2.4.2 are available below this threshold.

Electromagnetic processes like radiative decay are relatively slow. Furthermore, although hadronization via annihilation into gluons is a strong process such decays are suppressed, according to the OZI rule [51]. For these reasons the width of those bottomonia below $B\bar{B}$ threshold is very small (Γ = 54 KeV for the $\Upsilon(1S)$) as shown in Table 2.3.

2.5 Summary of the bottomonium measurements

The models discussed above for bottomonium formation lead to different expectations for the production rates and polarizations of the bottomonium states. The rest of the chapter focuses on the bottomonium measurements from the experiments at the Tevatron collider.

2.5.1 Quarkonium production at Tevatron

The most recent measurements on the Υ resonances cross sections and polarizations have been performed at the Tevatron at center-of-mass energies of $\sqrt{s} = 1.8$ TeV and 1.96 TeV by the CDF and D0 experiments. Although the cross-section measurements performed by the two experiments are in good agreement, the polarization measurements differ substantially.

The normalized differential cross sections for $\Upsilon(1S)$ production measured by the D0 experiment at $\sqrt{s} = 1.96$ TeV and the CDF experiment at $\sqrt{s} = 1.8$ TeV are shown in Figure 2.6, and are in agreement with each other.

The differential color-singlet cross section predictions [4] up to order α_s^5 are in agreement with the Tevatron measurements. The comparison of the color-singlet predictions for direct production of $\Upsilon(1S)$ at $\sqrt{s} = 1.8$ TeV with the CDF results are shown in Figure 2.7. In order to compare the color-singlet predictions for direct production of $\Upsilon(1S)$ with the CDF data, the most recent prompt-$\Upsilon(1S)$ cross-section measurement of [3] is multiplied by the direct fraction $F^{\Upsilon(1S)}_{direct} = 0.5 \pm 0.12$. This fraction was measured in an older data sample [52].

The LO and NLO results are very similar at low p_T, where the cross section is largest. This implies that the α_s^4 corrections are small in this region and that the perturbative expansion of the total cross section is under control. On the other hand, the relative importance of the NLO corrections dramatically increases at larger p_T, where new channels with a p_T^{-6} dependence (Figure 2.3(a)) start to dominate. This behavior signicantly reduces the discrepancy with the experimental data that is found at LO. However, the NLO prediction still drops too fast with p_T in comparison with the data. Note that the NLO calculation also takes into account associated production, $\Upsilon + \bar{b}b$. The associated production, in spite of reproducing the shape of the data very well at both low and high p_T (asymptotically it behaves as p_T^{-4}), remains negligible.

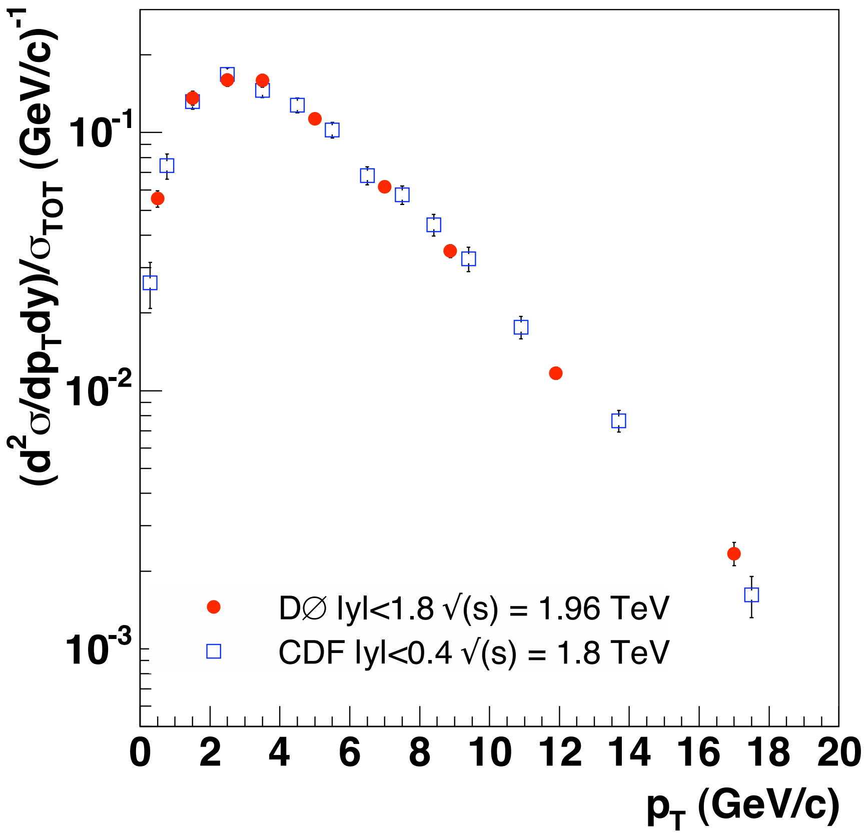

Figure 2.6: Normalized differential cross sections for $\Upsilon(1S)$ production at $\sqrt{s} = 1.96$ TeV by the D0 experiment [2] and at $\sqrt{s} = 1.8$ TeV by the CDF experiment [3] as a function of p_T.

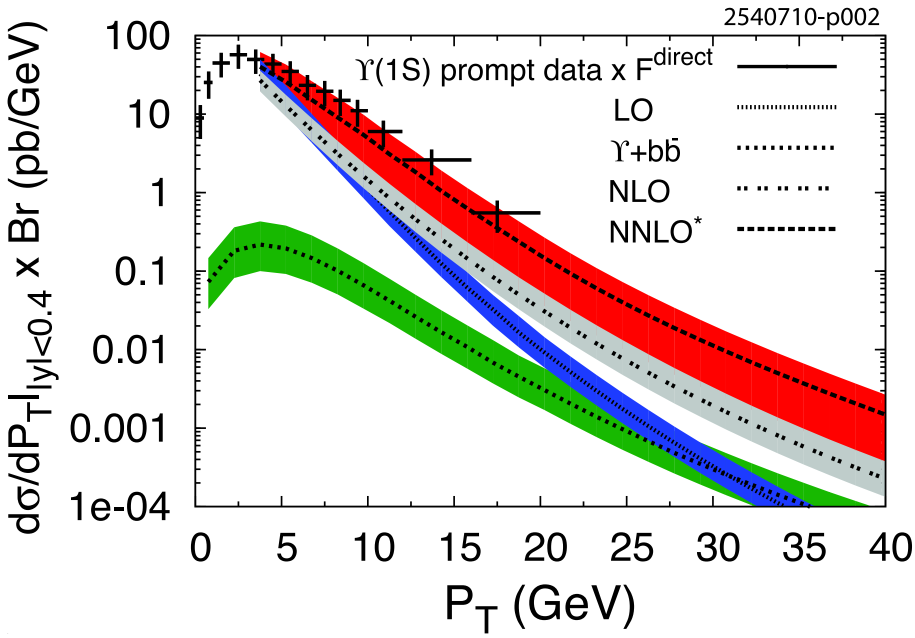

Figure 2.7: Theoretical predictions for the differential $\Upsilon(1S)$ + X cross section versus p_T at LO (α_s^3), for associated production (α_s^4), for full NLO (α_s^3+α_s^4), and for NNLO* (up to α_s^5), compared with the direct yield at $\sqrt{s}$ = 1.8 TeV measured by the CDF collaboration [4].

The discrepancy between the data and the full NLO (up to α_s^4) result increases with p_T. The α_s^5 terms provide the missing contributions. Indeed, the gluon fragmentation channel (Figure 2.3(b)) occurs for the first time at order α_s^5 and behaves like p_T^{-4} at large transverse momentum. The gluon fragmentation channel is a subset of $\bar{p}p \to \Upsilon$ + j j j (j stands for u, d, s, c, g), and provides new mechanisms to produce a high-p_T Υ with a lower kinematic suppression. This channel can therefore be expected to dominate the differential cross section at NNLO at transverse momentum. In Figure 2.7, the red band referred to as NNLO* corresponds to the sum of the NLO yield and the Υ + j j j contribution.

Both the NLO and NNLO* calculations predict a longitudinally polarized, directly produced $\Upsilon(1S)$, whereas the LO predicts a transversely polarized, directly produced $\Upsilon(1S)$. Similar to CSM-LO, COM (NRQCD) predicts a transversely polarized, promptly produced $\Upsilon(1S)$. The theoretical predictions for the polarization parameter α for direct Υ production in the color-singlet channel in $\bar{p}p$ collisions at $\sqrt{s}$ = 1.96 TeV for LO, NLO, and NNLO* are shown in Figure 2.8. The COM (NRQCD) predictions along with the experimental measurements are shown in Figure 2.9. Two different theoretical models predict different polarizations for Υ and moreover, CDF and D0 measure different polarization for prompt $\Upsilon(1S)$.

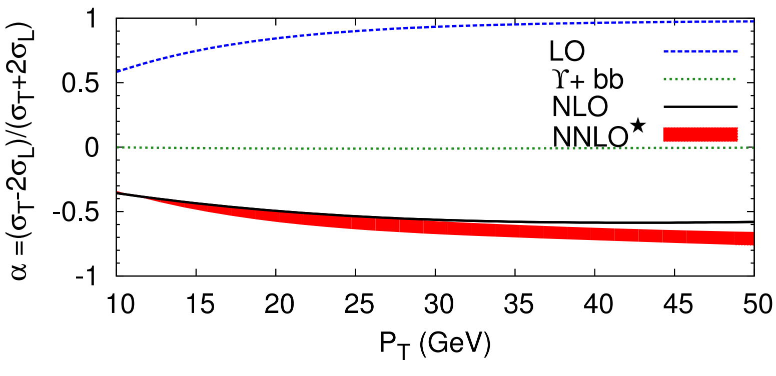

Figure 2.8: The theoretical predictions for the polarization parameter α for direct Υ production in the color-singlet channel in $\bar{p}p$ collisions at $\sqrt{s}$ = 1.96 TeV for LO, $\Upsilon + \bar{b}b$, NLO, and NNLO*, as a function of p_T.

The experimental data includes contributions from χ_b P-wave production and subsequent decays to $\Upsilon(1S)$. The effect of the feed-down on the Υ polarization predictions

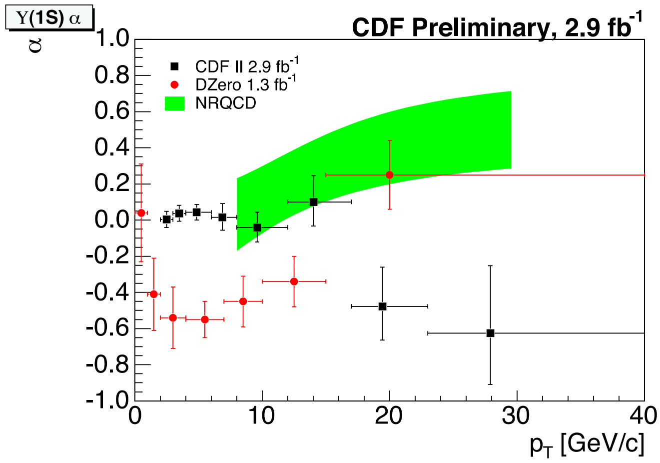

Figure 2.9: The COM (NRQCD) predictions with the experimental measurements for the polarization parameter α for prompt $\Upsilon(1S)$ production in $\bar{p}p$ at $\sqrt{s} = 1.96$ TeV.

causes a large systematical uncertainty, as shown in Figure 2.10, where the theoretical predictions, including the effect of the feed-down uncertainty, are compared to measurements from the D0 and CDF experiments. Two data sets clearly disagree, and the uncertainties on the theoretical predictions are huge, so it is difficult to draw any strong conclusion.

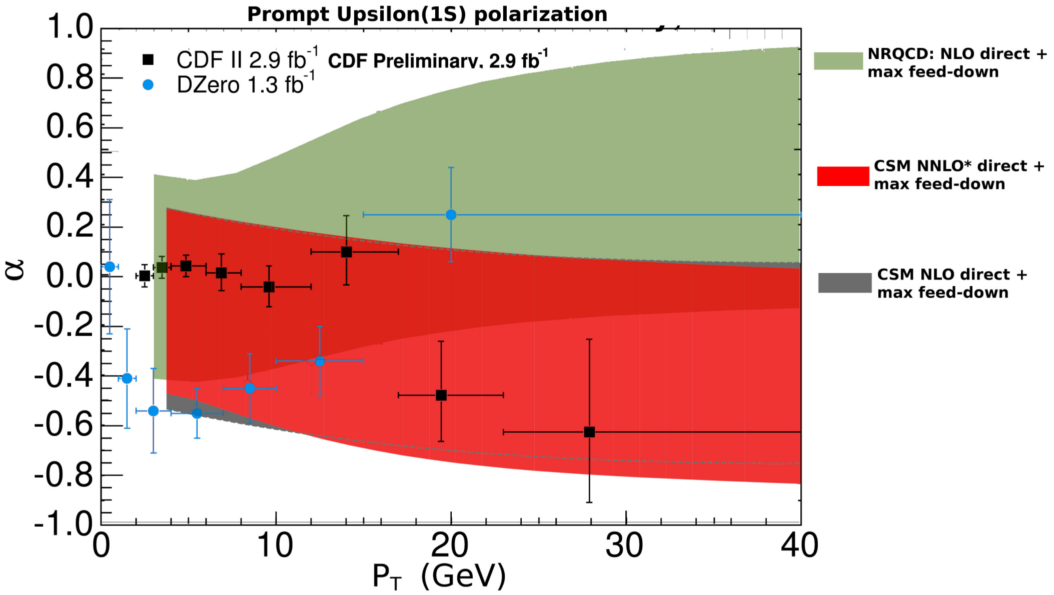

Figure 2.10: Prompt $\Upsilon(1S)$ polarization as a function of transverse momentum as predicted by NRQCD (including CO transitions), CSM at NLO, and CSM at NNLO*, compared to the D0 and CDF measurements [5]. The bands of the theoretical predictions are due to the feed-down uncertainty on the Υ polarization.

Chapter 3

The LHC and the CMS Experiment

The Large Hadron Collider (LHC) [53] is located near Geneva, Switzerland. The LHC is designed to collide proton beams at a center-of-mass energy of up to $\sqrt{s} = 14$ TeV with a nominal instantaneous luminosity of up to $\mathscr{L} = 10^{34}$ cm^{-2}s^{-1}. This proton-proton operation is a seven-fold increase in center-of-mass energy and almost two orders of magnitude increase in nominal instantaneous luminosity over the most powerful previous hadron-collider machine. Theoretical predictions suggest that a rich field of new physics can be studied at the LHC, the main motivations lie in searching for the Higgs boson, revealing the nature of electroweak symmetry breaking, and investigating possible new phenomena beyond the Standard Model. In addition to pp collisions, the LHC is capable of colliding heavy nuclei (Pb-Pb) with a center-of-mass energy of $\sqrt{s}$ = 2.76 TeV per nucleon and a peak luminosity of $\mathscr{L} = 10^{27}$ cm^{-2}s^{-1}.

There are four detectors installed in the experimental caverns around the collision points of the LHC: ATLAS [54] and CMS [7] are general purpose experiments, the LHCb [55] experiment is designed to focus on B physics, and the ALICE [56] experiment investigates heavy-ion collisions.

The rest of this chapter consists of an overview of the basic characteristics of the LHC and a description of CMS and its main sub-detectors.

3.1 The Large Hadron Collider

CERN's accelerator complex, shown in Figure 3.1, consists of successive machines with increasingly higher energies. The beam is injected from one machine to the next, which takes over to bring the beam to an even higher energy, and so on. The last element of this chain is the LHC, which accelerates each particle beam up to the record energy of 7 TeV.

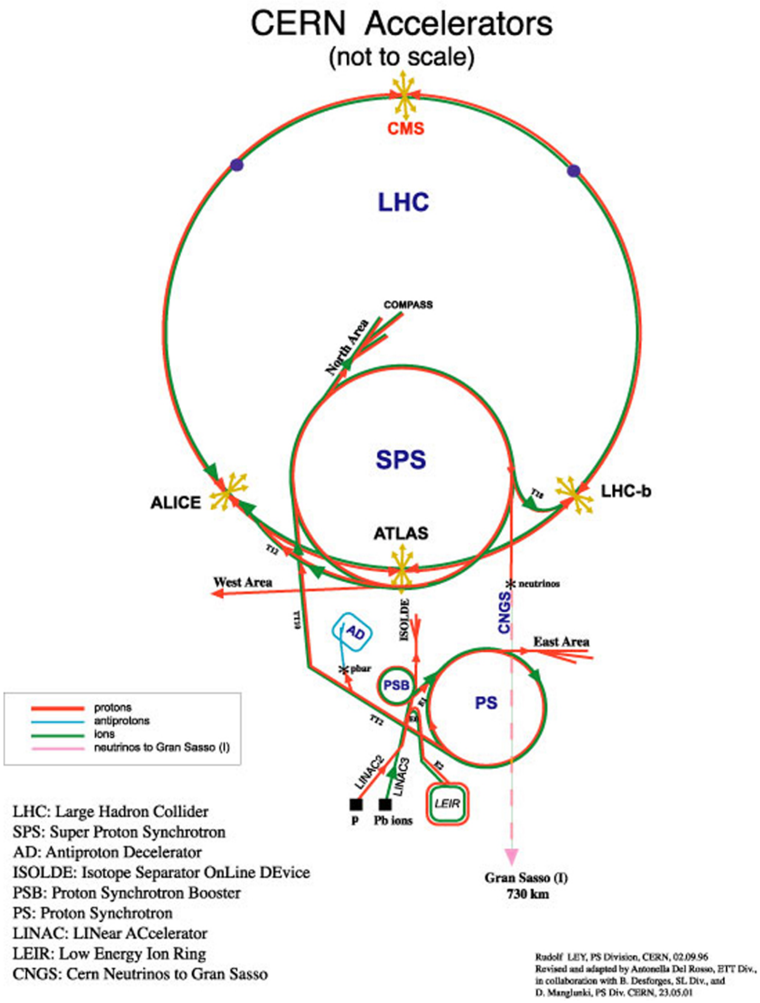

Figure 3.1: A schematic view of the CERN accelerator complex.

Protons are obtained by stripping electrons from hydrogen atoms. After acceleration in Linac2, protons are injected into the proton synchrotron booster (PSB) at an energy of 50 MeV. They are further accelerated to 1.4 GeV by the booster. The proton beam is then fed to the proton synchrotron (PS), where it is accelerated to 25 GeV. Next, protons are sent to the super proton synchrotron (SPS), which accelerates them to 450 GeV. Finally, they are transferred to the LHC, where they are accelerated to their nominal energy of 7 TeV.

In the LHC, under nominal operating conditions, each proton beam has 2808 bunches, with each bunch containing about 10^{11} protons. It is superconducting magnets with a magnetic field of 8.3 T that keep the protons in their orbit; these magnets are cooled with liquid helium to a temperature of 1.9 K.

At the interaction points, where the CMS, ATLAS, LHCb, and ALICE experiments are located, collisions happen every 25 ns, which corresponds to a bunch-crossing frequency of 40 MHz.

A list of parameters for the LHC is provided in Table 3.1 and more detailed information can be found in [57, 58].

Table 3.1: List of some LHC parameters.

Circumference	26659 m
Dipole operating temperature	1.9 K (-271.3°C)
Number of magnets	9593
Number of main dipoles	1232
Number of main quadrupoles	392
Number of RF cavities	8 per beam
Nominal energy, protons	7 TeV
Nominal energy, ions (per nucleon)	2.76 Tev/u
Peak magnetic dipole field	8.33 T
Min. distance per bunches	$\sim$7 m
Design luminosity	$10^{34}\,\mathrm{cm}^{-2}\mathrm{s}^{-1}$
No. of bunches per proton beam	2808
No. of protons per bunch (at start)	1.1×10^{11}
Collision rate	40 MHz
RMS beam size	16.7 μm

In 2010, first LHC collisions at 3.5 TeV/per proton beam took place on March 30th and pp collisions continued till late October. In November, LHC switched to heavy ion collisions. The data samples used in this thesis were obtained with pp collisions at $\sqrt{s}$ = 7 TeV and correspond to an integrated luminosity of 36.7 pb^{-1}. During pp collisions at $\sqrt{s}$ = 7 TeV the instantaneous luminosity increased from 2 $\times 10^{31}$ cm^{-2}s^{-1} to 2 $\times$ 10^{32} cm^{-2}s^{-1} and the number of bunches per beam increased from 56 to 368.

3.2 The CMS Detector

The CMS detector is located at the interaction point 5 (P5) of the LHC ring, near the village of Cessy in France. It is a general purpose detector located 100 m underground. Its design is motivated by the goals of the LHC physics program.

The CMS detector consists of a silicon tracking system, an electromagnetic and a hadronic calorimeter, a super-conducting solenoid magnet with a magnetic field of 3.8 T and a muon system. The detector is cylindrical in shape, consists of a barrel part and two endcaps, with an overall length of 21.6 m, and diameter of 14.6 m, with a total weight of 12,500 tons. The layout of the detector is given in Figure 9.5.

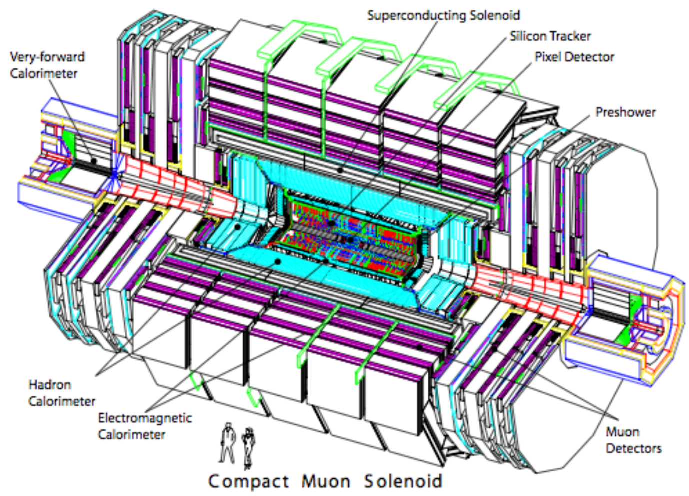

Figure 3.2: A schematic view of the CMS detector.

Since QCD jet production is the dominant process at the LHC, and many of the physics benchmark channels have a small cross section, a high background rejection power with an optimal efficiency for rare channels has to be achieved. In order to extract rare processes, high muon and electron identification efficiencies with excellent momentum and electromagnetic energy resolutions are desired. Moreover, the online event selection process, which is called the level-one "trigger", has to reduce hundred of millions of interactions per second to no more than 100 events/s for storage and further analysis. The short time(25ns) between bunch crossings and the high event rate at the LHC have major implications for the design of the readout and trigger systems.

At the design luminosity, around 20 inelastic collisions will take place per beam crossing. In the same bunch crossing, products of an interaction can be confused with those from other interactions. This is called "pile-up". The effects of pile-up can be minimized by using high-granularity detectors with good time resolution, resulting in low occupancy. Good time resolution is also needed to discriminate the interaction under study from the interactions occurring in neighboring bunch crossings. High radiation levels due to the large flux of particles near the interaction region is another difficulty and, because of it, radiation-tolerent detectors and front-end electronics are required.

The orientation of the CMS coordinate system is as follows: the nominal interaction point is the origin. The x-axis points radially inward towards the center of the LHC ring, the y-axis points vertically upward, and the z-axis points along the counter-clockwise beam direction. The azimuthal angle ϕ is measured from the x-axis in the x-y plane. The polar angle θ is measured from the z-axis and the pseudorapidity is $\eta = -\ln\,[\tan(\theta/2)]$. The momentum component of any particle transverse to the beam direction is denoted by p_T and transverse energy is defined as; $E_T = E\sin(\theta)$, where E is the calorimeter cell energy and θ is the angle between the beam direction and the direction of the vector pointing from the interaction vertex to the calorimeter cell.

A more detailed description of the CMS detector can be found in [6]. Figure 3.3 presents a transverse view of a section of the barrel detectors.

3.2.1 Magnet

The CMS detector has the largest solenoidal superconducting magnet in the world. With a maximum magnetic field of 3.8 T, the magnet provides a large bending power for high-energy charged particles in order to make a precise momentum measurement with the tracking detectors. The magnetic coil is 12.9 m long, has an inner bore of 5.9 m, and encloses the tracker and the barrel electromagnetic and hadronic calorimeters. The

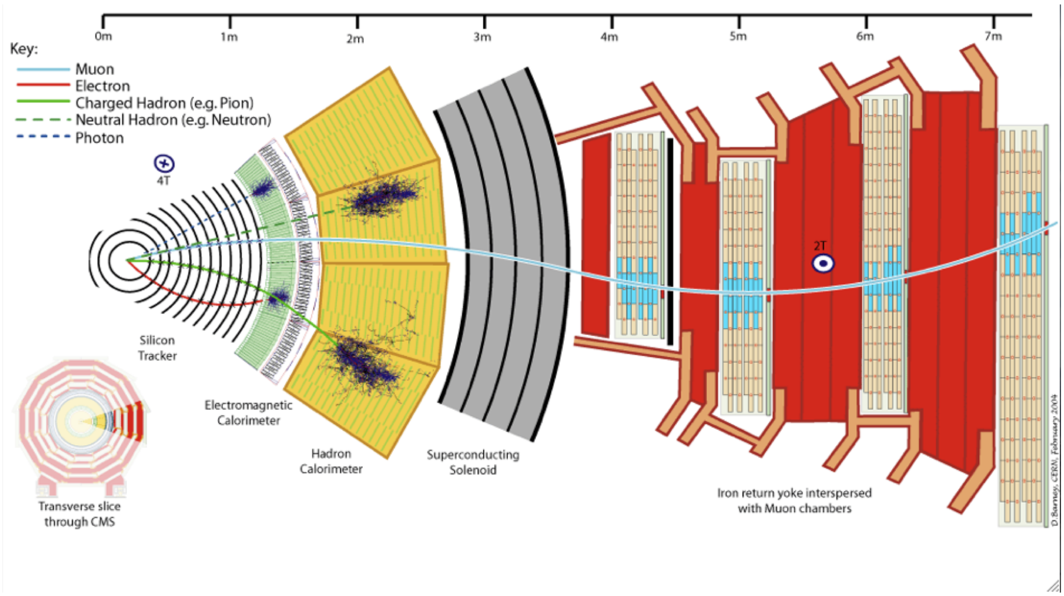

Figure 3.3: A transverse slice through the barrel portion of CMS showing different types of particles interacting with the different sub-detectors.

CMS solenoid [59] stores an energy of 2.6 GJ at full current. The steel magnet return yoke weights 10,000 tons and holds the muon chambers.

The main characteristics of the CMS magnet are the use of a high-purity aluminum-stabilized conductor with full epoxy impregnation and indirect cooling by thermosyphon. The total conductor cross section is 64×22 mm^2. The conductor was produced in twenty continuous pieces, each with a length of 2.65 km. Four continuous pieces are wounded together to make each of the 5 coil modules.

3.2.2 Tracking System

The all-silicon tracking detector of CMS has a total active area of 200 m^2, and is divided into pixel and strip parts. The tracker detector [60] is located close to the interaction region, and must operate in a very high particle flux. At LHC design luminosity, around 1000 charged particles are expected to pass through the tracking volume per 25 ns collision. This leads to a hit-rate density of 1 MHz/mm^2 at a radius of 4 cm. The tracking system is designed to determine the primary vertex, measure precisely the momentum of charged particles above 0.5 GeV/c, and identify secondary vertices for heavy-flavor signatures. In order to reduce the radiation effects and prolong the lifetime of the detector modules, the tracking detectors are designed to run at subzero temperatures. The tracker is cooled down to $-20°$C by a mono-phase liquid cooling system with C_6F_{14} as the cooling fluid.

The pixel detector contains 66 million pixels, and consists of 3 barrel layers and 2 endcap disks on each side of them. The barrel layers are located at mean radii of 4.4 cm, 7.3 cm and 10.2 cm, and have a length of 53 cm. The endcap disks, extending from 6 to 15 cm in radius, are placed on each side at z = $\pm$34.5 cm and $\pm$46.5 cm.

Each pixel is of size $100{\times}150\ \mu\mathrm{m}^2$, giving an occupancy of about 10^{-4} per pixel per LHC crossing. The barrel part is composed of 768 pixel modules arranged into half-ladders of 4 identical modules each. The endcap disks are assembled in a turn-like geometry with blades rotated by 20°; there are 672 pixel modules with 7 different modules in each blade on the endcap disks.

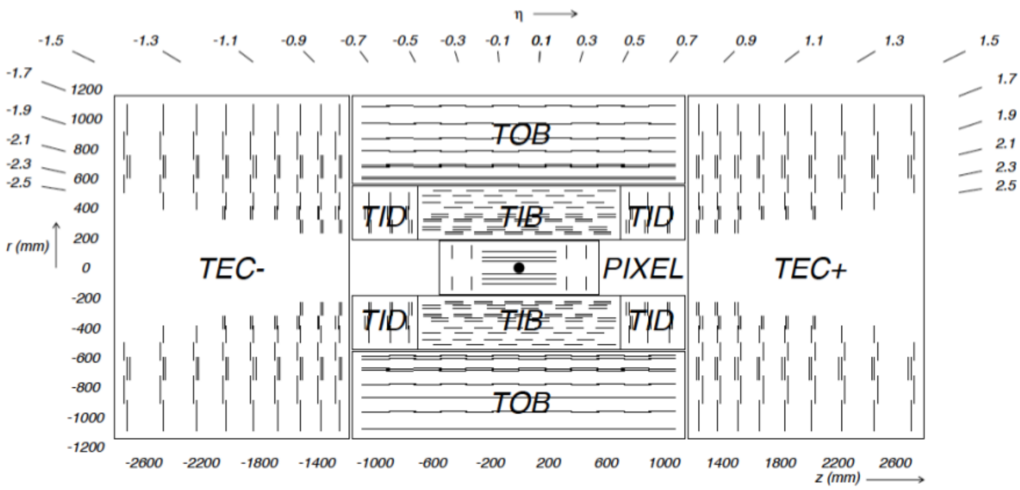

Figure 3.4: CMS tracker - single lines represent layers of modules with one sensor and double lines represent layers with back-to-back modules [6].

The strip detector is composed of four subsystems: the four-layer tracker inner barrel (TIB), the six-layer tracker outer barrel (TOB) and, on each side, the three-disk tracker inner disks (TID) and nine-disk tracker endcaps (TEC). A side view of the CMS tracker geometry is presented in Figure 3.4. The silicon tracker is 5.8 m in length and 2.4 m in diameter; it has 9.6 million silicon strips and covers $|\eta| < 2.4$.

Since the particle flux decreases with the radial distance from the interaction point, strip detectors with a minimum cell size of 10 cm $\times$ 80 μm can be used in the intermediate region, 20 cm $<$ r $<$ 50 cm, of the inner tracker. This cell size leads to an occupancy of $\sim$2-3% per LHC crossing. In the outermost region, r $>$ 55 cm, of the inner tracker, the particle flux has dropped enough to use larger-pitch silicon strips with a maximum cell size of 25 cm $\times$ 180 μm, which leads to an occupancy of $\sim$1% per LHC crossing.

There are 15400 single-sided modules in the silicon strip tracker. Modules for the TIB, TID and the first four rings of the TEC are single-sided, whereas the TOB and the outer three rings of the TEC are formed with double-sided modules. A double-sided module is constructed by putting two single-sided modules back-to-back with a stereo angle of 100 mrad between them. This orientation provides measurements in both r-ϕ and r-z coordinates.

3.2.2.1 Track Reconstruction

Charged particles travel through the tracker on a helical trajectory due to the axial magnetic field. In CMS, track reconstruction has three main stages: track seeding, track recognition, and track fitting. Since the pixel detector has low occupancy and is highly efficient with good spatial resolution, its hits are the best seeds for track candidates.

A Kalman-filter method is the basis for track recognition. It is an iterative process that starts from the seed layer with seed parameters and includes the information of successive layers one by one. With each new measurement the track parameters are known with a better precision, up to the last detection layer, where the full tracker information is included.

The trajectory building stage results in a collection of hits and an estimate of the track parameters for each trajectory. But the full information is not available until the last hit of the trajectory is found, and the constraints applied during the seeding stage can bias the estimate. In order to overcome this potential bias, the trajectory is refitted using a least-squares approach, implemented as a combination of the standard Kalman-filter and a second filter, called a smoother, running from the exterior of the tracking system to the beam line.

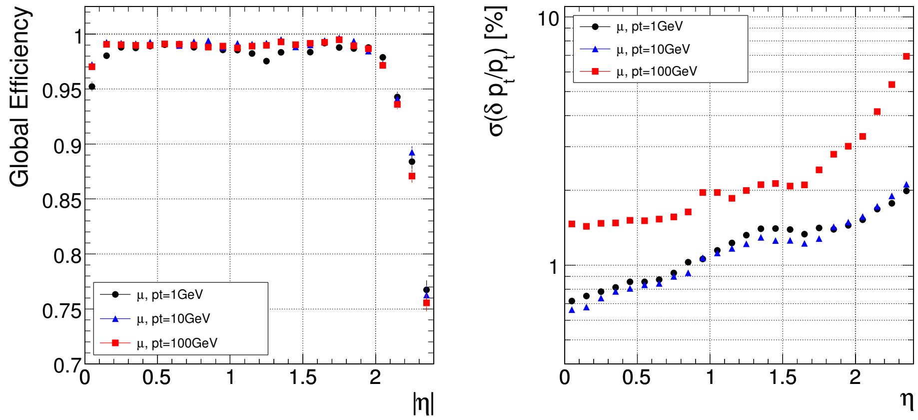

Figure 3.5: (left) Track reconstruction efficiency and (right) transverse momentum resolution for muons with $p_T = 1$, 10 and 100 GeV/c as a function of $|\eta|$ and η, respectively [6].

The expected performance of the reconstruction efficiency and the transverse momentum resolution for muon tracks, based on Monte Carlo simulation, are shown in Figure 3.5. The track reconstruction efficiency is higher than 95%, except for $|\eta| > 2.1$ where it falls to about 75% at $|\eta| = 2.4$, due to the reduced coverage of the forward pixel detector. For low momenta (1-10 GeV/c) the relative momentum resolution is around 1-2% for the entire η range; for high momenta (100 GeV/c) the resolution is again around 1-2% for $|\eta| < 1.6$ and for higher values of $|\eta|$ the lever arm of the measurement starts to become reduced and the resolution worsens to 7% at $|\eta| = 2.4$. At high momenta, multiple scattering from the material in the tracker accounts for 20-30% of the transverse momentum resolution, the rest is due to imperfect knowledge of the magnetic field and misalignment. At lower momenta, the resolution is dominated by multiple scattering and its distribution reflects the amount of material traversed by the track. The material budget of the CMS tracker in units of radiation length is given in Figure 3.6.

The details of track reconstruction in CMS can be found in [61].

3.2.3 Electromagnetic Calorimeter

The electromagnetic calorimeter (ECAL) [62] is a homogenous detector that is designed to make precise energy measurements of electromagnetically interacting electrons and

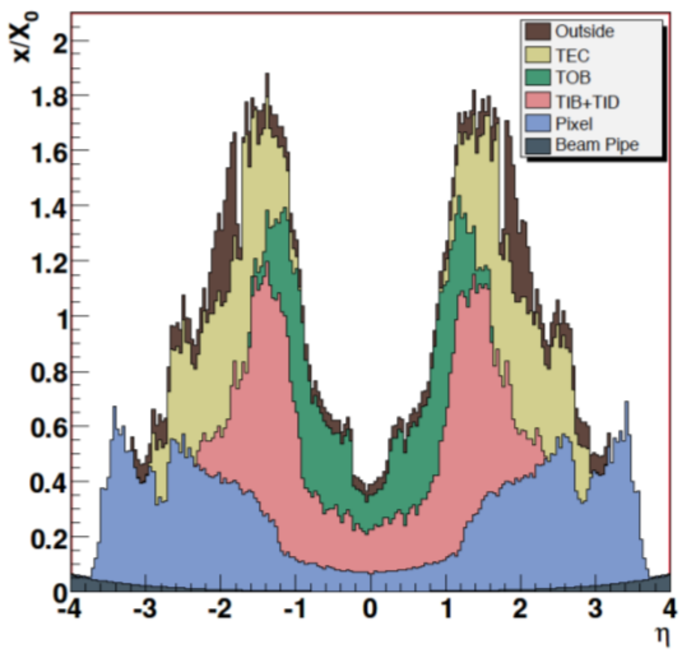

Figure 3.6: Material budget of the CMS tracker in units of radiation length X_0 as a function of η [6].

photons, and covers the pseudorapidity range up to $|\eta| = 3$. Lead tungstate ($PbWO_4$) scintillating crystals are chosen for the ECAL because of their short radiation length (X_0 = 0.89 cm) and Moliere radius [63] (2.2 cm), fast response time (80% of the light is emitted within 25 ns) and radiation hardness (up to 10 Mrad). The low light yield (30 γ/MeV) of these crystals requires the use of sensitive photodetectors. Silicon avalanche photodiodes (APDs) and vacuum phototriodes (VPTs) are used in the barrel and endcaps, respectively. There are 61200 lead tungstate crystals mounted in the barrel and 7324 in each endcap. The crystals are mounted in a quasi-projective geometry, with a front face of 22×22 mm^2 and 28.6×28.6 mm^2 in the barrel and the endcaps, respectively. The length of a barrel crystal is 23 cm, which corresponds to 25.8 X_0, and the length of an endcap crystal is 22 cm, corresponding to 24.7 X_0.

The crystals have to withstand the radiation levels and particle fluxes anticipated throughout the duration of the experiment. Ionizing radiation produces absorption bands through the formation of color centers due to oxygen vacancies and impurities in the lattice. The practical consequence is a wavelength-dependent loss of light transmission without changes to the scintillation mechanism, a damage that can be tracked and corrected for by monitoring the optical transparency with injected laser light. The damage reaches a dose-rate dependent equilibrium level that results from a balance between damage and recovery at 18°C. Therefore, the ECAL operates at 18°C by using a water cooling system.

The barrel part of the ECAL (EB) is at a distance of 1.6 m from the beam line and made up of 36 identical supermodules and covers the range $|\eta| < 1.479$. The ECAL endcaps (EE) are at a distance of 3.15 m from the interaction point and cover from 1.653 $< |\eta| < 3.0$. In order to obtain better spatial resolution, a finer-granularity preshower detector (ES) is placed in front of the EE, covering the range $1.653 < |\eta| < 2.6$. The ES is a sampling calorimeter with 2 layers of lead radiators to initiate electromagnetic showers from incoming photons and electrons, while silicon strip sensors placed after each radiator measure the energy deposited and the transverse shower profiles. The longitudinal view of a quarter of the CMS ECAL is shown in Figure 3.7.

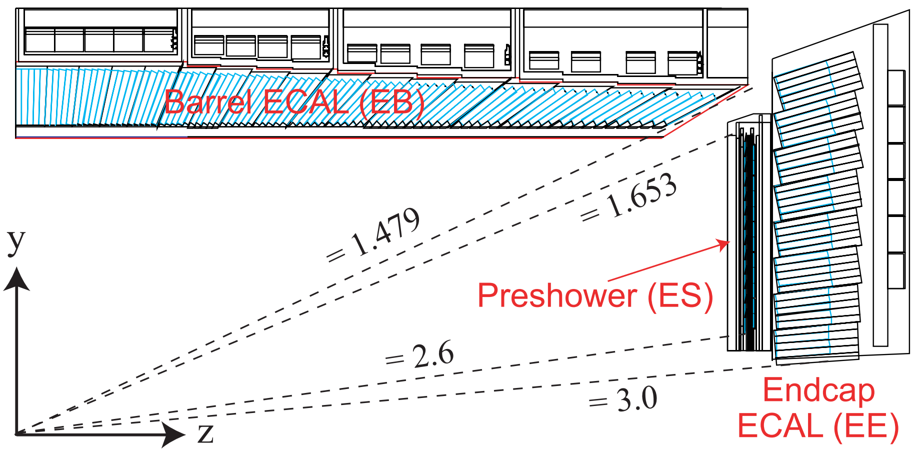

Figure 3.7: Transverse section through the ECAL [6].

The performance of a supermodule was measured in a test beam. The energy resolution σ, measured by fitting a Gaussian function to the reconstructed energy distributions, of a ECAL supermodule can be expressed as a function of energy by:

$$(\frac{\sigma}{E})^2 = (\frac{S}{\sqrt{E}})^2 + (\frac{N}{E})^2 + C^2 \ , \tag{3.1}$$

where S is the stochastic term, N is the noise, and C is a constant term. The values of the parameters were measured with data from an electron test beam, and are listed in the Figure 3.8. The energy resolution is 1% for an energy of 25 GeV, and decreases to 0.4% when the energy is 250 GeV.

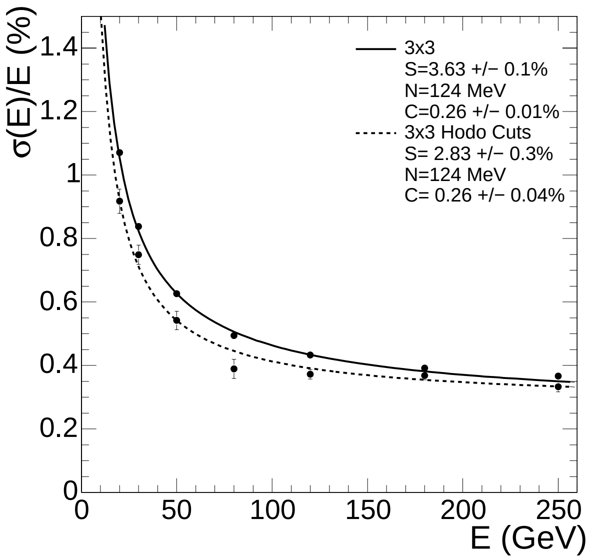

Figure 3.8: ECAL supermodule energy resolution as measured from a test beam. The upper series of points correspond to events selected to fall within a 20×20 mm^2 region, and the lower series of points correspond to events selected to fall within a 4×4 mm^2 region. The energy was measured in an array of 3×3 crystals with electrons impacting the central crystal. The measured values, by fitting the points to the function in Eq. 3.1, of the stochastic term S, the noise N, and the constant term C are given in the legend for the two different lines [6].

3.2.4 Hadronic Calorimeter

The hadronic calorimeter (HCAL) surrounds the ECAL system, with the barrel part located inside the magnet coil. The HCAL [64] is a sampling calorimeter built from alternating layers of absorbing brass plates and plastic scintillator tiles arranged in trays. The barrel part of the HCAL is restricted in volume between the outer extent of the ECAL (r = 1.77 m) and the inner extent of the magnetic coil (r = 2.95 m). This is complemented by an additional layer of scintillators, referred to as the hadron outer (HO) detector, positioned outside of the magnetic coil.

The barrel part of HCAL (HB) covers the range $|\eta| < 1.4$ in 2304 towers with segmentation of $\Delta\eta \times \Delta\phi = 0.087 \times 0.087$. The HB has 15 brass plates, each having a thickness of about 5 cm, and 2 external stainless steel plates for mechanical strength. The HB is supplemented by the HO containing scintillators with a thickness of 10 mm, which line the outside of the outer vacuum tank of the coil and cover the region $|\eta| < 1.26$. The HO uses the magnet as an additional layer of absorber and provides adequate containment for hadronic showers to over 10 interaction lengths. The HO scintillators match the HB tower geometry in η and ϕ.

The HCAL endcaps (HE) cover the range from $1.3 < |\eta| < 3.0$. Each HE consists of 14 η towers; for the 5 outermost towers (smaller $|\eta|$) the ϕ segmentation is 5° and the η segmentation is 0.087, whereas for the 8 innermost towers the ϕ segmentation is 10° and the η segmentation changes between 0.09 to 0.35. The total number of HE towers is 2304. The HCAL tower segmentation for one quarter of the HB, HO and HE detectors is displayed in Figure 3.9.

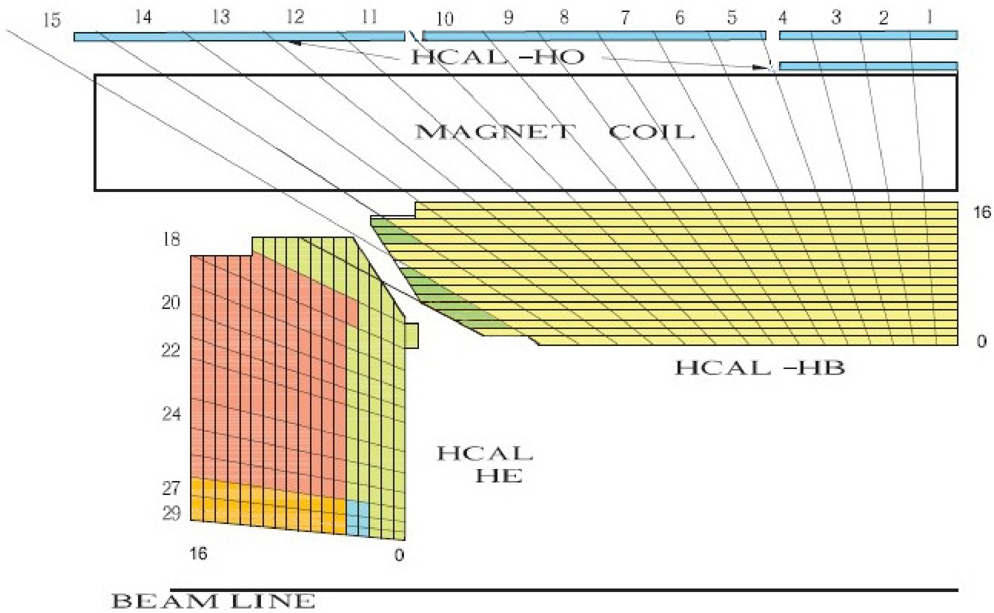

Figure 3.9: Tower segmentation for one quarter of the HCAL. The colors represent the optical grouping of scintillator layers into different readouts [6].

The plastic scintillator tiles are read out with embedded wavelength-shifting (WLS) fibers. The WLS fibers are spliced to high-attenuation-length clear fibers outside the scintillator, which carry the light to the read-out system. There are 70000 and 20916 scintillator tiles installed in the HB and the HE, respectively.

The hadron forward (HF) calorimeter is located at z = ±11.2 m from the interaction point and has a depth of 1.65 m. The HF covers the range from $3.0 < |\eta| < 5.0$; the signal originates from Cerenkov light emitted in quartz fibers, which is then channeled by the fibers to photomultipliers.

The granularity of the sampling in the 3 parts of the HCAL has been chosen such that the jet energy resolution, as a function of E_T, is similar in all 3 parts. This is shown in Figure 3.10. The reconstructed jet transverse energy (E_T^{rec}) was compared to the MC generated transverse energy (E_T^{MC}). The distribution of E_T^{rec}/E_T^{MC} was fit. The jet transverse resolution is defined as the sigma over mean of the fit and is shown with respect to E_T^{MC} in Figure 3.10. The resolution of the missing transverse energy (E_T^{miss}) in QCD dijet events with pile-up, an average of 3.5 fully inelastic events per 25 ns beam crossing, is given by $\sigma(E_T^{miss}) \approx 1.0\ \sqrt{\sum E_T}\ GeV^{\frac{1}{2}}$ if energy clustering corrections are not made, while the average E_T^{miss} is given by $\langle E_T^{miss}\rangle \approx 1.25\ \sqrt{\sum E_T}\ GeV^{\frac{1}{2}}$.

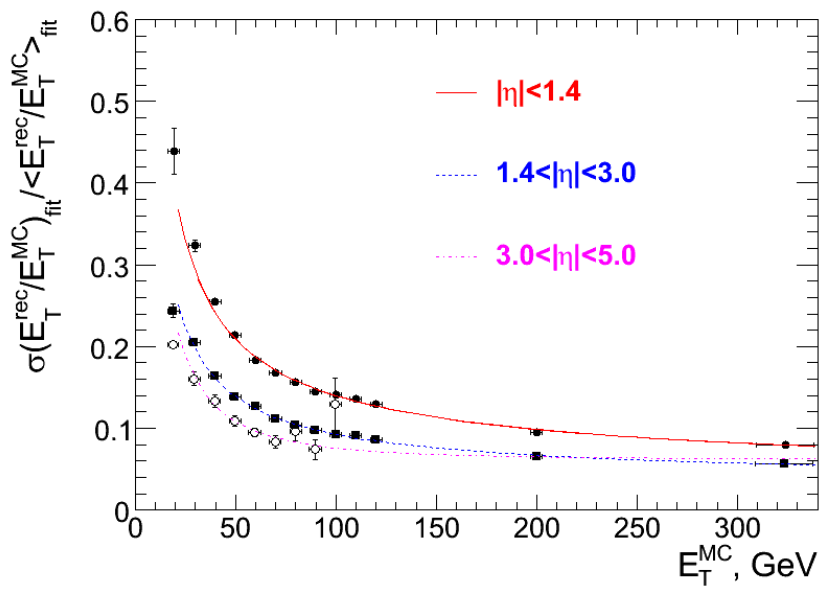

Figure 3.10: The jet transverse energy resolution as a function of the simulated jet transverse energy for barrel jets ($|\eta| < 1.4$), endcap jets ($1.4 < |\eta| < 3.0$) and very forward jets ($3.0 < |\eta| < 5.0$) [6].

3.2.5 Muon System

The muon system is the outermost part of the CMS detector. It relies on three types of gaseous detectors for muon identification and momentum measurement. These detectors are mounted between the steel plates of the magnet return yoke. In total, the muon system contains of order 25000 m^2 of active detection planes, and nearly 1 million electronic channels.

The drift tube (DT) chambers are used in the barrel region ($|\eta| < 1.2$), where the neutron-induced background is small, the muon rate is low and residual magnetic field is high. The cathode strip chambers (CSC) are deployed in the endcaps, where the muon rate, as well as the neutron-induced background rate, are high, as is the magnetic field. The CSCs cover the pseudorapidity range from $0.9 < |\eta| < 2.4$. The resistive plate chambers (RPC) are used in both the barrel and the endcaps. The RPCs cover the range up to $|\eta| < 1.6$. The layout of the CMS muon system is shown in Figure 3.11.

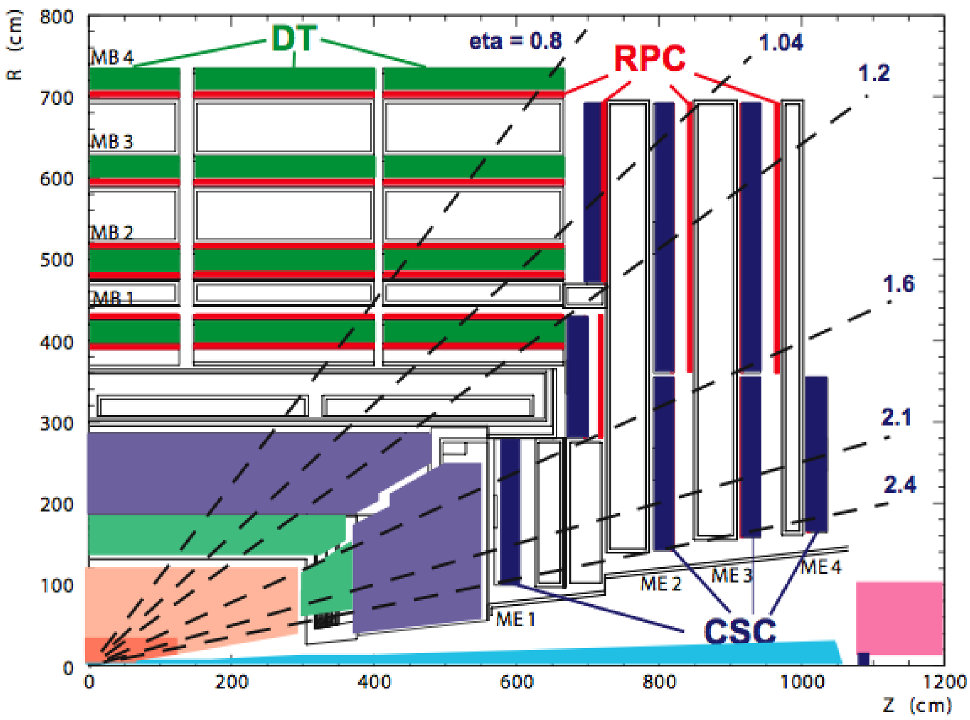

Figure 3.11: Layout of one quarter of the CMS muon system [6].

The muon barrel (MB) detector consists of 250 DTs in 4 stations inside the magnet yoke. The segmentation along the beam direction follows the 5 wheels of the yoke, each of which is divided into 12 sectors, with each covering a 30° azimuthal angle. In the first two stations (MB1 and MB2) each DT chamber is sandwiched between 2 RPCs. In the last two stations (MB3 and MB4) one RPC is placed on the innermost side of the station for each DT.

There are 473 CSCs in the muon endcap (ME) system. In each of the endcaps, the CSCs and RPCs are organized in 4 disks perpendicular to the beam. Each disk is arranged in concentric rings; 3 rings in the innermost station, 2 rings in the middle two stations and 1 ring for the outermost station. There are 5 additional CSCs in the last station for one endcap.

Each DT chamber consists of 12 layers of DT cells, which are 4.2 cm in size, organized in three groups of four. The tubes inside each layer are staggered by half a tube. Two outside groups measure the $r - \phi$ coordinate in the bending plane (they have wires parallel to the beam line), and the middle group measures the z-component running parallel to the beam by having wires perpendicular to the beam. The chambers are operated with an Ar/CO_2 (85/15%) gas mixture. The voltages applied to the electrodes are +3600 V for wires, +1800 V for strips, and 1200 V for cathodes. The electron drift velocity is about 54 μm/ns. A honeycomb structure separates an $r - \phi$ layer from the other two layers. This gives a lever arm length of about 28 cm for the measurement of the track direction inside each chamber in the bending plane. The maximum drift length is 2.0 cm and the single-point resolution is $\approx 200\ \mu m$. Each station is designed to give a muon vector in space, with a ϕ precision better than 100 μm in position and approximately 1 mrad in direction.

The CSCs are trapezoidal in shape and consist of 6 gas gaps, each gap having a plane of radial cathode strips and a plane of anode wires at high voltage (3.6 kV) running almost perpendicularly to the strips. The CSCs operate with a gas mixture of $Ar\text{-}CO_2\text{-}CF_4(40\%, 50\%, 10\%)$. The gas ionization and subsequent electron avalanche caused by a charged particle traversing each plane of a chamber produces a charge on the anode wire and an image charge on a group of cathode strips. Thereby, each CSC measures the space coordinates (r, ϕ, z) in each of the 6 layers. The strip width varies for the chambers from 4 to 16 mm. With strips this wide, the spatial resolution depends on the hit position across a strip; it is worst when the hit occurs at the center of a strip since there is almost no charge sharing, while on the contrary it is good between strips.

In order to compensate for this effect, odd and even chamber planes are staggered by half a strip width, which ensures that 3 out of 6 hits will be in the area of good spatial resolution. The overall six-plane chamber spatial resolution from the strips is typically about 50 μm. The angular resolution in ϕ is of order 10 mrad. The typical wire timing resolution is 12 ns for a single plane and 4 ns for a chamber.

The innermost CSC station is called ME1/1. The ME1/1 chambers differ from all other CSCs in that within a single station the electronics are mounted facing alternately toward and away from the IP. ME1/1 anode wires have a 29 degree inclination to compensate for the lorentz angle in the magnetic field. ME1/1 is divided into two substations in η, labeled ME1/1a inner part (by radius) and ME1/1b outer part. ME1/1b has 64 strips while ME1/1a has 48 strips. The 48 strips of ME1/1a are ganged 3:1 into 16 readout channels in a fashion that retains fine-grained position information. The ME1/1s operate at high voltage of 3kV.

Each RPC detector consists of a double-gap bakelite chamber, operating in avalanche mode. A cluster of electrons, produced by an ionizing particle, begins the avalanche multiplication. The electronic charge is then developed inside the gap. Each RPC gap is operated at a voltage of 10 kV, with a current limit of 200 μA. The drift of the charge towards the anode induces a signal on the pick-up electrode. The RPCs operate with a non-flammable gas mixture of $C_2H_2F_4$ and i-C_4H_{10}. The RPCs complement the muon system measurement by their high-rate capability and good time resolution (1 ns).

The details of the muon system can found in [65].

3.2.5.1 Muon Reconstruction

Muon reconstruction is performed in 3 stages: local pattern recognition, standalone reconstruction, and global reconstruction. The muon reconstruction algorithm is seeded by muon candidates found by the Level-1 muon trigger. The details of the muon trigger will discussed in Sec.3.2.6. Starting from a seed, the muon chambers compatible with the seed are identified and local pattern recognition is performed only in those chambers; track segments are built by associating aligned hits in the chambers. Standalone muon reconstruction uses only information from the muon system, while global and tracker muon reconstructions also use silicon tracker hits.

The standalone muon reconstruction starts with the track segments from the muon chambers obtained by the local pattern recognition. The muon trajectories are formed by working from the inner-most to outer-most segments, using a Kalman-filter technique. After the trajectory is formed, another Kalman-filter procedure is applied to determine the track parameters, but this time moving from the outer-most to inner-most segments. Lastly, the track is extrapolated to the nominal interaction point and a vertex-constrained fit to the track parameters is carried out.

The global muon reconstruction includes silicon tracker hits in the extended muon trajectories. The standalone muon track parameters are compared to the track parameters of tracks found in the silicon tracker by extrapolating the muon track trajectories from the innermost muon station to the outer tracker surface. If the state vector (track position, momentum and direction) of a track in the silicon tracker is compatible with the extrapolated muon track trajectory, the hits from the silicon tracker and the muon system are combined and refitted to build a global muon track.

In some cases, the standalone muon reconstruction fails due to the lack of hit and segment information in the muon system. For these cases, a complementary approach is considered. The tracker muon reconstruction considers all tracks in the silicon tracker and identifies tracker muons by looking for compatible segments in the muon system.

The standalone muon momentum resolution is dominated by multiple scattering in the material before the first muon station up to p_T values of about 200 GeV/c, when the chamber spatial resolution starts to dominate. For global and tracker muons at low momentum, the momentum resolution is given by the resolution obtained in the silicon tracker. The momentum resolution for global muons is better than standalone muons at all momentum, and is better than tracker muons at high momentum. A comparison of the momentum resolution of the tracker system, the muon system, and the combined measurement is given in Figure 3.12 for two η bins of width 0.2 in the barrel and endcap regions.

3.2.6 Trigger and Data Acquisition System

The CMS trigger system is designed to deal with the high luminosity and interaction rates at the LHC. The trigger system has to reduce the 40 MHz event rate to a final rate of about 100 Hz, while maintaining a high efficiency for a broad variety of physics processes.

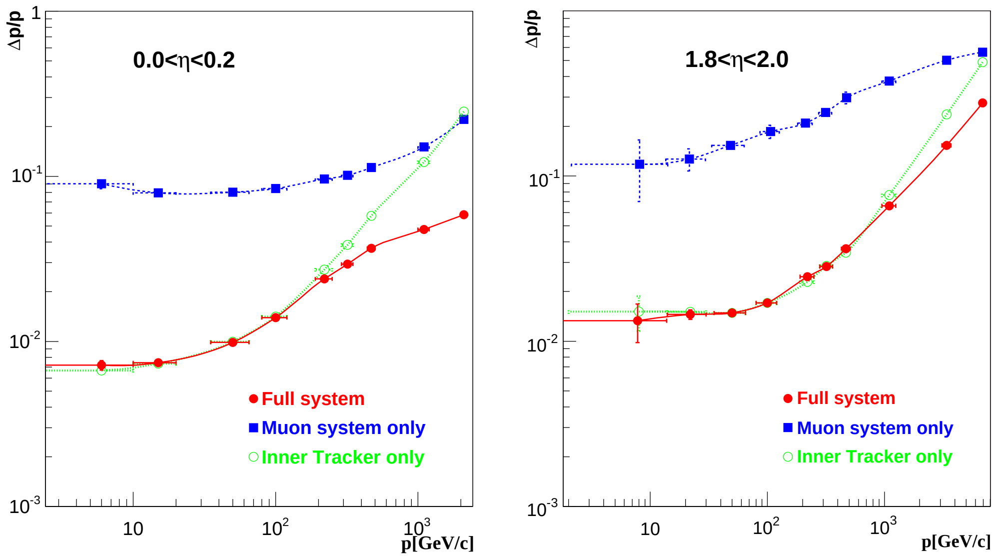

Figure 3.12: The muon momentum resolution versus p from the silicon tracker system (open circles), the muon system(squares), and both(closed circles), for (left) $\eta < 0.2$ and (right) $1.8 < \eta < 2.0$ [6].

The trigger system consists of two parts: level 1 (L1) [66] and a high-level trigger (HLT) [67]. The L1 trigger is designed to achieve a maximum output rate of 100 kHz within a time period of 3.2 μs. The L1 trigger consists of custom, programmable hardware processors, whereas the HLT is based on software algorithms running on a large cluster of computers. The HLT reduces the L1 output rate to the final 100 Hz at which events are stored.

The L1 trigger uses reduced-granularity and reduced-resolution data from the muon and calorimetry systems, while the full data are held in pipelined memories waiting for the L1 decision. As mentioned above, the decision must be taken within 3.2 μs. The latency of the decision not only depends on the decision of the local, regional and global trigger components, but also on the readiness of the other sub-detectors and data acquisition system (DAQ). The L1 trigger architecture is presented in Figure 3.13.

The muon trigger uses all three types of muon detectors. The CSCs provide track segments in three dimensions, and find the bunch crossing for the track. The DTs provide hit patterns in both ϕ and η. In the CSCs, muon segments are found separately by the cathode and anode electronics trigger boards; the cathode electronics design is

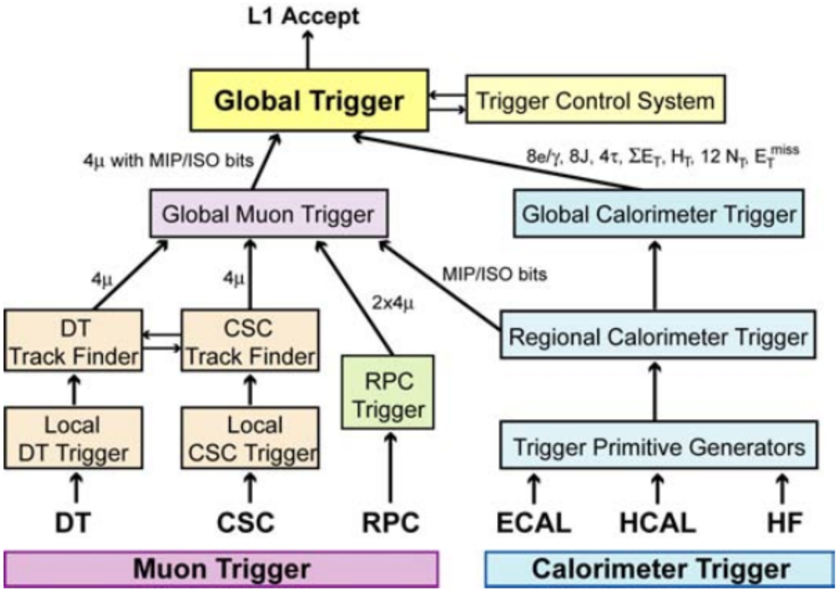

Figure 3.13: Architecture of the CMS L1 trigger [7].

optimized to measure the ϕ value and the direction, while the anode electronics design is optimized to determine the muon bunch crossing and the η value. The transverse momentum, location and quality of a track segment are calculated by the separate CSC and DT trackfinders. The RPCs carry out a measurement on the time-coincidence, and assigns a p_T value extracted from regional hit patterns. The global muon trigger receives up to four muon candidates each from the DTs, CSCs, barrel RPCs, and endcap RPCs per beam crossing, as well as isolation information from the global calorimeter trigger. The global muon trigger selects up to four muon trigger candidates and determines their momentum, position, charge, and quality.

The ECAL and the HCAL generate trigger primitives by calculating the transverse energy from a trigger tower and assigning it to a bunch crossing. The trigger towers are formed by calorimeter cells with a coverage of 0.087×0.087 in (η, ϕ) for the barrel region, a larger size of up to 0.350×0.350 for HE, and up to 0.828×0.828 for HF in the forward region. The trigger primitives are sent to a regional calorimeter trigger that determines the regional photon, electron, and jet candidates, together with the information needed for muon identification. The global calorimeter trigger provides the information about the jets, the total transverse energy, and missing energy in the event.

The global trigger (GT) combines the information about the trigger objects that are sent from the global muon and calorimeter triggers, makes a decision on whether to accept an event, and distributes this decision to the sub-detectors. The decision is based on simple algorithmic criteria such as the transverse momentum of a single trigger object being larger than a given threshold or the object multiplicities exceeding certain values.

The CMS DAQ processes the L1-accepted events at a rate of up to 100 kHz. The full detector information for an event ($\sim$1.5 MB) is read out by the DAQ and passed to the event filter farm as the HLT input. The HLT code is the same as the full offline analysis code, the major difference being the limited processing time for the former. In order to minimize the processing time, the HLT code only reconstructs trigger objects and regions of the detector that are actually needed for the trigger decision. In this way, lengthy computations are avoided, and events that should be rejected are discarded as soon as possible. A set of trigger paths are contained in the HLT menu, each path addresses a specific trigger object selection with a kinematic cut, e.g., HLT_Mu3, HLT_Jet15U, HLT_Ele10_LW_L1R. The execution of a path is aborted if the event does not fulfill the conditions imposed. In the end, the HLT accepts events at a rate up to 100 Hz for mass storage. The specific HLT paths are discussed in Chapter.5.

Chapter 4

Monte Carlo Event Generators

This chapter provides information on the generation of the Monte Carlo (MC) event samples used in this thesis.

4.1 Υ and J/ψ Generation in PYTHIA

Simulated Υ events are used to tune the selection criteria, calculate the efficiencies for analysis cuts and vertexing, calculate the corrections to the muon identification and trigger efficiencies, and estimate the fit parameters for the final-state radiative tail. The MC-estimated fit parameters are then used for the fits to the data. Simulated J/ψ events are used to check the tag-and-probe (TNP) method for muon identification and trigger efficiencies, as described in Chapter 6.

The simulated Υ and J/ψ events are produced using the PYTHIA generator [13], which is a program for the generation of high-energy physics events. It contains theory and models for a number of physics processes, including hard and soft interactions, parton distributions, initial- and final-state parton showers, multiple interactions, fragmentation and decay. The production of the Υ and J/ψ events is based on leading-order color-singlet and color-octet mechanisms. A summary of the subprocesses for all the color-singlet and color-octet production in PYTHIA is given in Table 4.1. These subprocesses are switched on by setting MSEL(62) = 1 for Υ and MSEL(61) = 1 for J/ψ in the program. Figure 9.3 shows the Feynman diagrams for color-octet t-channel gluon exchange and fragmentation processes; the corresponding processes for the color-singlet mechanism were discussed in Section 2.3.2. The color-octet states undergo a shower evolution via emission of a soft gluon and end up as a color-neutral state. The tuning of the NRQCD matrix elements is obtained by comparing results of NRQCD calculations with measurements from CDF [14]. The matrix elements are listed in Table 4.2. It is possible with PYTHIA to produce direct J/ψ and also indirect J/ψ from χ_c, and similarly direct Υ and also indirect Υ from χ_b as different processes, see Table 2.4. The polarization of the J/ψ and Υ in the event generation is set to zero.

Table 4.1: Color-singlet/octet production subprocesses and their corresponding ISUB indices in PYTHIA [13] for J/ψ and Υ production.

Color-singlet/octet production in PYTHIA			
Charmonium subprocesses		Bottomonium subprocesses	
421	$g + g \to c\bar{c}[^3S_1^{(1)}] + g$	461	$g + g \to b\bar{b}[^3S_1^{(1)}] + g$
422	$g + g \to c\bar{c}[^3S_1^{(8)}] + g$	462	$g + g \to b\bar{b}[^3S_1^{(8)}] + g$
423	$g + g \to c\bar{c}[^1S_0^{(8)}] + g$	463	$g + g \to b\bar{b}[^1S_0^{(8)}] + g$
424	$g + g \to c\bar{c}[^3P_J^{(8)}] + g$	464	$g + g \to b\bar{b}[^3P_J^{(8)}] + g$
425	$g + q \to q + c\bar{c}[^3S_1^{(8)}]$	465	$g + q \to q + b\bar{b}[^3S_1^{(8)}]$
426	$g + q \to q + c\bar{c}[^1S_0^{(8)}]$	466	$g + q \to q + b\bar{b}[^1S_0^{(8)}]$
427	$g + q \to q + c\bar{c}[^3P_J^{(8)}]$	467	$g + q \to q + b\bar{b}[^3P_J^{(8)}]$
428	$g + \bar{q} \to c\bar{c}[^3S_1^{(8)}] + g$	468	$g + \bar{q} \to b\bar{b}[^3S_1^{(8)}] + g$
429	$g + \bar{q} \to c\bar{c}[^1S_0^{(8)}] + g$	469	$g + \bar{q} \to b\bar{b}[^1S_0^{(8)}] + g$
430	$g + \bar{q} \to c\bar{c}[^3P_J^{(8)}] + g$	470	$g + \bar{q} \to b\bar{b}[^3P_J^{(8)}] + g$
431	$g + g \to c\bar{c}[^3P_0^{(1)}] + g$	471	$g + g \to b\bar{b}[^3P_0^{(1)}] + g$
432	$g + g \to c\bar{c}[^3P_1^{(1)}] + g$	472	$g + g \to b\bar{b}[^3P_1^{(1)}] + g$
433	$g + g \to c\bar{c}[^3P_2^{(1)}] + g$	473	$g + g \to b\bar{b}[^3P_2^{(1)}] + g$
434	$g + q \to q + c\bar{c}[^3P_0^{(1)}]$	474	$g + g \to q + b\bar{b}[^3P_0^{(1)}]$
435	$g + q \to q + c\bar{c}[^3P_1^{(1)}]$	475	$g + g \to q + b\bar{b}[^3P_1^{(1)}]$
436	$g + q \to q + c\bar{c}[^3P_2^{(1)}]$	476	$g + g \to q + b\bar{b}[^3P_2^{(1)}]$
437	$g + \bar{q} \to c\bar{c}[^3P_0^{(1)}] + g$	477	$g + \bar{q} \to b\bar{b}[^3P_0^{(1)}] + g$
438	$g + \bar{q} \to c\bar{c}[^3P_1^{(1)}] + g$	478	$g + \bar{q} \to b\bar{b}[^3P_1^{(1)}] + g$
439	$g + \bar{q} \to c\bar{c}[^3P_2^{(1)}] + g$	479	$g + \bar{q} \to b\bar{b}[^3P_2^{(1)}] + g$

The response of the CMS detector is simulated with a GEANT4-based [68] MC program. GEANT4 is a toolkit for simulating the passage of particles through matter. It

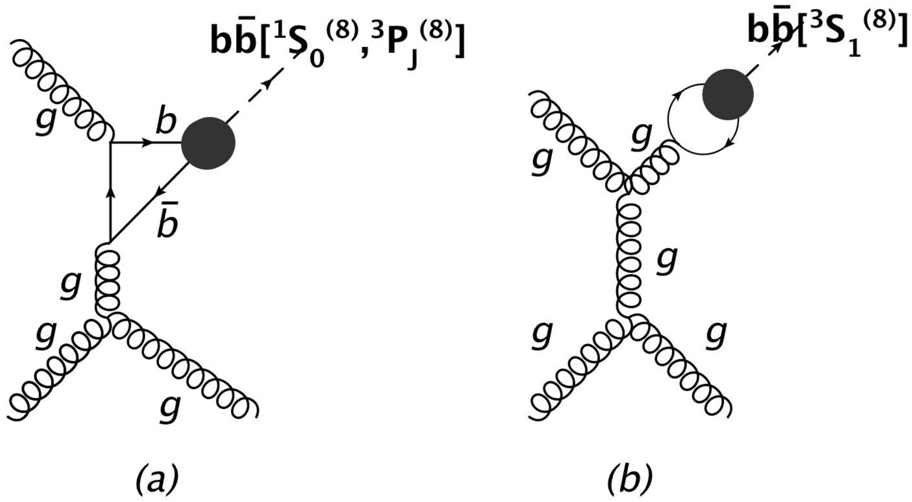

Figure 4.1: The diagrams for t-channel gluon exchange (left) and gluon fragmentation (right) in the color-octet mechanism.

Table 4.2: The J/ψ and Υ matrix elements and their corresponding parameters in PYTHIA [14, 15].

PYTHIA parameter	Value J/ψ			Matrix Element
PARP(141)	1.16			$\langle\, \mathcal{O}(\mathrm{J}/\psi)[^3S_1^{(1)}]\, \rangle$
PARP(142)	0.0119			$\langle\, \mathcal{O}(\mathrm{J}/\psi)[^3S_1^{(8)}]\, \rangle$
PARP(143)	0.01			$\langle\, \mathcal{O}(\mathrm{J}/\psi)[^1S_0^{(8)}]\, \rangle$
PARP(144)	0.01			$\langle\, \mathcal{O}(\mathrm{J}/\psi)[^3P_0^{(8)}]\, \rangle \,/\, m_c^2$
PARP(145)	0.05			$\langle\, \mathcal{O}(\chi_{c0})[^3P_0^{(1)}]\, \rangle \,/\, m_c^2$
	$\Upsilon(1S)$	$\Upsilon(2S)$	$\Upsilon(3S)$	
PARP(146)	9.28	4.63	3.54	$\langle\, \mathcal{O}(\Upsilon)[^3S_1^{(1)}]\, \rangle$
PARP(147)	0.15	0.045	0.075	$\langle\, \mathcal{O}(\Upsilon)[^3S_1^{(8)}]\, \rangle$
PARP(148)	0.02	0.006	0.01	$\langle\, \mathcal{O}(\Upsilon)[^1S_0^{(8)}]\, \rangle$
PARP(149)	0.02	0.006	0.01	$\langle\, \mathcal{O}(\Upsilon)[^3P_0^{(8)}]\, \rangle \,/\, m_b^2$
PARP(150)	0.085	0.108	0.0	$\langle\, \mathcal{O}(\chi_{b0})[^3P_0^{(1)}]\, \rangle \,/\, m_b^2$

includes modules for handling geometry, tracking, detector response, run management, visualization, and user interface.

The geometry module offers the ability to describe a geometrical structure and propagate particles efficiently through it. There are two different types of volumes in the geometry module: logical and physical. A logical volume represents a detector element of a certain shape that can hold other volumes inside it and can have other attributes; it also has access to other information that is independent of its physical position in the detector, such as material and sensitive-detector behaviour. A physical volume represents the spatial positioning or placement of the logical volume with respect to an enclosing mother (logical) volume. Thus, a hierarchical tree structure of volumes can be built, each volume containing smaller volumes.

In GEANT4, each particle is moved step by step with a tolerance that permits significant optimizing of execution performance, but that preserves the required tracking precision. The physics process associated with the particle sets the step size. For a particle at rest, this is a time rather than a length. The physical values associated with each step are exchanged between the tracking and each physics process. The step length (or lifetime for the at-rest action) is straightforwardly calculated from the mean lifetime of the particle. The generation of decay products requires a knowledge of branching ratios.

A particle in flight is subject to many competing processes. In simulation, as mentioned above, the particle proceeds in steps, and an efficient and unbiased way of choosing step value needs to be found. If the particle continues, the parameters for the next step also need to be updated. First, the distance to the point of interaction or decay is calculated. This is characterized by the mean-free path λ. The probability of surviving a distance l is

$$P(l) = e^{-n_\lambda}, \tag{4.1}$$

where $n_\lambda = \int_0^l dl/\lambda(l)$. For a decay, $\lambda = \gamma v \tau$; where v is the velocity, τ is the mean lifetime, and γ is the Lorentz factor. It must be kept in mind that λ varies as the particle loses energy and changes discontinuously at a geometrical boundary. Processes other than interaction or decay also compete to limit the step. Continuous energy loss can limit the step size too. The process which returns the smallest distance is selected and the step is finalized. If this is an interaction or decay, the particle is eliminated and secondaries are generated. If not, the particle gets another chance to interact or decay; for each process n_λ is decremented by an amount corresponding to the step length, and the entire algorithm is repeated at the next step.

An example showing how well the simulation reflects the data is displayed in Figure 4.2 using the position resolution of the primary event vertex. The primary vertex resolution depends strongly on the number of tracks used in fitting the vertex and the p_T of those tracks. A data-driven method to measure the resolution as a function of the number of tracks in the vertex, which is referred to as the "split method" is introduced. The tracks used in the vertex for an event are split evenly into two different sets. During the splitting procedure, the tracks are first ordered in descending order of p_T and then grouped in pairs starting from the track with largest p_T. For each pair, tracks are randomly assigned to one of the track sets. This procedure ensures that the two track sets have the same kinematic distributions on average. These two different track sets are independently given as input to the adaptive vertex fitter. The distributions of the difference in the fitted vertex positions for a given number of tracks are then fit with a single Gaussian distribution to extract the resolution. Figure 4.2 shows the measured primary vertex resolutions in x (a), y (b), and z (c) as a function of the number of tracks. Results are shown for both the data and the simulation, and good agreement between the two sets is seen. The resolutions in x and y are observed to be consistent, as expected given the shape of the beams and the symmetry of the tracker. For minimum-bias events at $\sqrt{s}$ = 7 TeV, the resolutions in x(y) and z are found to be about 25 μm and 20 μm, respectively, for primary vertices with more than 30 tracks [8].

Final-state radiation is implemented using the PHOTOS program [69, 70]. PHOTOS uses an algorithm that adds bremsstrahlung photons to already existing events, which are produced by a host generator that does not take into account the effects of QED radiative corrections. PHOTOS adds final-state QED radiation in the decay of particles and resonances, independent of the physics process from which they were generated.

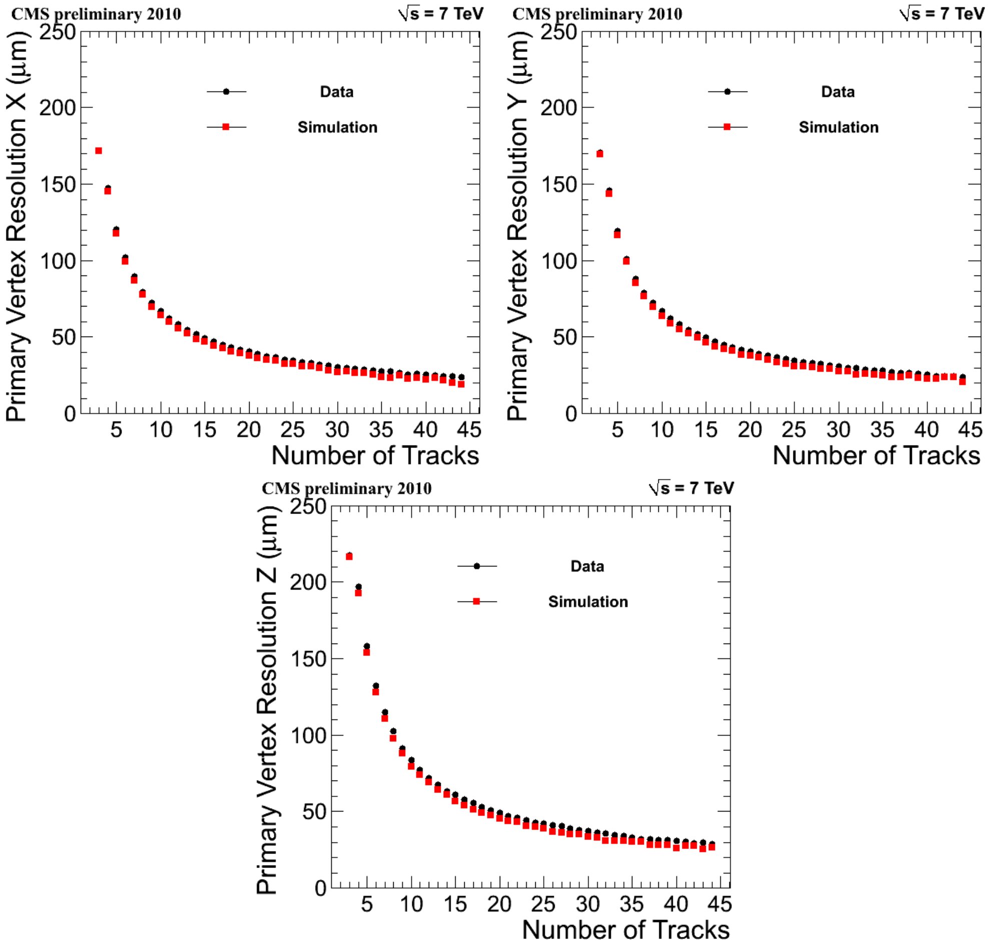

Figure 4.2: Primary vertex resolution in x (a), y (b), and z (c) as a function of the number of tracks used in the vertex fit for data and MC simulation [8].

4.2 Overview of the Monte Carlo Samples

The MC samples used in this thesis were produced by the CMS collaboration as part of the "Fall10" production sequence using CMS software (CMSSW) version 3_8_4_patch2. Events were generated with PYTHIA, and the Υ and J/ψ resonances were decayed using the PHOTOS program to introduce final-state radiation. GEANT4 was used for the detector simulation, followed by the L1 trigger emulation (the L1 trigger emulation task is to emulate bit-by-bit each L1 trigger subsystem), HLT processing, and the offline reconstruction.

Events containing an Υ or a J/ψ were generated at $\sqrt{s} = 7$ TeV within the NRQCD framework via the leading-order color-singlet and color-octet mechanisms. The long-distance matrix elements that are postulated to be universal were obtained from fits to the CDF data. In order to obviate time-consuming simulation and storage of events in which one or both muons are generated outside of the geometric acceptance of the detector, an event filter was implemented immediately after the event generation. The filter requires an event to have at least two muons (not necessarily from Υ or J/ψ decays) each with $|\eta| < 2.5$.

Table 4.3 summarizes the statistics, the effective integrated luminosity, and the effective cross sections (i.e., including the branching fraction to muons and the filter efficiency) of the MC samples.

Table 4.3: The name, number of events, effective cross sections (including branching fractions to muons and PYTHIA filter efficiency), and integrated luminosities for the MC samples.

Sample Name	# of Events (M)	$\sigma_{eff}(nb)$	$\int\mathscr{L}\mathrm{dt}(\mathrm{pb}^{-1})$
Upsilon1SToMuMu_2MuEtaFilter_7TeV-pythia6-evtgen/Fall10-START38_V12-v1	2.32	14.3	162.5
Upsilon2SToMuMu_2MuEtaFilter_7TeV-pythia6-evtgen/Fall10-START38_V12-v1	1.14	6.0	190.2
Upsilon3SToMuMu_2MuEtaFilter_7TeV-pythia6/Fall10-START38_V12-v1	0.92	1.6	566.5
JPsiToMuMu_2MuEtaFilter_7TeV-pythia6-evtgen/Fall10-START38_V12-v1	8.95	544.3	16.4

For the samples given in Table 4.3 the resonances are generated via the processes $pp \to \Upsilon(nS) + X$ or $pp \to J/\psi + X$, and the resonances are forced to decay by the processes $\Upsilon(nS) \to \mu^+\mu^-$ or $J/\psi \to \mu^+\mu^-$.

In addition to the above-mentioned MC samples, separate samples for the determination of the Υ acceptance are produced. In these acceptance samples, there are no other particles in the event other than the Υ, which is forced to decay to two muons, and its daughter muons.

Chapter 5

Data samples and online selection

The data samples used in this thesis were recorded by the CMS detector in pp collisions at $\sqrt{s} = 7$ TeV during 2010. The samples correspond to a total integrated luminosity of 36.7 ± 1.5 pb^{-1} [71].

Data are included for all periods where the silicon tracker, muon system, and trigger performed well and a luminosity measurement was available.

5.1 CMS Muon and Upsilon Triggers

As mentioned in Chapter 3, the CMS trigger system performs the online event selection in two steps: the level-1 (L1) trigger and the high-level trigger (HLT). The L1 trigger consists of custom-designed programmable electronics, whereas the HLT is a software program running on computer farms.

The muon trigger at L1 uses all three muon system: the DT, the CSC, and the RPC, and has local, regional, and global components. The endcap CSCs deliver three-dimensional track segments. The barrel DTs provide local trigger information in the form of track segments in the ϕ projection and hit patterns in the η projection. The regional muon trigger consists of the DT and CSC trackfinders that join segments to complete tracks and assign physical parameters to them. In addition, the RPC chambers deliver their own track candidates based on regional hit patterns. The global muon trigger then combines the information from the three muon detectors. The trigger candidates are ranked based on their momentum and quality, and the best four are sent to the HLT for further processing.

In the HLT, event selection is performed in two stages: level-2 (L2) and level-3 (L3). At L2, the L1 candidates are used to seed track reconstruction in the muon system. Starting from the seed, hits are included in the fit iteratively. The trajectory is extrapolated to the closest layer of detectors in each step. The local reconstruction is performed only in the chambers compatible with the extrapolated state in each detector layer. The procedure is repeated until the fit reaches the last station. The result is an updated track reaching the outermost muon station. Then, the updated track is used as a seed in a similar procedure, this time from the outermost muon station to the interaction point (defined by the beam-spot size: σ_{xy} is of the order 1 μm and σ_z is of the order 1 cm). The L2 reconstruction improves the p_T resolution. The typical p_T resolution for muons coming from low-mass resonances such as J/ψ and Υ is about 10% in the barrel, 16% in the endcaps and 21% in the overlap region. The improvement in the resolution with respect to what is used in the L1 trigger reduces the muon trigger rate by almost an order of magnitude.

More muon candidates were reconstructed with increasing instantaneous LHC luminosity. However, it was not possible to keep them all due to the limited bandwidth of the trigger system. Thus, only a fraction of the muon candidates were kept; this concept is called “pre-scaling”. At the end of L2, muon candidates are pre-scaled based on their pseudorapidity and transverse momentum. At L3, muon tracks are reconstructed using data from the silicon tracker. The reconstruction is performed using only pixel and strip hits in regions near the projections of the L2 muon candidates, in order to keep the execution time short. The final selection is based on the improved transverse momentum measurement of the muon candidates at L3. The typical p_T resolution for muons coming from low-mass resonances is about 0.8% in the barrel, 2% in the endcaps and 1.5% in the overlap region.

Table 5.1 shows the names of the selected muon trigger paths, their L1 seed, HLT thresholds, and pre-scale factors for three different instantaneous luminosities. There are two types of trigger paths in the table, single-muon trigger paths (first four rows) and di-muon trigger paths (last two rows). The same L1 seed can be used by more than one trigger path. The main difference between the single-muon trigger paths is the p_T threshold for the L3 muon. The “Pre-scale” column shows the pre-scale factors for different trigger paths with different instantaneous luminosities. For example, the pre-scale factor for HLT_Mu9 is 1 when the instantaneous luminosity is 2 $\times$

10^{31} cm^{-2}s^{-1} (2E31), and it is 30 when the instantaneous luminosity reaches 2×10^{32} cm^{-2}s^{-1}(2E32). Along with the increasing instantaneous luminosity, trigger paths with lower-p_T thresholds are pre-scaled and new trigger paths with higher-p_T thresholds are introduced.

Table 5.1: Some of the HLT muon trigger paths; names, L1 seeds, thresholds, and pre-scale factors for three different instantaneous luminosities [16].

HLT Path	L1 Seed	Threshold for L3 muon(s)	Pre-scale Factor		
			2E31	6E31	2E32
HLT_Mu3	L1_SingleMu3	$p_T > 3$ GeV/c	280	N/A	N/A
HLT_Mu5	L1_SingleMu3	$p_T > 5$ GeV/c	100	N/A	N/A
HLT_Mu9	L1_SingleMu7	$p_T > 9$ GeV/c	1	10	30
HLT_Mu11	L1_SingleMu7	$p_T > 11$ GeV/c	N/A	1	20
HLT_DoubleMu0	L1_DoubleMuOpen	no p_T requirement	1	N/A	N/A
HLT_DoubleMu0_Quarkonium_v1	L1_DoubleMuOpen	no p_T requirement	N/A	1	1

The data used in this thesis were collected with two trigger paths. The HLT_DoubleMu0 trigger path requires the detection of two L3 muons without an explicit p_T requirement. The two-dimentional distance in the transverse plane between each L3 muon and the beam spot must be less than 2 cm. The HLT_DoubleMu0 trigger was removed during data taking when the instantaneous luminosity reached 6×10^{31} cm^{-2}s^{-1} because of the high rate, and the HLT_DoubleMu0_Quarkonium_v1 trigger was used thereafter. The latter trigger requires two L3 muons with opposite sign and a di-muon invariant mass in the "quarkonium" mass window (1.5–14.5 GeV/c^2), in addition to the requirements imposed for the HLT_DoubleMu0 trigger.

5.2 Data Samples and Luminosity

The raw data collected with the HLT_DoubleMu0 trigger from CMS runs 146240 to 147116, correspond to an integrated luminosity of 5.40 pb^{-1}, while the HLT_DoubleMu0_Quarkonium_v1 trigger was used for runs 147196 to 149711, corresponding to an integrated luminosity of 31.34 pb^{-1}.

The total integrated luminosity of $\int \mathscr{L} \mathrm{dt} = 36.7 \pm 1.5$ pb^{-1} was measured for the two muon trigger paths using the forward hadronic calorimeter (HF). Two methods were used to extract a real-time relative luminosity. The first is a "zero-counting" method, in which the average fraction of empty calorimeter towers is used to infer the mean number of interactions per bunch crossing. The second method exploits the linear relationship between the average transverse energy per tower and the luminosity. The absolute luminosity is than calibrated using separation scans, a technique first pioneered by Van der Meer at the ISR [72]. The size and shape of the interaction region is measured by recording the relative interaction rate as a function of the transverse beam separation. For both methods, the uncertainty on the luminosity measurement is dominated by the measurement of the beam currents. Another source of uncertainty is due to the uncertainty of the beam shape. The total systematic uncertainty on the integrated luminosity is 4%. A detailed description of the procedure employed can be found in [71].

Chapter 6

Analysis Procedure

The measurement of the $\Upsilon(1S)$, $\Upsilon(2S)$, and $\Upsilon(3S)$ transverse momentum differential production cross sections, $d\sigma(\Upsilon(nS))/dp_T$, is performed in the di-muon decay channel, which has branching fractions of $(2.48 \pm 0.05)\%$, $(1.93 \pm 0.17)\%$ and $(2.18 \pm 0.21)\%$ for the $\Upsilon(1S)$, $\Upsilon(2S)$, and $\Upsilon(3S)$, respectively. The differential production cross sections are measured over the Υ rapidity range $|y| \leq 2.4$. The procedure can be summarized in the following expression:

$$\frac{d^2\sigma(pp \to \Upsilon(nS))}{dp_T dy} \times B(\Upsilon(nS) \to \mu^+\mu^-) = \frac{N_{fit}^{\Upsilon(nS)}(p_T, y)}{A \times \epsilon_{track} \times \epsilon_{id} \times \epsilon_{trig} \times \epsilon_{addsel} \times \int \mathscr{L} dt \times \Delta p_T \times \Delta y} \tag{6.1}$$

where

- $N_{fit}^{\Upsilon(nS)}(p_T, y)$ is the yield of $\Upsilon(nS)$ obtained from a fit to the di-muon invariant mass spectrum for a particular bin in p_T and y.
- $A(p_T^{\Upsilon}, y^{\Upsilon})$ is the geometric and kinematic acceptance of Υ candidates obtained from MC simulations.
- $\epsilon_{track}(p_T^{\Upsilon}, y^{\Upsilon})$ is the di-muon track reconstruction efficiency.
- $\epsilon_{id}(p_T^{\Upsilon}, y^{\Upsilon})$ and $\epsilon_{trig}(p_T^{\Upsilon}, y^{\Upsilon})$ are the di-muon identification and trigger efficiencies obtained with the "Tag-and-Probe" data-driven technique, discussed in Section 6.5.2.
- $\epsilon_{addsel}(p_T^{\Upsilon}, y^{\Upsilon})$ is the di-muon efficiency for additional selections, discussed in Section 6.5.6.

- $\int \mathscr{L} dt$ is the integrated luminosity.
- $\Delta p_T, \Delta y$ are the Υ transverse momentum and rapidity bin widths, respectively.

The track reconstruction, muon identification, and trigger efficiencies are first parametrized in terms of the muon transverse momentum and pseudorapidity for single muons. The di-muon efficiencies are then expressed from the single-muon efficiencies, $\epsilon_{\Upsilon}(p_T^{\Upsilon}, y^{\Upsilon}) = \epsilon_{\mu_1}(p_T^{\mu_1}, \eta^{\mu_1}) \times \epsilon_{\mu_2}(p_T^{\mu_2}, \eta^{\mu_2})$. The acceptance and efficiency for additional selection are directly parametrized in terms of the Υ transverse momentum and rapidity. Binned maximum likelihood fits are performed on the di-muon invariant mass distribution in bins of the Υ candidate p_T and rapidity, and the signal yields are corrected for the average acceptance and efficiencies in the same region of kinematics.

The p_T differential cross sections are separately extracted for each of the three upsilon states and for each of the following rapidity ranges: $|y| \leq 0.4$, $0.4 < |y| \leq 0.8$, $0.8 < |y| \leq 1.2$, $1.2 < |y| \leq 1.6$, $1.6 < |y| \leq 2.0$, $2.0 < |y| \leq 2.4$. The ratios of the integrated cross sections for $\Upsilon(2S)/\Upsilon(1S)$ and $\Upsilon(3S)/\Upsilon(1S)$ are also determined as functions of p_T and $|y|$. The p_T-integrated, differential rapidity cross sections are extracted for all three upsilon states, as well.

6.1 Muon Reconstruction

The muon reconstruction was discussed in Section 3.2.5.1, this is a short summary of the three different muon types [73]:

Standalone muons are tracks that have been reconstructed in the muon system only. Hits in the CSC and DT layers are aggregated into segments. The tracking algorithm requires at least two segments in the CSC/DT, or one segment in the CSC/DT and one RPC hit. The final track fit uses the beam spot as a constraint.

Global muon reconstruction starts from a standalone muon track and finds matching tracks in the silicon tracker. A global fit is performed using the hits of both tracks. The combined track with the best normalized χ^2 is identified as a global muon track.

Tracker muons are tracks in the silicon tracker that are identified as a muon track if the extrapolation to the muon system matches at least one muon segment in the CSC or DT.

In the Υ signal selection for the cross section measurement, tracker muons are used. The pseudorapidity coverage for muon reconstruction is $|\eta| \leq 2.4$. Tracks in the silicon tracker are reconstructed using a Kalman-filter technique, which starts from hits in the pixel system and extrapolates outward to the silicon strip tracker.

6.2 Offline Selection

The soft momentum ($p_T \leq 10$ GeV/c) spectrum of muons from the decay of the $\Upsilon(nS)$ motivates the choice of using tracker muons since that reconstruction algorithm has the highest efficiency for this range of momentum. Upsilon candidates are reconstructed from pairs of, what are called, arbitrated tracker muon tracks. In the reconstruction, a given muon chamber segment can be associated with more than one silicon track, *i.e.*, reconstructed tracker muons are allowed to share segments. Arbitration is the pattern recognition process that assigns each segment uniquely to a single tracker muon.

The arbitration algorithm works as follows: assume that one segment is associated with more than one tracker muon. For each tracker muon, the quantity $\Delta R^2 = \Delta X^2 + \Delta Y^2$ is calculated, where ΔX and ΔY are the distances between the extrapolated silicon track and the segment in the local CSC/DT X and Y coordinates. The segment is uniquely associated with the tracker muon for which ΔR is smallest. Once the muon segments are uniquely assigned, the full track fit is repeated, and the resulting tracks are used in this analysis. Further details can be found in [73].

The detection criteria for muons coming from Υ decay are that each muon should lie within the geometric and kinematic acceptance of the muon detectors, $|\eta^\mu| \leq 2.4$ and $p_T^\mu > 3$ GeV/c in the central pseudorapidity region. The distribution contours of muons from $\Upsilon(1S)$ decay in the (p, η) and (p_T, η) planes are shown in Figure 6.1 (left) and (right), respectively.

The acceptance contours in the (p, η) and (p_T, η) planes are shown in Figure 6.2 (left) and (right), respectively. Muons are required to satisfy:

$$(p_T \geq 4 \text{ GeV/c} \;\text{ if }\; |\eta| \leq 1.2) \;\text{ or }\; (p_T \geq 3 \text{ GeV/c} \;\text{ if }\; 1.2 < |\eta| \leq 2.4). \tag{6.2}$$

These kinematic acceptance criteria are chosen to ensure that the trigger and muon reconstruction efficiencies are high and not rapidly changing.

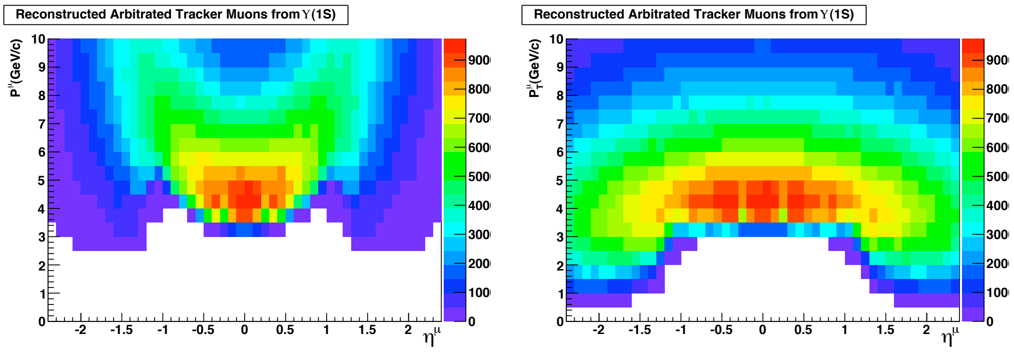

Figure 6.1: Distribution of muons from $\Upsilon(1S)$ decay, (left) as a function of p versus η, and (right) as a function of p_T versus η. The color scale shows the number of muons in a given cell.

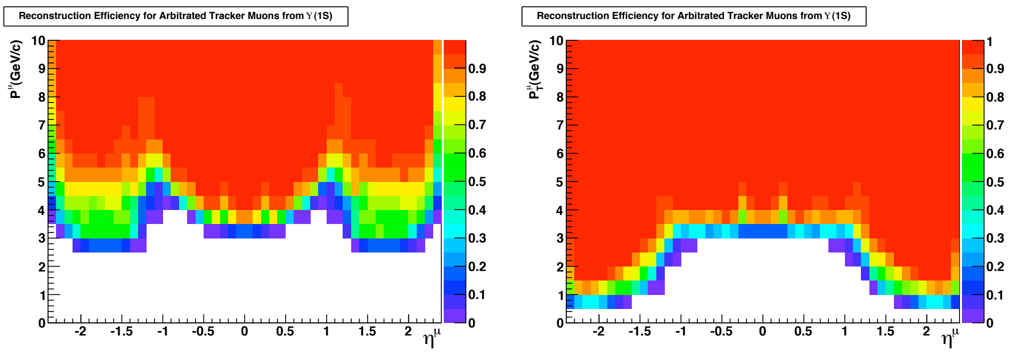

Figure 6.2: Acceptance contours of the muons from $\Upsilon(1S)$, (left) as a function of p versus η, and (right) as a function of p_T versus η. The color scale shows the muon acceptance in a given cell.

The momentum measurement of charged tracks in the CMS detector is affected by systematic uncertainties caused by imperfect knowledge of the magnetic field, the material budget model, and sub-detector misalignments, as well as by biases in the algorithms that fit the track trajectory. The mismeasurement of the track momentum shifts and broadens the reconstructed peaks of the di-muon resonances. The momentum measurement is corrected with data collected from cosmic-ray muons and pp collisions [74, 75, 76]. The residual effects are determined by studying the dependence of the reconstructed J/ψ di-muon invariant mass distribution on the muon transverse momentum and pseudorapidity. The residual relative correction is parametrized as

$$p_T^{corr} = (a + b|\eta|)p_T, \tag{6.3}$$

where p_T and p_T^{corr} are the uncorrected and corrected transverse momentum, with a = $(3.8 \pm 1.9)\times 10^{-4}$, and b = $(3.0 \pm 0.7)\times 10^{-4}$ found from fits to the data [77].

6.3 Fits to the Di-muon Invariant Mass Spectrum

In order to identify events containing an Υ decay, muons with opposite charge are paired, and the invariant mass of the muon pair is required to be between 8.7 and 11.2 GeV/c^2. The rapidity, y, of the Υ candidates is required to satisfy $|y| \leq 2.4$ because the acceptance diminishes rapidly at larger rapidity. The Υ rapidity is defined as $y = \frac{1}{2}\ln(\frac{E+p_{||}}{E-p_{||}})$, where E is the energy and $p_{||}$ is the momentum parallel to the beam axis of the muon pair.

The $\Upsilon(1S)$, $\Upsilon(2S)$, and $\Upsilon(3S)$ yields are extracted via a binned maximum-likelihood fit to the di-muon invariant mass distribution. The measured lineshape of each Υ state is parametrized by a "Crystal Ball" (CB) function [78];

$$f(x;\alpha,n,\bar{x},\sigma) = N \cdot \begin{cases} exp(-\frac{(x-\bar{x})^2}{2\sigma^2}), & \text{for } \frac{x-\bar{x}}{\sigma} > -\alpha \\ A \cdot (B - \frac{x-\bar{x}}{\sigma})^{-n}, & \text{for } \frac{x-\bar{x}}{\sigma} \leq -\alpha \end{cases} \tag{6.4}$$

where A = $(\frac{n}{|\alpha|})^n \cdot exp(-\frac{|\alpha|^2}{2})$ and B = $\frac{n}{|\alpha|} - |\alpha|$. This is a Gaussian resolution function with the low-side tail replaced with a power law describing final-state radiation (FSR). The parameters $\bar{x}$ and σ are the Gaussian mean and standard deviation, respectively. The parameters α and n define the FSR tail, α is the crossover point and n is the length of the tail. The parameter N is the normalization. The FSR tail is fixed to the MC shape. The di-muon mass spectrum in the MC was fit by letting the FSR tail parameters float and fixing those parameters when fitting the data to their MC values. Figure 6.3 shows an example CB shape for different FSR tail parameters with the same $\bar{x}$ and σ. Figure 6.4 shows MC fits for two different rapidity ranges with the values of the tail parameters.

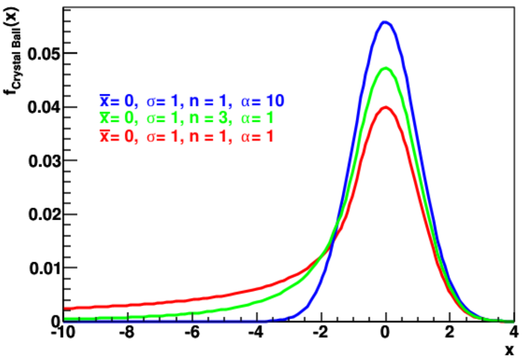

Figure 6.3: Example CB function shape for different FSR tail parameters.

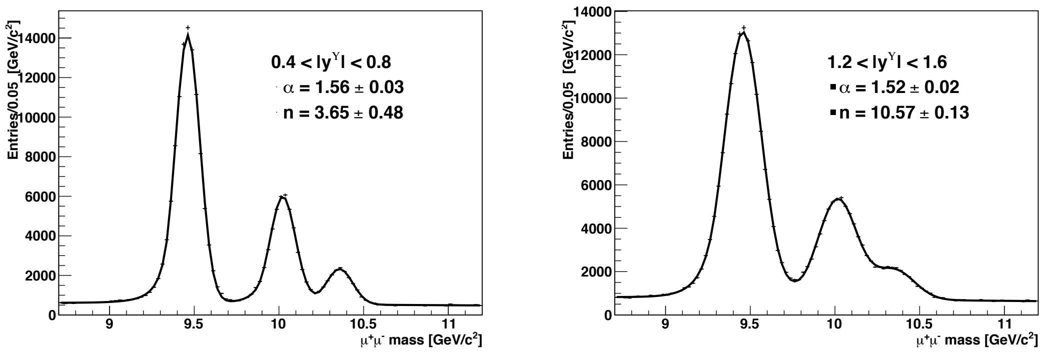

Figure 6.4: The di-muon invariant mass distribution from MC in the vicinity of the $\Upsilon(nS)$ resonances for $p_T \leq 50$ GeV/c with $0.4 < |y^\Upsilon| < 0.8$ (left), and $1.2 < |y^\Upsilon| < 1.6$ (right). The results of the fits are shown by the solid lines.

Since the three resonances overlap in the measured di-muon mass spectrum, the three $\Upsilon(nS)$ states are fitted simultaneously. Therefore, the probability distribution function describing the signal consists of three CB functions. The Gaussian standard deviation (σ), and the mean ($\bar{x}$), are free parameters for the $\Upsilon(1S)$ and $\Upsilon(2S)$, but for $\Upsilon(3S)$ they are constrained to scale with the ratio of the $\Upsilon(3S)$ to $\Upsilon(2S)$ world-average mass value. A first-degree polynomial is chosen to describe the background in the 8.7-11.2 GeV/c^2 mass-fit range.

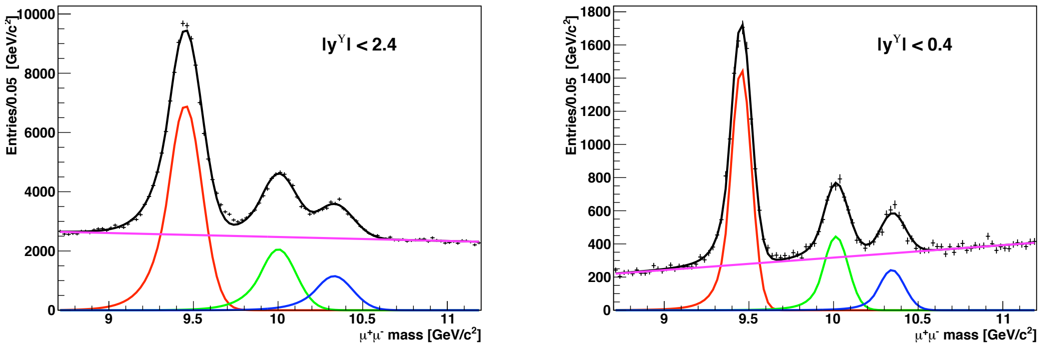

Figure 6.5: The di-muon invariant mass distribution from data in the vicinity of the $\Upsilon(nS)$ resonances for $p_T \leq 50$ GeV/c with $|y^{\Upsilon}| < 2.4$ (left), and $|y^{\Upsilon}| < 0.4$ (right). The results of the fits are shown by the solid lines.

The di-muon invariant mass spectrum from data in the $\Upsilon(nS)$ region for $p_T <$ 50 GeV/c is shown in Figure 6.5 for $|y^{\Upsilon}| < 2.4$ and $|y^{\Upsilon}| < 0.4$, and the ten p_T intervals used for the $\Upsilon(1S)$ differential cross section measurement in Figure 6.6. The results of the fits are shown by the curves in both sets of plots. The observed signal yields are reported in Table 6.1 for all three resonances in bins of p_T. For all three resonances, yields from the combined fits are in good agreement with the sum of the yields from the fits in bins of p_T. The total $\Upsilon(1S)$, $\Upsilon(2S)$, and $\Upsilon(3S)$ yields are: 73,569 $\pm$ 465, 23,390 $\pm$ 364, and 13,359 $\pm$ 130, respectively.

The $\Upsilon(1S)$ mass resolution and mean, given by the Gaussian width and mean fit parameters, are shown in Figures 6.7 and 6.8 as a function of the $\Upsilon(1S)$ rapidity and p_T. From the fit to the data, the $\Upsilon(1S)$ mass resolution of 99.7 $\pm$ 0.7 MeV/c^2 and mean of 9451 $\pm$ 0.6 MeV/c^2 are obtained for the entire rapidity range $|y^{\Upsilon}| \leq 2.4$. The mass resolution and mean from the MC fit are 91.6 $\pm$ 0.2 MeV/c^2 and 9462 $\pm$ 0.2 MeV/c^2 respectively.

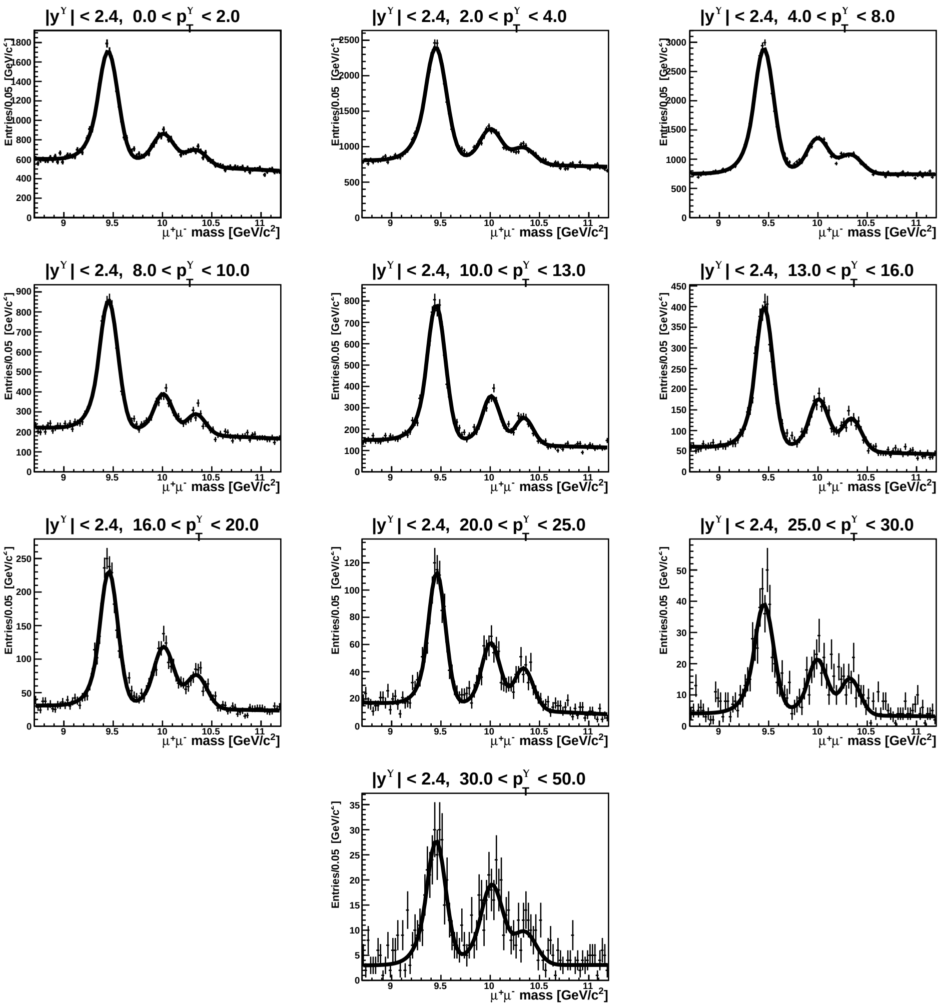

Figure 6.6: The di-muon invariant mass distribution for different p_T. The results of the fits are shown by the solid lines.

Table 6.1: Measured Υ signal yields in different p_T regions for the 3 Υ resonances. The sum of all the p_T bins and the sum from the fit to the combined invariant mass distribution are also given.

p_T (GeV/c)	signal yield	p_T (GeV/c)	signal yield	p_T (GeV/c)	signal yield
$\Upsilon(1S)$		$\Upsilon(2S)$		$\Upsilon(3S)$	
0.00 - 2.00	12341 ± 201	0.00 - 2.00	3631 ± 162	0.00 - 2.00	2064 ± 73
2.00 - 4.00	18675 ± 246	2.00 - 4.00	5650 ± 199	2.00 - 4.00	2945 ± 72
4.00 - 8.00	22692 ± 255	4.00 - 8.00	7033 ± 205	4.00 - 8.00	4091 ± 44
8.00 - 10.00	6586 ± 135	8.00 - 10.00	1923 ± 93	8.00 - 10.00	1086 ± 41
10.00 - 13.00	6487 ± 129	10.00 - 13.00	2104 ± 84	10.00 - 13.00	1226 ± 29
13.00 - 16.00	3315 ± 88	13.00 - 16.00	1263 ± 63	13.00 - 16.00	869 ± 24
16.00 - 20.00	1983 ± 68	16.00 - 20.00	962 ± 52	16.00 - 20.00	567 ± 22
20.00 - 25.00	899 ± 46	20.00 - 25.00	460 ± 35	20.00 - 25.00	311 ± 17
25.00 - 30.00	351 ± 29	25.00 - 30.00	184 ± 24	25.00 - 30.00	121 ± 18
30.00 - 50.00	240 ± 24	30.00 - 50.00	180 ± 24	30.00 - 50.00	78 ± 14
sum	73569 ± 465	sum	23390 ± 364	sum	13359 ± 130
combined fit	73290 ± 462	combined fit	23216 ± 360	combined fit	13273 ± 126

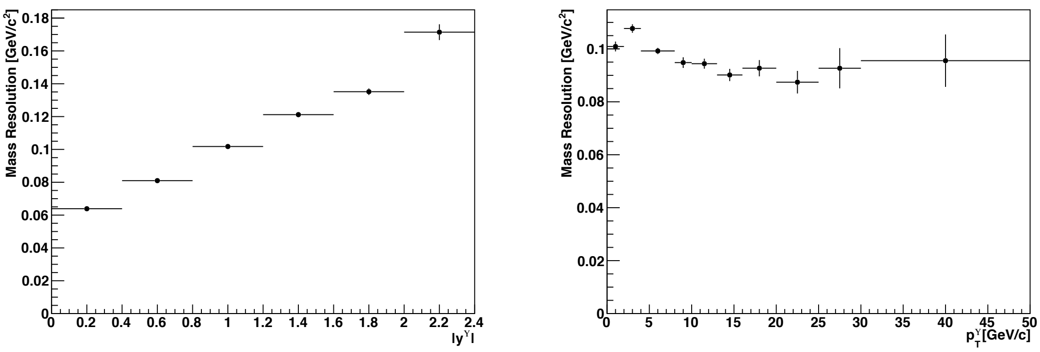

Figure 6.7: The $\Upsilon(1S)$ mass resolution as a function of rapidity (left) and p_T (right) from fits to the invariant mass distributions from data.

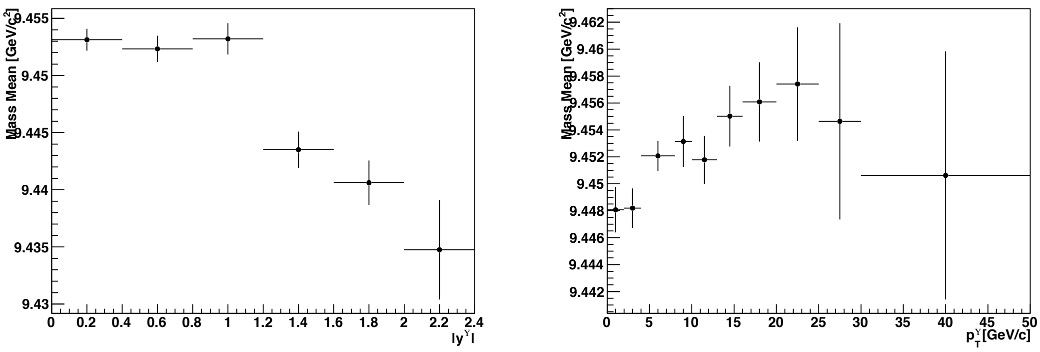

Figure 6.8: The $\Upsilon(1S)$ mass mean as a function of rapidity (left) and p_T (right) from fits to the invariant mass distributions from data.

6.4 Acceptance

The muon system covers the pseudorapidity range $|\eta| < 2.4$ with drift tube (DT) and cathode strip chamber (CSC) detectors. In addition, resistive plate chambers (RPC), which enhance the triggering capability, are installed in the range $|\eta| < 1.6$. Due to ionization energy losses, muons with transverse momentum $p_T \leq 3$ GeV/c in the central pseudorapidity region do not reach the muon system.

The calculation of the acceptance for $\Upsilon \rightarrow \mu^+\mu^-$ takes into account the finite geometrical coverage of the detector and the limited kinematic acceptance of the reconstruction system. The acceptance is measured for $\Upsilon(1S)$, $\Upsilon(2S)$, and $\Upsilon(3S)$ using a MC simulation, and then parametrized as a function of the p_T and y of the Υ. The acceptance is defined as the fraction of detectable $\Upsilon \rightarrow \mu^+\mu^-$ decays to the number of generated upsilons,

$$A(p_T^\Upsilon, y^\Upsilon) = \frac{N^{det}(p_T^\Upsilon, y^\Upsilon|\text{generated muon pair satisfing Eq. 6.2})}{N^{gen}(p_T^\Upsilon, y^\Upsilon)}, \tag{6.5}$$

where N^{gen} is the total number of generated upsilons in a (p_T^Υ, y^Υ) bin, while N^{det} is the number of detectable upsilons with both daughter muons satisfying Eq. 6.2 in the corresponding (p_T^Υ, y^Υ) bin.

The acceptance is measured using a Υ production Monte Carlo generator and forcing the Υ to decay to two muons. There are no particles in the event besides the Υ and its daughter muons. The acceptance is determined for bins of the generated Υ p_T and y.

The two-dimensional (2D) $|y|$ versus p_T map of the $\Upsilon(1S)$ acceptance for the unpolarized scenario and the projection of the unpolarized-Υ acceptance as a function of p_T are shown in Figure 6.9. There are no accepted events beyond $|y| = 2.4$. In the vicinity of $p_T = 5$ GeV/c, the acceptance reaches a minimum, mainly as a result of the softer μ failing the p_T cut. For $p_T < 5$ GeV/c, muons tend to be produced back to back, due to the low p_T of the Υ, with transverse momenta higher than the transverse momentum of the softer μ in the upsilon $p_T = 5$ GeV/c case. The average values of the acceptance are given in Tables 6.2 and 6.3 in bins of p_T; statistical uncertainties on the average values are all around 0.1%.

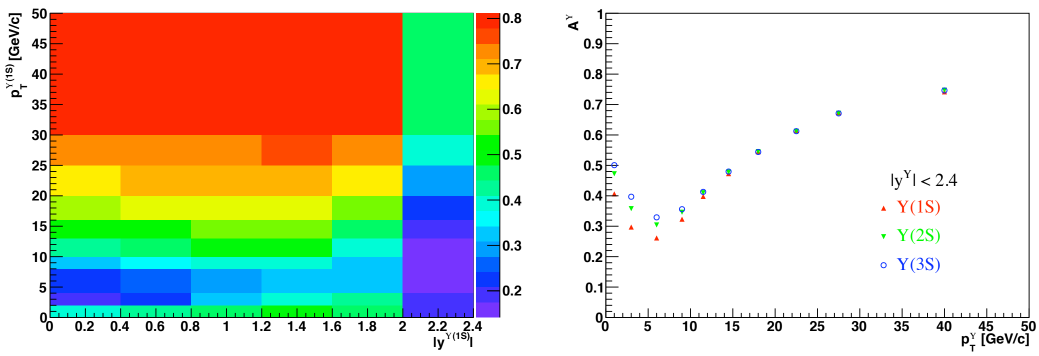

Figure 6.9: The unpolarized-$\Upsilon(1S)$ acceptance as a function of p_T and y (left), and the unpolarized $\Upsilon(1S)$, $\Upsilon(2S)$, and $\Upsilon(3S)$ acceptances integrated over rapidity $|y| \leq 2.4$ as a function of p_T (right).

The unknown polarization of the Υ strongly influences the muon angular distributions and is predicted to change as a function of p_T^{Υ}. In order to account for this, the acceptance is found from simulation with five separate assumptions for the polarization: unpolarized, and polarized longitudinally and transversely with respect to two different reference frames. The first is the helicity frame, defined by the direction of the upsilon boost direction in the upsilon rest frame. The second, the Collins-Soper frame [79], is an approximation to the frame connecting the incoming partons in the collision, defined by the bisection of the incoming hadron directions in the upsilon rest frame. Even though not used in this thesis, there is yet another reference frame, the Gottfried-Jackson frame, which is defined by the direction of the momentum of one of the two colliding beams. Illustrations of the two frames are shown in Figure 6.10. The

Table 6.2: $\Upsilon(1S)$ acceptance A^{Υ} for five different polarization scenarios; unpolarized (UNPOL), transversely polarized in the helicity frame (HX T), longitudinally polarized in the helicity frame (HX L), transversely polarized in the Collins-Soper frame (CS T), and longitudinally polarized in the Collins-Soper frame (CS L), in bins of p_T for $|y| \leq 2.4$. The statistical uncertainties on the values are all about 0.1%.

p_T (GeV/c)	A^{Υ}				
	UNPOL	HX T	HX L	CS T	CS L
$\Upsilon(1S)$					
0.00 - 2.00	0.4064	0.3337	0.5515	0.3312	0.5565
2.00 - 4.00	0.2972	0.2430	0.4056	0.2435	0.4048
4.00 - 8.00	0.2614	0.2178	0.3485	0.2264	0.3313
8.00 - 10.00	0.3231	0.2740	0.4214	0.3078	0.3538
10.00 - 13.00	0.3979	0.3415	0.5108	0.3972	0.3995
13.00 - 16.00	0.4729	0.4099	0.5989	0.4835	0.4516
16.00 - 20.00	0.5450	0.4786	0.6779	0.5637	0.5077
20.00 - 25.00	0.6144	0.5474	0.7487	0.6377	0.5679
25.00 - 30.00	0.6734	0.6083	0.8036	0.6984	0.6232
30.00 - 50.00	0.7417	0.6827	0.8599	0.7659	0.6934

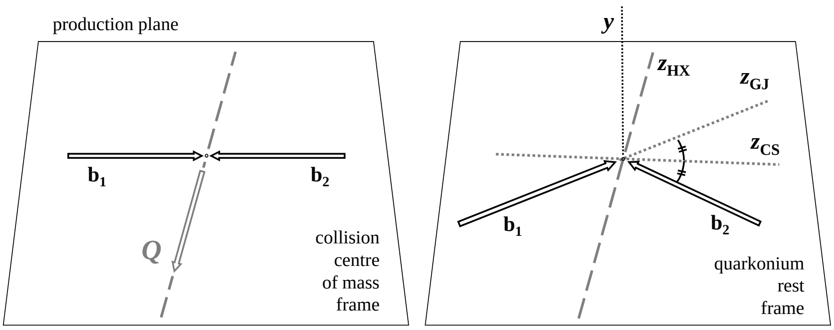

Figure 6.10: Left plot shows the directions of motion of the two colliding beams (b_1, b_2) and the quarkonium (Q) in the collision center-of-mass frame. Right plot illustrates the three definitions of the polarization axis z (CS: Collins-Soper, GJ: Gottfried-Jackson, HX: helicity) with respect to the directions of motion of the two colliding beams (b_1, b_2) and of the quarkonium (Q) [9].

Table 6.3: $\Upsilon(2S)$ and $\Upsilon(3S)$ acceptances A^{Υ} for five different polarization scenarios; unpolarized (UNPOL), transversely polarized in the helicity frame (HX T), longitudinally polarized in the helicity frame (HX L), transversely polarized in the Collins-Soper frame (CS T), and longitudinally polarized in the Collins-Soper frame (CS L), in bins of p_T for $|y| \leq 2.4$. The statistical uncertainties on the values are all about 0.1%.

p_T (GeV/c)	A^{Υ}				
	UNPOL	HX T	HX L	CS T	CS L
$\Upsilon(2S)$					
0.00 - 2.00	0.4725	0.3966	0.6244	0.3916	0.6343
2.00 - 4.00	0.3578	0.2971	0.4795	0.2960	0.4816
4.00 - 8.00	0.3042	0.2562	0.4003	0.2632	0.3863
8.00 - 10.00	0.3460	0.2960	0.4456	0.3272	0.3834
10.00 - 13.00	0.4103	0.3545	0.5216	0.4063	0.4182
13.00 - 16.00	0.4778	0.4169	0.5995	0.4858	0.4618
16.00 - 20.00	0.5454	0.4812	0.6734	0.5616	0.5130
20.00 - 25.00	0.6123	0.5469	0.7432	0.6342	0.5685
25.00 - 30.00	0.6714	0.6076	0.7992	0.6954	0.6235
30.00 - 50.00	0.7472	0.6899	0.8618	0.7704	0.7007
$\Upsilon(3S)$					
0.00 - 2.00	0.5007	0.4241	0.6542	0.4185	0.6654
2.00 - 4.00	0.3970	0.3333	0.5246	0.3301	0.5307
4.00 - 8.00	0.3292	0.2791	0.4291	0.2849	0.4177
8.00 - 10.00	0.3560	0.3058	0.4563	0.3354	0.3970
10.00 - 13.00	0.4129	0.3578	0.5233	0.4077	0.4233
13.00 - 16.00	0.4797	0.4197	0.6002	0.4870	0.4653
16.00 - 20.00	0.5441	0.4808	0.6708	0.5591	0.5141
20.00 - 25.00	0.6125	0.5486	0.7402	0.6331	0.5711
25.00 - 30.00	0.6709	0.6082	0.7963	0.6939	0.6250
30.00 - 50.00	0.7463	0.6897	0.8595	0.7691	0.7009

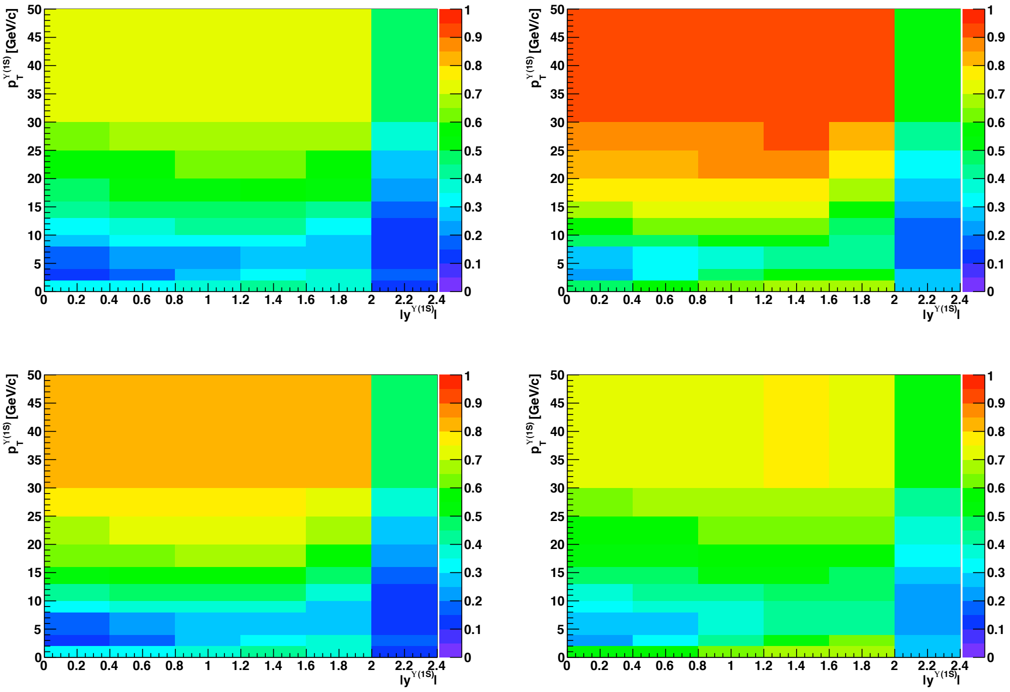

Figure 6.11: The $\Upsilon(1S)$ acceptance for the four polarized scenarios: (upper left) transverse polarization in the helicity frame, (upper right) longitudinal polarization in the helicity frame, (lower left) transverse polarization in the Collins-Soper frame, and (lower right) longitudinal polarization in the Collins-Soper frame.

2D $\Upsilon(1S)$ acceptance as a function of y^{Υ} and p_T^{Υ} for each of the polarization scenarios is shown in Figure 6.11. Comparisons as a function of $p_T^{\Upsilon(1S)}$ and $y^{\Upsilon(1S)}$ are shown in Figure 6.12. They are obtained from a sample of 4 million generated unpolarized $\Upsilon(1S)$ MC events.

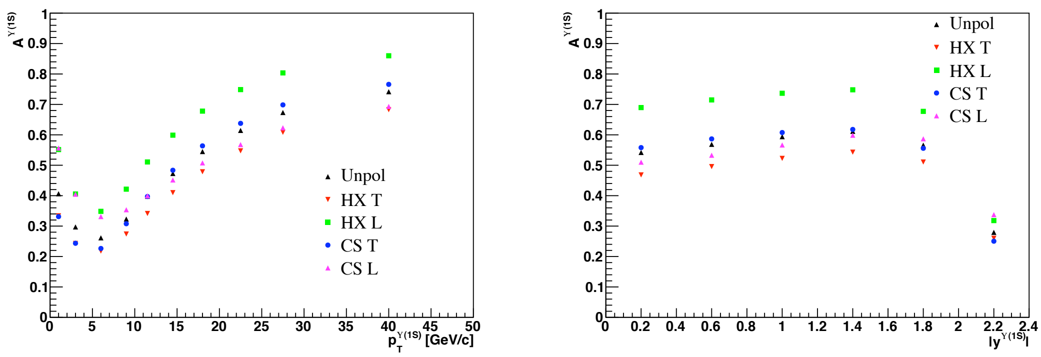

Figure 6.12: $\Upsilon(1S)$ acceptance for the unpolarized and four polarized scenarios as a function of p_T for $|y| \leq 2.4$ (left) and rapidity for $p_T \leq 50$ GeV/c (right).

6.5 Efficiencies

The total muon efficiency can be factorized into three conditional terms:

$$\epsilon(total) = \epsilon(trig|id) \times \epsilon(id|track) \times \epsilon(track|detectable) \equiv \epsilon_{trig} \times \epsilon_{id} \times \epsilon_{track}, \quad (6.6)$$

where:

- ϵ_{track} is the muon tracking efficiency, i.e., the efficiency that a detectable muon from a $\Upsilon(nS)$ decay within the detector acceptance is found as a track in the silicon tracker. It is determined with the track-embedding technique, discussed below.

- ϵ_{id} is the muon identification efficiency, i.e., the efficiency that a reconstructed muon track is identified as a muon. It is measured with the tag-and-probe method, discussed in Section 6.5.2.

- ϵ_{trig} is the muon trigger efficiency, i.e., the efficiency that an identified muon is matched to a trigger object, also measured with the tag-and-probe method.

6.5.1 Tracking Efficiency

The absolute track reconstruction efficiency in pp collisions is difficult to precisely quantify using data because of the lack of a pure, high-statistics sample of tracks with known kinematic properties that is free from selection or trigger bias. Nonetheless, by removing the single-track acceptance, which is a geometric quantity calculable using the material model of the detector in the Monte Carlo simulation, the major factor that contributes to the tracking inefficiency is expected to be pattern-recognition failures in the tracking algorithms. Such failures can result when hits associated with a track are lost or when hits not associated with a track are incorrectly included in the track's trajectory fit. Both effects are expected to be driven by the tracker occupancy in the vicinity of the track in question, for which the accuracy of a simulation can be difficult to quantify. Instead, an estimate of the absolute track reconstruction efficiency, with respect to which the muon identification efficiencies are defined, is found by measuring the fraction of simulated tracks that fail to be reconstructed after superimposing their hits into real events from pp collisions recorded at $\sqrt{s} = 7$ TeV.

The track-embedding procedure is described in Ref. [80], and follows closely the approach used by the CDF experiment. A sample of pp collision events is analyzed and the position of the primary vertex in each event is determined. Simulated muons with p_T ranging from 0.5 to 500 GeV/c and with pseudorapidity in the range $|\eta| \leq 3$ are generated with initial positions corresponding to the primary vertices reconstructed in the data. These simulated muons are processed using the Monte Carlo detector simulation and event reconstruction procedure and are classified as being within the detector acceptance if a reconstructed track is found that had at least 75% of its hits originating from the generated muon. The pixel and strip detector hits from the pp collision are then merged with the simulated muon hits and the event reconstruction is repeated. The tracking inefficiency is calculated from the fraction of embedded tracks that fail to be reconstructed after superimposing hits from pp collision events. The measured efficiencies are given in Table 6.4. All are greater than 99%.

With this procedure, it is found that the pixel and silicon tracker occupancies observed in the data result in a loss of track reconstruction efficiency of less than 0.5% for muons with $p_T > 1$ GeV/c and $|\eta| \leq 2.4$.

Table 6.4: Track reconstruction efficiencies as a function of p_T and η for muons in 7 TeV data, found from the track-embedding procedure. The uncertainties shown are statistical only.

η	p_T (GeV/c)				
	0.5 - 2	2 - 5	5 - 10	10 - 20	20 - 50
-2.4 – -2.1	$.9999^{+.0001}_{-.0016}$	$.9981\pm.0013$	$.9990\pm.0010$	$.9989\pm.0011$	$.9990\pm.0010$
-2.1 – -1.2	$.9982\pm.0009$	$.9987\pm.0007$	$.9980\pm.0008$	$.9987\pm.0007$	$.9994\pm.0005$
-1.2 – -0.8	$.9970\pm.0017$	$.9999^{+.0001}_{-.0009}$	$.9978\pm.0013$	$.9993\pm.0007$	$.9999^{+.0001}_{-.0009}$
-0.8 – 0.8	$.9967\pm.0009$	$.9981\pm.0006$	$.9971\pm.0007$	$.9977\pm.0007$	$.9989\pm.0005$
0.8 – 1.2	$.9960\pm.0020$	$.9992\pm.0008$	$.9992\pm.0008$	$.9985\pm.0011$	$.9999^{+.0001}_{-.0010}$
1.2 – 2.1	$.9978\pm.0010$	$.9970\pm.0010$	$.9993\pm.0005$	$.9984\pm.0007$	$.9993\pm.0005$
2.1 – 2.4	$.9999^{+.0001}_{-.0015}$	$.9999^{+.0001}_{-.0012}$	$.9999^{+.0001}_{-.0012}$	$.9990\pm.0010$	$.9999^{+.0001}_{-.0012}$

6.5.2 Tag-and-Probe Method

"Tag-and-Probe" (TNP) [81, 82] is a data-driven method used in this analysis to determine muon identification and trigger efficiencies. It utilizes well-known di-muon decays, e.g., $J/\psi \to \mu^+\mu^-$, to provide a sample of probe objects. A well-identified muon, called the tag, is combined with a second object, called the probe, in the event and their invariant mass is computed. The tag-probe pairs are divided into two samples based on whether the probe satisfies the criteria for the efficiency being measured. The tag-probe mass distribution of each sample contains a J/ψ peak, the area of which corresponds to the number of probes from the decay that satisfy or fail to satisfy the criteria imposed, respectively. The efficiency is extracted from binned maximum-likelihood fits to each mass distribution.

In order to obtain a precise determination of the efficiencies via the TNP method, the J/ψ resonance is utilized since it provides a larger yield than the Υ resonances and, moreover, a statistically independent sample [83]. The events are collected for invariant masses within a J/ψ mass window [2.8-3.4] GeV/c^2.

The tag muons are required to have $p_T \geq 3$ GeV/c and $|\eta| \leq 2.4$ and be identified as arbitrated tracker muons. Furthermore, to avoid trigger biases on the probe sample, the tag is required to satisfy the trigger requirements, i.e., the tag muon must have fired the HLT_Mu11 trigger, used to collect the data sample. This ensures that the tag muon was the reason that the event was triggered, so no bias is introduced on the probe sample. Figure 6.13 shows some examples of fits for two samples of tag-probe pairs used to determine the muon identification efficiency in the muon kinematic region -0.4 $< \eta^\mu <$ 0.4 and 3 GeV/c $< p_T <$ 4 GeV/c.

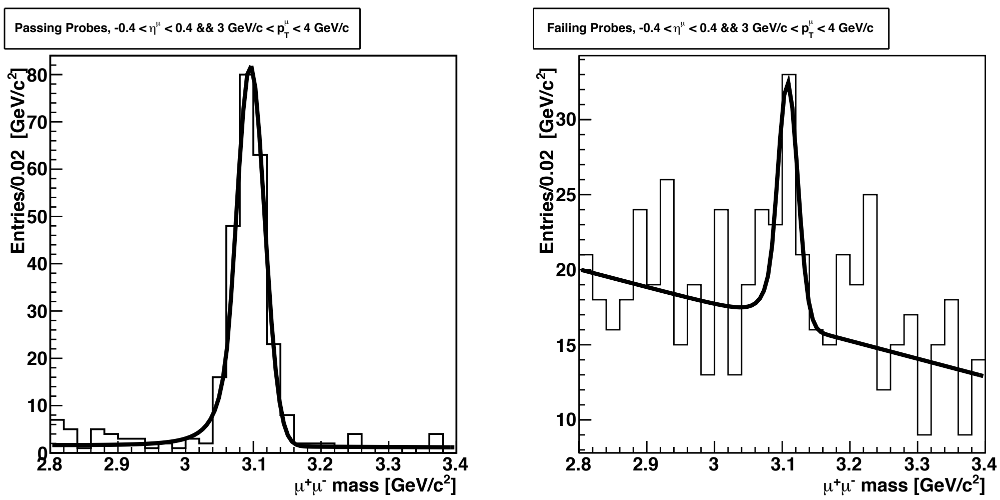

Figure 6.13: Di-muon invariant mass distributions of tag-probe pairs satisfying the muon identification criteria (left) and failing the muon identification criteria (right) in the probe muon kinematic region -0.4 $< \eta^\mu <$ 0.4 and 3 GeV/c $< p_T <$ 4 GeV/c.

The measurement of the muon identification and trigger efficiencies can be more complicated when the two muon tracks are close enough to each other so that they hit the same muon detector. They can then be reconstructed as one muon and/or fire the single-muon trigger instead of the double-muon trigger. This situation needs to be considered when dealing with two muons from the J/ψ resonance; the di-muons that bend towards each other (type-1) in the magnetic field, at low p_T and in the forward region, may cross again in a muon station, whereas the di-muons that bend away from each other (type-2) have no chance of crossing at the muon stations again [84]. In this study, J/ψ events with type-1 muons are not used for the TNP efficiency calculations in order to bypass the complication mentioned above.

6.5.3 Single-Muon Identification Efficiency

The data sample used for the determination of the single-muon identification and trigger efficiencies via the TNP method is that specified in Chapter 5, corresponding to an integrated luminosity of 31.34 pb^{-1} and CMS runs from 147196 to 149711, during which the data were collected with the HLT_DoubleMu0_Quarkonium_v1 trigger.

The probes for the muon identification efficiency measurement are tracks reconstructed in the silicon tracker, and the successful probes are those that are matched muon candidates satisfying the muon identification and selection requirements defined in Section 6.2.

The single-muon identification efficiencies as a function of p_T^{μ} for five η^{μ} regions are shown in Table 6.5 and Figure 6.14. No values are provided for the range $3 < p_T < 4$ GeV/c and $|\eta| < 1.2$ due to the phase space cut in Eq. 6.2.

Because of the number of reconstructed J/ψ mesons, the TNP method has limited statistics. The lack of statistics is the reason for the fluctuations of the TNP points in Figure 6.14, which is not the case for the TNP MC points, also shown in Figure 6.14, since there are more statistics in the MC simulation. The large required p_T and η bin sizes are another difficult issue. There might be different distributions within a bin for TNP sample and the physics sample. Assigning a single value for the entire bin range is not a good way of estimating the efficiency. In order to limit the effects of the fluctuations and the large bin sizes, the TNP efficiency points are fit to a smooth function. The details of the fit are given in Sec. 6.5.5.

Table 6.5: Single-muon identification efficiencies from the J/ψ TNP method; the uncertainties are statistical only.

η	p_T (GeV/c)							
	3 - 4	4 - 5	5 - 6	6 - 8	8 - 10	10 - 14	14 - 20	20 - 50
-2.4 – -1.2	.907±.014	.976±.008	.909±.020	.960±.011	.954±.018	.951±.016	.899±.034	.750±.064
-1.2 – -0.4	-	.997±.003	.955±.013	.965±.010	.976±.010	.976±.011	.934±.023	.948±.025
-0.4 – 0.4	-	.997±.003	.996±.004	.895±.016	.869±.022	.948±.014	.980±.013	.984±.013
0.4 – 1.2	-	.962±.010	.940±.014	.982±.007	.995±.005	.995±.005	.967±.018	.888±.033
1.2 – 2.4	.949±.010	.979±.008	.961±.012	.996±.003	.994±.006	.950±.017	.946±.024	.921±.035

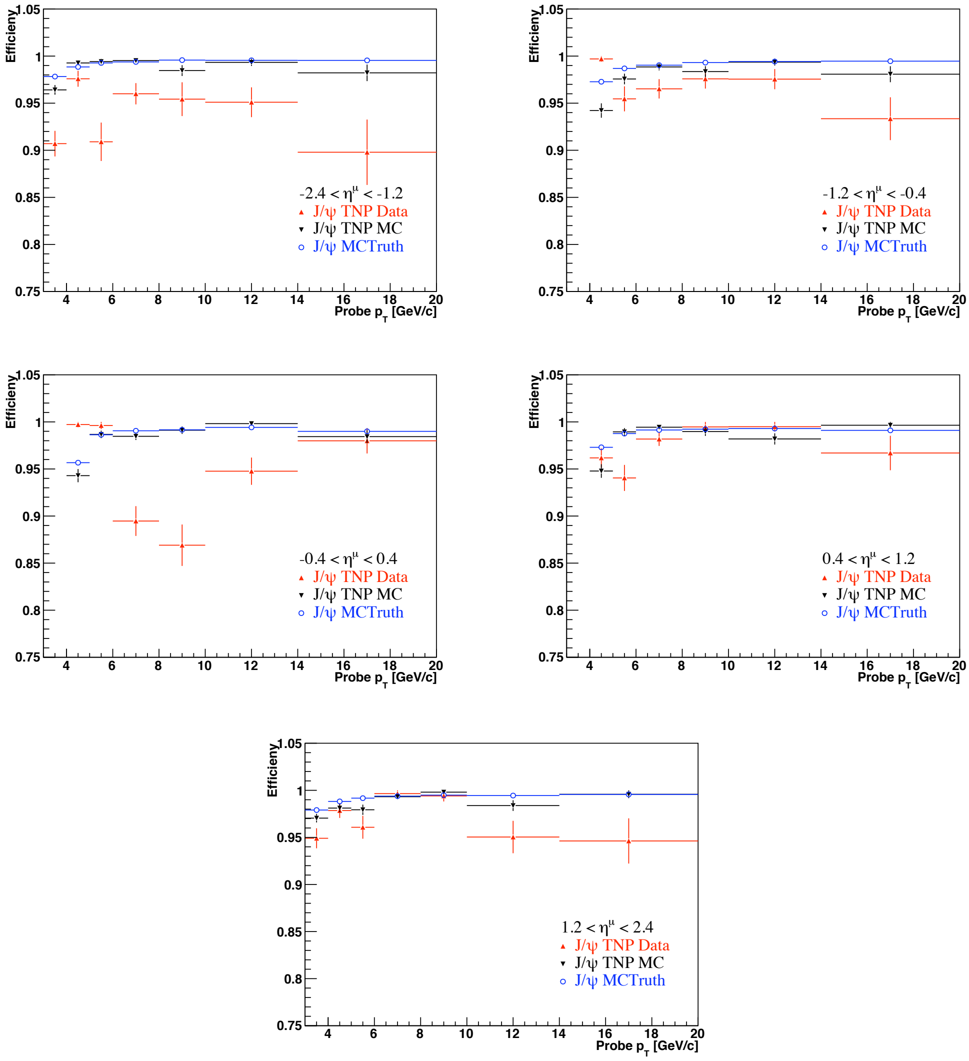

Figure 6.14: Single-muon identification efficiencies as a function of p_T^μ and η^μ from the TNP method using J/ψ events from data (red), MC (black), and the MC Truth (blue). The errors show the statistical uncertainties.

Comparing the TNP MC points with the MC "Truth" points in Figure 6.14 gives a feeling for how well the TNP method works. The MC "Truth" indicates the muon identification efciencies determined using reconstructed tracks which were matched to MC generator level muons. For single-muon identification the TNP MC points and the MC "Truth" points are in good agreement. The comparison of the TNP and MC-simulation di-muon efficiencies are described in Sec. 6.5.6, along with the calculation of the ρ factors that are used for the muon identification and trigger efficiency corrections.

In Figures 6.14, 6.15, and 6.16 display the different muons efficiencies up to $p_T = 20$ GeV/c. The last p_T bin is not plotted in order to focus on the best determined values. The efficiency values for the last p_T bin can be found in Tables 6.5 and 6.6.

6.5.4 Trigger Efficiency

The probes from the TNP method that satisfy the muon identification criteria are, in turn, the input probes for the study of the trigger efficiency. Both the tag and probe muons need to be matched to a leg of the double-muon trigger in order to consider the probe as a one that satisfies the trigger criterion. The resulting single-muon trigger efficiencies for one-leg (probe) of the HLT_DoubleMu0_Quarkonium_v1 trigger as function of p_T^μ for five η^μ regions are shown in Table 6.6 and Figure 6.15. No values are provided for the range $3 < p_T < 4$ GeV/c and $|\eta| < 1.2$ due to the phase space cut in Eq. 6.2. The comparisons between the HLT_DoubleMu0 and HLT_DoubleMu0_Quarkonium_v1 trigger efficiencies are shown in Figure 6.16, they are in agreement.

As mentioned in the last section, the fit to the TNP efficiency points, and the di-muon efficiency comparisons are described in Section 6.5.5 and 6.5.6, respectively.

There is a common feature in Figures 6.15 and 6.16. In the forward pseudorapidity region ($1.2 < |\eta| < 2.4$), at increasing p_T the TNP efficiency decreases for the MC and both data triggers. This is related to the distance between the two muons in the muon detector. The close distance between the muon hits causes the trigger inefficiency. This means that vetoing the type-1 di-muons does not solve the problem entirely. This is another motivation for fitting the TNP efficiency points and using the results of the fits for the di-muon efficiency calculations.

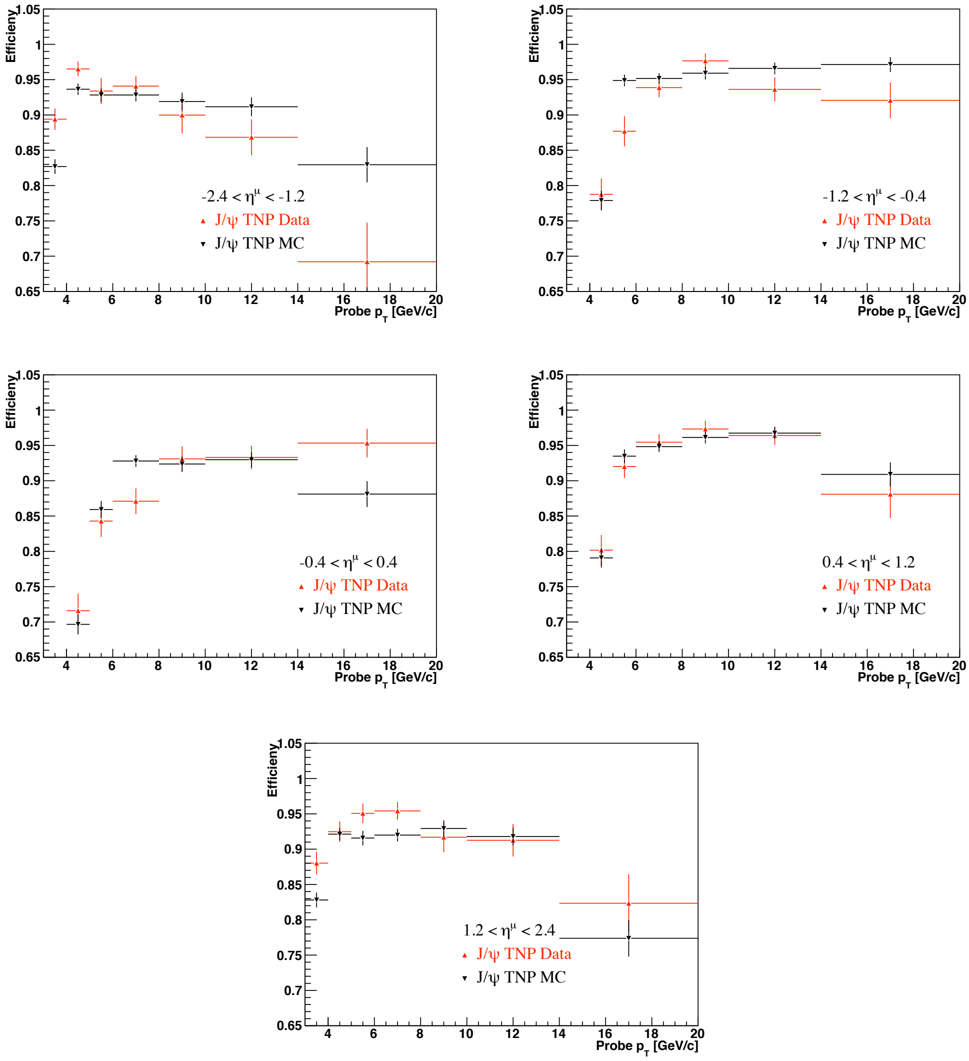

Figure 6.15: Single-muon trigger efficiencies as a function of p_T^{μ} and η^{μ} with the TNP method using J/ψ resonances from data (red) and MC (black). The errors show the statistical uncertainties.

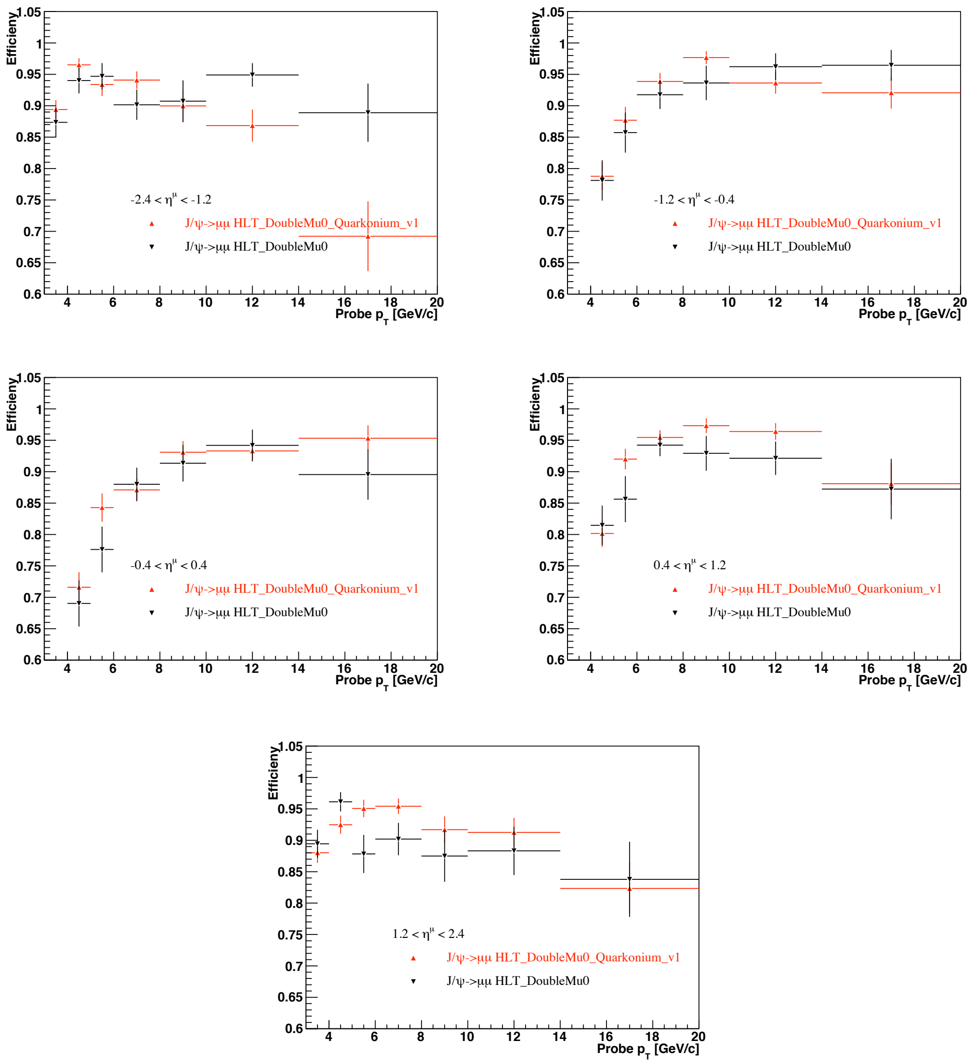

Figure 6.16: Single-muon trigger efficiencies as a function of p_T^μ and η^μ with the TNP method using J/ψ resonances from data for the HLT_DoubleMu0_Quarkonium_v1 (red) and HLT_DoubleMu0 (blue) triggers. The errors show the statistical uncertainties.

Table 6.6: Single-muon trigger efficiencies from the J/ψ TNP method; the uncertainties are statistical only.

η	p_T (GeV/c)							
	3 - 4	4 - 5	5 - 6	6 - 8	8 - 10	10 - 14	14 - 20	20 - 50
-2.4 – -1.2	.894±.015	.965±.010	.934±.018	.940±.014	.900±.026	.868±.026	.692±.055	.853±.060
-1.2 – -0.4	-	.788±.022	.877±.021	.939±.014	.977±.010	.936±.017	.921±.025	.809±.045
-0.4 – 0.4	-	.716±.024	.843±.022	.871±.018	.931±.018	.933±.017	.953±.020	.761±.042
0.4 – 1.2	-	.802±.022	.920±.016	.955±.011	.973±.012	.964±.013	.881±.034	.852±.039
1.2 – 2.4	.880±.016	.925±.014	.951±.014	.954±.012	.917±.021	.913±.023	.823±.041	.674±.068

6.5.5 Fits to the TNP Efficiency Points

As described in the previous sections, a fit is performed to obtain a better estimation of the muon identification and trigger efficiencies. A hyperbolic tangent function is used;

$$\begin{aligned} f(x;a,b,c,d) &= a + b \cdot \tanh(c \cdot (x-d)), \\ &= a + b \cdot \frac{\exp(2c \cdot (x-d)) - 1}{\exp(2c \cdot (x-d)) + 1}. \end{aligned} \tag{6.7}$$

The fit function increases rapidly with increasing p_T and reaches a plateau around 5-6 GeV/c for most fits. The most significant parameter is b that multiplies the tanh. Figures 6.17 and 6.18 show the fits with the fitted value for the parameter b and the uncertainty on it for the muon identification and trigger efficiencies, respectively. The uncertainty on the parameter b is used to estimate the systematical uncertainty on the di-muon efficiencies for the muon identification and trigger. The details are discussed in Section 7.1.

6.5.6 Efficiency Determination with MC Simulation

MC simulated event samples can directly provide a measurement of the di-muon efficiencies for muon identification and trigger. In the MC simulation, the muon identification and trigger efficiencies amounts to simply counting the number of events produced and the number passing a certain criteria. Comparing MC simulated di-muon efficiencies with the MC TNP di-muon efficiencies gives corrections that are applied to Data TNP di-muon efficiencies.

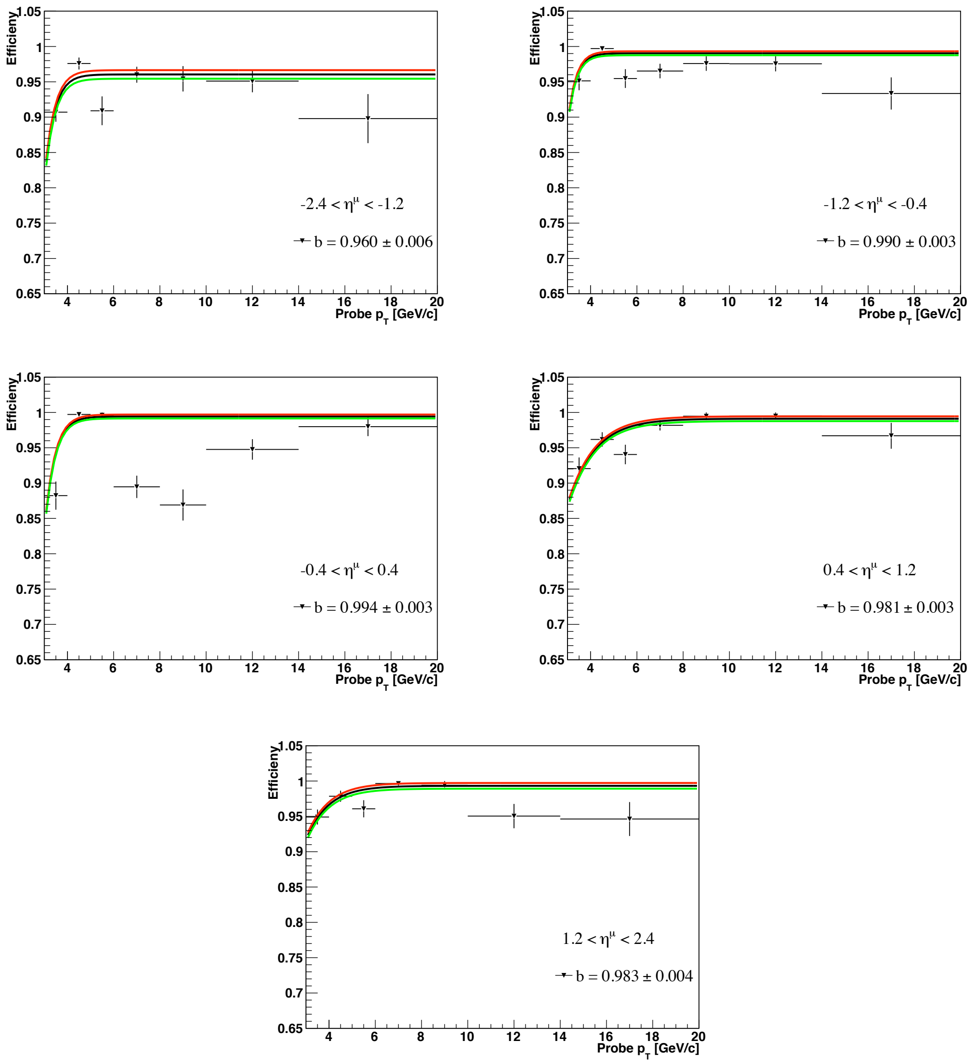

Figure 6.17: The single-muon identification efficiencies for five different ranges of η^μ and the result of the fit. The value and the uncertainty of the parameter b are also shown.

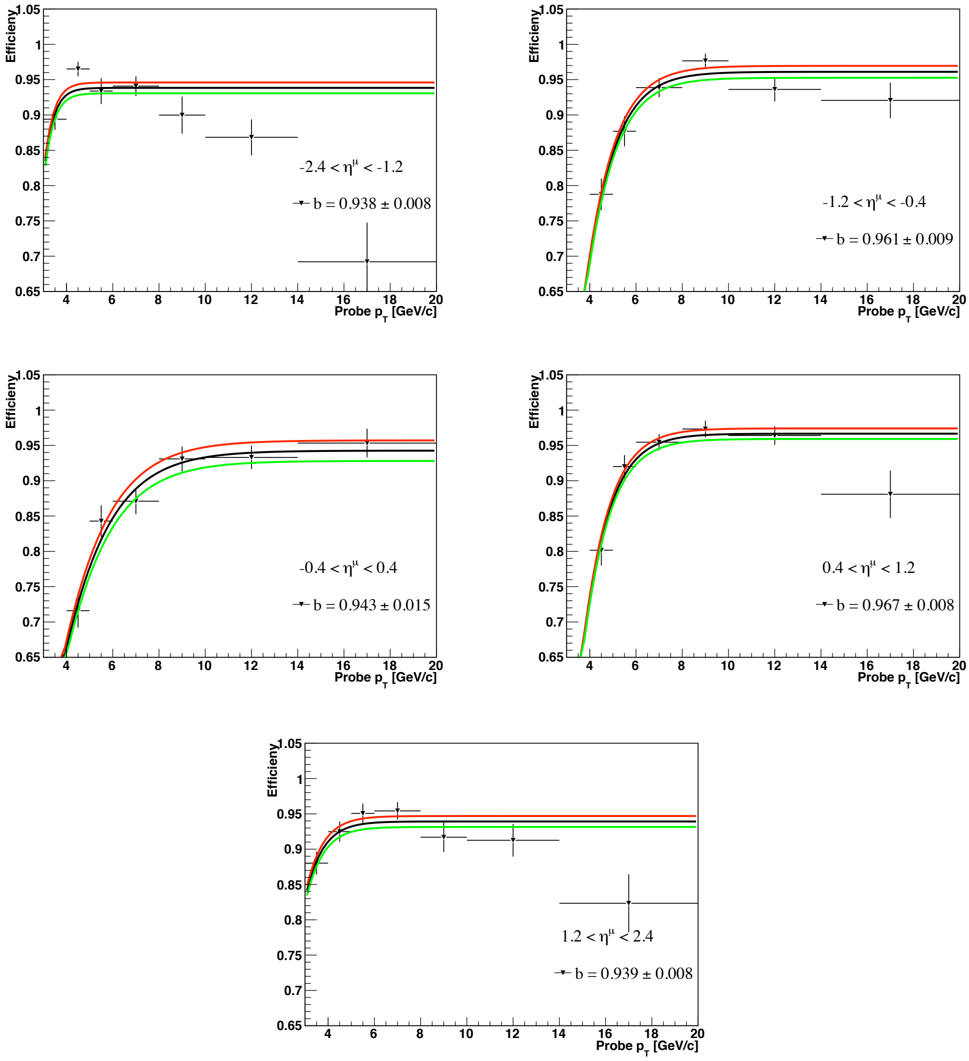

Figure 6.18: The single-muon trigger efficiencies for five different ranges of η^{μ} for the HLT_DoubleMu0_Quarkonium_v1 trigger and the result of the fit. The value and the uncertainty of the parameter b are also shown.

6.5.6.1 Comparison of TNP with MC Simulated Efficiencies

To compare the TNP di-muon efficiencies to the MC simulation efficiencies, the single-muon efficiencies have to be combined using the formula:

$$\langle \epsilon_{mc}^{TNP} \rangle = [\epsilon^{TNP}(p_T^{\mu_1}, \eta^{\mu_1}) \times \epsilon^{TNP}(p_T^{\mu_2}, \eta^{\mu_2}); w], \tag{6.8}$$

where w is the weight given by: $w = 1/[\epsilon^{TNP}(p_T^{\mu_1}, \eta^{\mu_1}) \times \epsilon^{TNP}(p_T^{\mu_2}, \eta^{\mu_2})]$. The di-muon TNP efficiencies are calculated by multiplying the single-muon TNP efficiencies and the result of the multiplication is taken into account with a weight that is the inverse of the multiplication.

The ratio ρ^{TNP} represents a correction to the above combination and, more importantly, for any possible bias introduced by the TNP efficiency measurement. It is described as

$$\rho^{TNP} = \frac{\epsilon(\text{di-muon}; \text{MC simulated})}{\langle \epsilon_{mc}^{TNP} \rangle}. \tag{6.9}$$

The di-muon efficiencies from the TNP, the MC simulation, and corresponding ρ^{TNP} values are shown in Figures 6.19 and 6.20 for muon identification and trigger efficiencies, respectively. The ρ^{TNP} factors for muon identification show almost no deviation from 1, whereas for the trigger they show some deviation in the forward-rapidity region.

6.5.7 Efficiency of Additional Selections

The efficiencies for a di-muon candidate to satisfy the vertex χ^2 probability and analysis requirements

- 8.7 GeV/c^2 < M_Υ < 11.2 GeV/c^2,
- $q_{\mu_1} \times q_{\mu_2} < 0$

are determined using the MC simulation. A sample of simulated Υ di-muons is identified by requiring that each muon satisfies the selection criteria in Section 6.2 and is matched to a generator-level muon. The number of reconstructed upsilons are counted as a function of the Υ p_T and y with and without the vertex probability criterion, and before and after the analysis criteria are imposed. The efficiencies for the vertex χ^2 probability and analysis requirements are shown in Figures 6.21 and 6.22, respectively. The efficiencies for the vertex χ^2 probability are all > 98%, and the efficiencies for the analysis criteria are all > 96%.

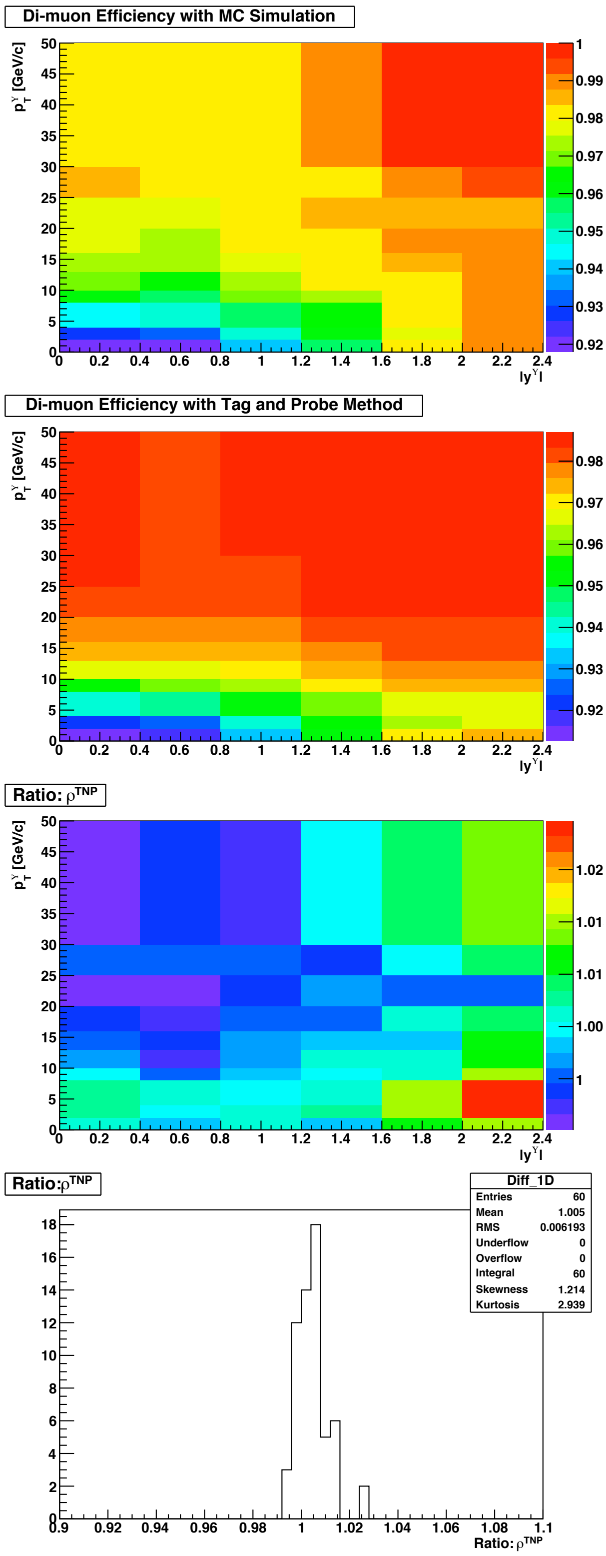

Figure 6.19: The di-muon identification efficiencies found from MC simulation (top), with the TNP method (middle) as a function of p_T^{Υ} and $|y^{\Upsilon}|$, and the ratios ρ^{TNP} (bottom).

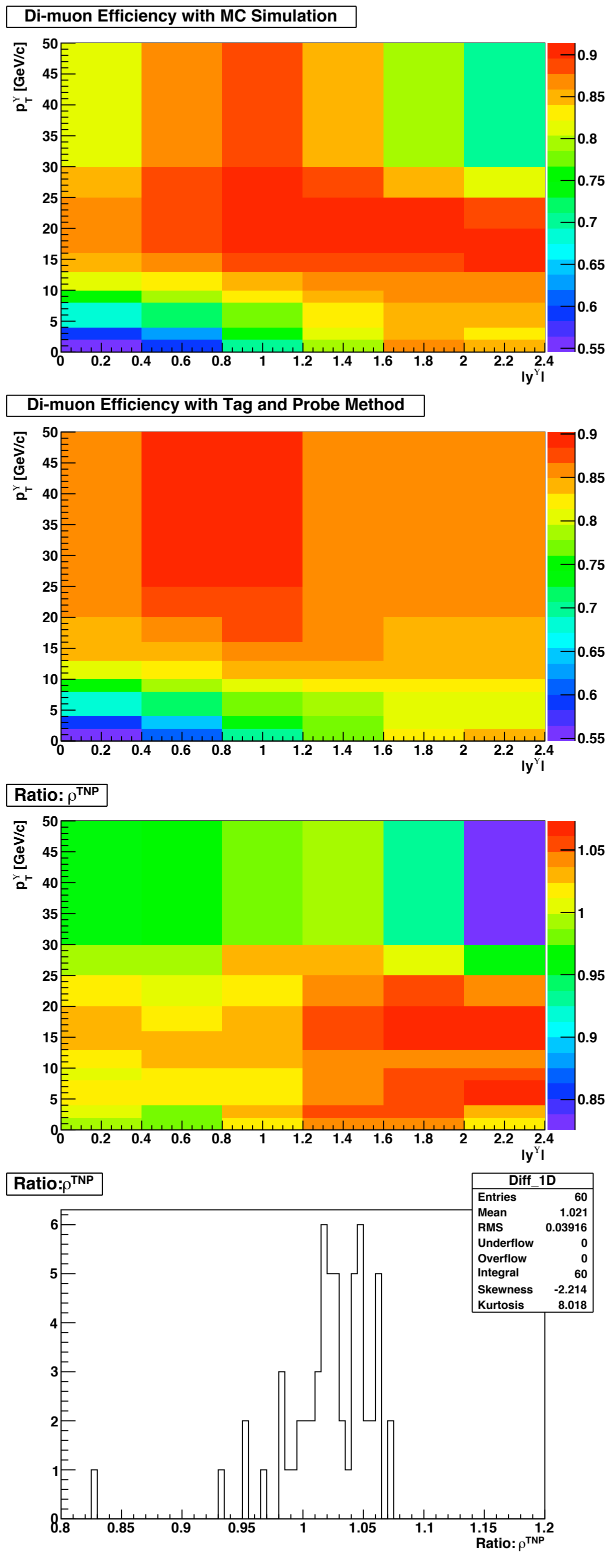

Figure 6.20: The di-muon trigger efficiencies found from MC simulation (top), with TNP method (middle) as a function of p_T^{Υ} and $|y^{\Upsilon}|$, and the ratios ρ^{TNP} (bottom).

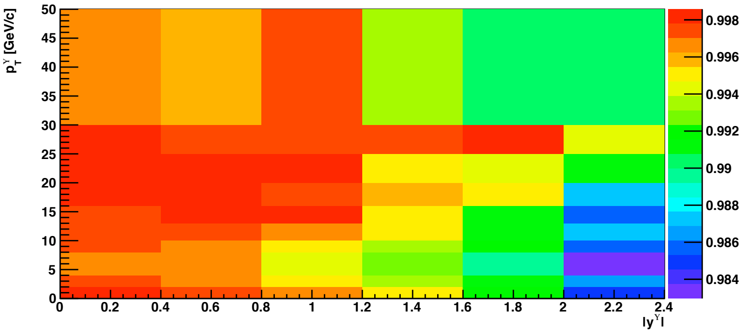

Figure 6.21: The vertex χ^2 probability efficiency found from MC simulations as a function of $|y^\Upsilon|$ and p_T^Υ.

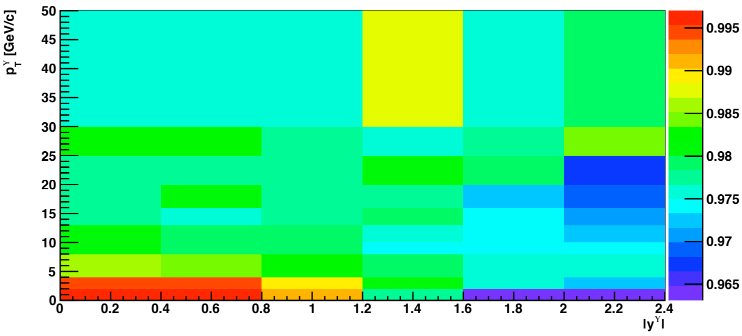

Figure 6.22: The efficiency of the analysis requirements found from MC simulations as a function of $|y^\Upsilon|$ and p_T^Υ.

Chapter 7

Systematic Uncertainties

There are several sources of systematic uncertainty that contribute to the measurement of the $\Upsilon(nS)$ cross section. This chapter focuses on the sources of the systematic uncertainty and the methods used in their determination.

The unknown $\Upsilon(nS)$ production polarization affects the distribution of the decay muons in the detector. The systematic uncertainty from the unknown polarization is the dominant uncertainty on the acceptance. Only unpolarized Υ cross section results are reported in this thesis, and the uncertainty is treated by quoting the cross section result using acceptance maps for five different polarization scenarios that are expected to represent a set of maximal variations. In the future, it should be possible to measure the Υ production polarization and cross section simultaneously with the larger data samples that are expected.

7.1 Muon Efficiencies

As mentioned in the previous chapter, the systematic uncertainties in the di-muon identification and trigger efficiencies are estimated by varying the fit parameter b by ± 1 standard deviation obtained from the fit to the muon efficiencies. For the TNP efficiency points that are more than -1 standard deviation away, half the difference between the -1 standard deviation and the measured value of the efficiency point is taken as the systematic uncertainty. The resulting uncertainties in the cross section measurement are 1-2% for all three resonances. Similarly, the systematic uncertainty on the cross section from the trigger and muon identification efficiencies are $\pm$ 2% and

$\pm$ 1% for low p_T ($p_T < 16$ GeV/c). However, with increasing p_T the positive side of the uncertainty increases up to 12% and 6%, respectively.

Another source of systematic uncertainty from the efficiencies arises from the uncertainty on the ρ factors. In the ρ-factor estimation, the MC simulation efficiencies are calculated using the Υ resonance for which the ρ factors are used as corrections, determine the ρ factors of the $\Upsilon(1S)$, the MC simulation efficiencies are calculated using simulated $\Upsilon(1S)$ events, and the same for $\Upsilon(2S)$ and $\Upsilon(3S)$. The uncertainty on the cross section from the ρ factors is estimated by taking the difference between the cross sections that are measured using the other two Υ resonances for the ρ factor calculations. The uncertainty on the $\Upsilon(1S)$ cross section from the ρ factor determination is estimated as 1% for $p_T^{\Upsilon(1S)} < 20$ GeV/c and 3% for $p_T^{\Upsilon(1S)} > 20$ GeV/c. For the $\Upsilon(2S)$ it is 1% for $p_T^{\Upsilon(2S)} < 20$ GeV/c and 2-3% for $p_T^{\Upsilon(2S)} > 20$ GeV/c. For the $\Upsilon(3S)$ it is 1-2% for $p_T^{\Upsilon(3S)} < 25$ GeV/c and 3-4% for $p_T^{\Upsilon(3S)} > 25$ GeV/c.

The muon charge misassignment rate is less than 0.01% [85] and contributes a negligible systematic uncertainty.

7.2 Di-muon Invariant Mass Fit

There can be systematic effects due to the function shapes used to parametrize the di-muon invariant mass signal and background distributions. This is especially true for the two FSR tail parameters (α and n) of the Crystal Ball (CB) function, which are fixed to the values extracted from the MC. These two parameters are also highly correlated. The systematic uncertainties from the CB functions are estimated by fitting the di-muon mass distributions to three Gaussians and a linear background instead of the three CBs and a linear background, and taking the difference of the signal yields. The uncertainty on the $\Upsilon(1S)$ cross section from the signal function shape is 3-4% for $p_T^{\Upsilon(1S)} < 25$ GeV/c and 10% for $p_T^{\Upsilon(1S)} > 25$ GeV/c. For the $\Upsilon(2S)$ it is 2-5% for $p_T^{\Upsilon(1S)} < 25$ GeV/c and 9-10% for $p_T^{\Upsilon(1S)} > 25$ GeV/c. For the $\Upsilon(3S)$ it is 3-14% for $p_T^{\Upsilon(3S)} < 25$ GeV/c and about 25% for $p_T^{\Upsilon(3S)} > 25$ GeV/c. In the summary tables at the end of this section, the uncertainties from the signal shape are labelled as *sigPDF*.

In order to estimate the systematical uncertainty from the background function shape, a second-order polynomial function is used instead of a first order. The di-muon mass distributions are fit to three CB functions and a second-order polynomial, and the differences in the signal yields are taken as the systematic uncertainty from the background function shape. The uncertainty on the $\Upsilon(1S)$ cross section from the background function shape is less than 1% for $p_T^{\Upsilon(1S)} < 16$ GeV/c and about 6% for $p_T^{\Upsilon(1S)} > 16$ GeV/c. For the $\Upsilon(2S)$ and $\Upsilon(3S)$ it is less 1%, except for three p_T bins where it is about 5%. In the tables, the uncertainties from the background shape are labelled as $bgPDF$.

The effect of the invariant mass range used in fits is studied by changing the range from 8.7 – 11.2 GeV/c^2 to 8 – 12 GeV/c^2 and performing the same fitting procedure. No significant difference is observed in the signal yields

7.3 Momentum Correction

The systematic uncertainty associated with the momentum correction is estimated by comparing the yields with and without the correction. The uncertainty on the cross section for $\Upsilon(1S)$, $\Upsilon(2S)$, and $\Upsilon(3S)$ are found to be less than 1%. In the tables, the uncertainties from the momentum correction are labelled as msc.

7.4 Bin Migration

The systematic uncertainty associated with reconstructing an Υ in a different p_T or y bin than in which it is produced is estimated by comparing the reconstructed and generated Υ yields in a given bin from the MC simulation. The bins were chosen to keep the bin migration below 1% and the uncertainty on the cross section for $\Upsilon(1S)$, $\Upsilon(2S)$, and $\Upsilon(3S)$ are found to be less than 1% for most of the bins. In the tables, the uncertainties from the bin migration are labelled as mig.

7.5 Luminosity

The systematic uncertainty associated with the integrated luminosity measurement is estimated to be 4% [86].

7.6 Summary of Uncertainties

The sources of systematic uncertainty on the Υ differential cross section measurements along with the uncertainty from the luminosity and the unknown production polarization is summarized in Tables 7.1, 7.2, and 7.3 for $\Upsilon(1S)$, $\Upsilon(2S)$, and $\Upsilon(3S)$, respectively.

For the systematic uncertainties on the ratios of the production cross sections the contributions from the integrated luminosity, muon identification and trigger efficiencies cancel out, and only the uncertainties from the polarization, signal and background shapes, ρ factor, momentum correction, and bin migration play a role. The sources of systematic uncertainty on the $\sigma(\Upsilon(2S))/\sigma(\Upsilon(1S))$ and $\sigma(\Upsilon(3S))/\sigma(\Upsilon(1S))$ ratios and their magnitudes are summarized in Tables 7.4, and 7.5.

Table 7.1: Summary of the various contributions to the systematic uncertainty on the $\Upsilon(1S)$ differential cross section for three p_T intervals. The uncertainties from the signal shape, background shape, momentum correction, and bin migration are labelled as *sigPDF*, *bgPDF*, *msc*, and *mig*, respectively. Totals are given with and without including the polarization uncertainty

	uncertainty [%]		
	$p_T < 10$ GeV/c	$10 < p_T < 25$ GeV/c	$p_T > 25$ GeV/c
Polarization	18.2 - 26.9	12.0 - 22.0	9.2 - 16.1
Luminosity	4.0	4.0	4.0
Trig Eff	2.0 - 2.2	2.3 - 7.0	9.6 - 12.6
MuID Eff	0.9 - 1.7	2.3 - 3.4	4.8 - 6.1
ρ factor	0.0 - 1.4	0.0 - 1.8	3.0 - 3.5
sigPDF	3.0 - 3.8	1.6 - 4.0	9.7 - 10.3
bgPDF	0.1 - 0.3	0.1 - 6.2	9.8
msc	0.1 - 0.8	0.1 - 0.6	0.1 - 0.5
mig	0.1 - 0.4	0.1 - 0.7	0.5 - 1.5
total without polarization	5.5 - 6.4	5.4 - 11.6	18.2 - 20.7
total with polarization	19.0 - 27.7	13.2 - 24.9	20.4 - 26.2

Table 7.2: Summary of the various contributions to the systematic uncertainty on the $\Upsilon(2S)$ differential cross section.

	uncertainty [%]		
	$p_T < 10$ GeV/c	$10 < p_T < 25$ GeV/c	$p_T > 25$ GeV/c
Polarization	17.2 - 25.3	12.1 - 21.3	8.9 - 14.9
Luminosity	4.0	4.0	4.0
Trig Eff	2.0 - 2.2	2.3 - 6.7	9.9 - 12.5
MuID Eff	0.8 - 1.7	2.4 - 3.4	5.0 - 6.0
ρ factor	0.1 - 1.7	0.0 - 1.9	1.5 - 3.0
sigPDF	1.5 - 5.0	2.1 - 5.4	8.6 - 10.9
bgPDF	0.4 - 7.1	0.6 - 4.8	4.3
msc	0.2 - 0.3	0.2 - 0.5	0.2 - 1.1
mig	0.3 - 0.5	0.3 - 1.1	0.4 - 0.5
total without polarization	4.8 - 10.1	5.7 - 11.4	15.3 - 18.9
total with polarization	17.9 - 27.2	13.3 - 24.2	17.7 - 24.0

Table 7.3: Summary of the various contributions to the systematic uncertainty on the $\Upsilon(3S)$ differential cross section.

	uncertainty [%]		
	$p_T < 10$ GeV/c	$10 < p_T < 25$ GeV/c	$p_T > 25$ GeV/c
Polarization	16.3 - 24.2	11.5 - 20.5	8.4 - 14.0
Luminosity	4.0	4.0	4.0
Trig Eff	2.0 - 2.1	2.4 - 6.8	10.1 - 12.8
MuID Eff	0.8 - 1.6	2.2 - 3.4	5.2 - 6.4
ρ factor	0.2 - 2.0	0.1 - 1.9	3.7 - 4.6
sigPDF	6.9 - 13.8	3.0 - 9.9	27.0 - 46.6
bgPDF	0.4 - 4.2	0.1 - 8.3	5.5
msc	0.1 - 0.8	0.2 - 0.9	0.3 - 0.5
mig	0.1 - 0.3	0.1 - 0.3	0.1 - 0.4
total without polarization	8.3 - 15.4	6.0 - 15.7	30.3 - 49.4
total with polarization	18.3 - 28.7	13.0 - 25.8	31.4 - 51.4

Table 7.4: Summary of the various contributions to the systematic uncertainty on $\sigma(\Upsilon(2S))/\sigma(\Upsilon(1S))$ ratio.

	uncertainty [%]		
	$p_T < 10$ GeV/c	$10 < p_T < 25$ GeV/c	$p_T > 25$ GeV/c
Polarization	23.2 - 43.3	21.3 - 33.8	12.7 - 23.3
ρ factor	0.1 - 2.1	0.1 - 2.7	1.5 - 4.4
sigPDF	3.8 - 6.2	4.1 - 5.6	13.4 - 14.6
bgPDF	0.1 - 3.7	0.1 - 7.9	10.7
msc	0.1 - 0.8	0.1 - 0.6	0.2 - 1.2
mig	0.1 - 0.6	0.6 - 1.2	0.6 - 1.6
total without polarization	3.8 - 7.6	4.2 - 10.1	17.2 - 18.7
total with polarization	23.5 - 44.0	21.7 - 35.3	21.4 - 29.9

Table 7.5: Summary of the various contributions to the systematic uncertainty on $\sigma(\Upsilon(3S))/\sigma(\Upsilon(1S))$ ratio.

	uncertainty [%]		
	$p_T < 10$ GeV/c	$10 < p_T < 25$ GeV/c	$p_T > 25$ GeV/c
Polarization	24.5 - 37.3	20.7 - 35.5	12.3 - 22.4
ρ factor	0.1 - 1.8	0.2 - 1.9	3.0 - 4.5
sigPDF	6.6 - 14.2	4.9 - 10.5	28.7 - 47.8
bgPDF	0.1 - 4.2	0.1 - 10.4	11.3
msc	0.1 - 1.1	0.1 - 0.9	0.2 - 0.7
mig	0.1 - 0.5	0.2 - 0.7	0.6 - 1.5
total without polarization	6.6 - 15.0	4.9 - 14.9	31.0 - 49.4
total with polarization	25.4 - 40.2	21.3 - 38.5	33.3 - 54.2

Chapter 8

Results

Integrated over the range $p_T \leq 50$ GeV/c and $|y| \leq 2.4$, the product of the $\Upsilon(nS)$ production cross section and the di-muon branching fraction ($B_{\mu\mu}$), assuming the unpolarized Υ scenario, with the statistical and systematic uncertainties is measured to be:

$$\sigma(pp \to \Upsilon(1S)X) \cdot \mathcal{B}(\Upsilon(1S) \to \mu^+\mu^-) = 8.347 \pm 0.056 \text{ (stat.) } {}^{+0.365}_{-0.350} \text{ (syst.)} \pm 0.334 \text{ (lumi.) nb}\,,$$
$$\sigma(pp \to \Upsilon(2S)X) \cdot \mathcal{B}(\Upsilon(2S) \to \mu^+\mu^-) = 2.274 \pm 0.034 \text{ (stat.) } {}^{+0.138}_{-0.130} \text{ (syst.)} \pm 0.086 \text{ (lumi.) nb}\,,$$
$$\sigma(pp \to \Upsilon(3S)X) \cdot \mathcal{B}(\Upsilon(3S) \to \mu^+\mu^-) = 1.175 \pm 0.021 \text{ (stat.) } {}^{+0.101}_{-0.098} \text{ (syst.)} \pm 0.046 \text{ (lumi.) nb}\,.$$

The uncertainties shown in the figures and quoted in the tables include both the statistical and systematic ones. However, the 4% systematic uncertainty on the integrated luminosity is not included. Only Figures 8.5 and 8.7, and Tables 8.11 and 8.13 take into account the effect of the unknown production polarization.

The $\Upsilon(nS)$ differential p_T cross-section results for the rapidity region $|y^{\Upsilon}| < 2.4$ are shown in Figure 8.1. Figure 8.2 shows the differential p_T cross-section results fitted to the function; $a \times \exp(-bp_T + cp_T^2)$. Table 8.1 shows the fir parameters for the differential cross sections of the $\Upsilon(nS)$ as a function of p_T integrated over the rapidity range $|y| < 2.4$. The $\Upsilon(nS)$ p_T-integrated, differential rapidity cross-section measurements are shown in Figure 8.3. A decrease in the cross section at larger rapidity is observed, consistent with theoretical expectations [87].

The relative systematic uncertainties from each source on the differential p_T cross section are summarized in Tables 8.2, 8.3, and 8.4. The relative systematical uncertainties from each source on the differential $|y|$ cross section are summarized in Table 8.8.

Tables 8.5, 8.6, 8.7, and 8.9 show the relative systematical uncertainties for the different polarization scenarios. In all the tables, the mean of the bins (p_T or $|y|$) are given in the second column. They are the mean values of the Υ distributions in each bin, and are the positions where the corresponding points are plotted in the figures.

Due to the feed-down processes $\Upsilon(3S) \to \Upsilon(2S)X$, $\Upsilon(3S) \to \Upsilon(1S)X$, and $\Upsilon(2S) \to \Upsilon(1S)X$, and the assumption that the p_T dependence of the direct differential production cross section for each upsilon resonance is the same, it is expected that the ratios of the production cross sections $\sigma(\Upsilon(3S))/\sigma(\Upsilon(1S))$ and $\sigma(\Upsilon(2S))/\sigma(\Upsilon(1S))$ will increase with p_T. The data support this argument. The ratios of the $\Upsilon(nS)$ differential p_T cross sections for the unpolarized scenario are shown in Figure 8.4 and summarized in Table 8.10. The ratios of the $\Upsilon(nS)$ differential p_T cross sections with the addition of maximum variation in the polarization as a systematical uncertainty are shown in Figure 8.5 and summarized in Table 8.11. Similarly, the ratios of the $\Upsilon(nS)$ differential $|y|$ cross sections for the unpolarized scenario and with maximum variation in the polarization are shown in Figures 8.6 and 8.7, and summarized in Tables 8.12 and 8.13, respectively. The measurements of the ratios of the production cross sections are consistent with being independent of $|y^{\Upsilon}|$, within their uncertainties. The ratios $(\sigma(\Upsilon(2S)) \times B_{\mu\mu})/(\sigma(\Upsilon(1S)) \times B_{\mu\mu})$ and $(\sigma(\Upsilon(3S)) \times B_{\mu\mu})/(\sigma(\Upsilon(1S)) \times B_{\mu\mu})$ averaged over all p_T are 0.268 and 0.135, respectively.

The systematical uncertainty for the maximum variation in the polarization has been estimated by taking the difference between the cross sections with no Υ polarization and with fully transverse and longitudinal polarization in the helicity frame.

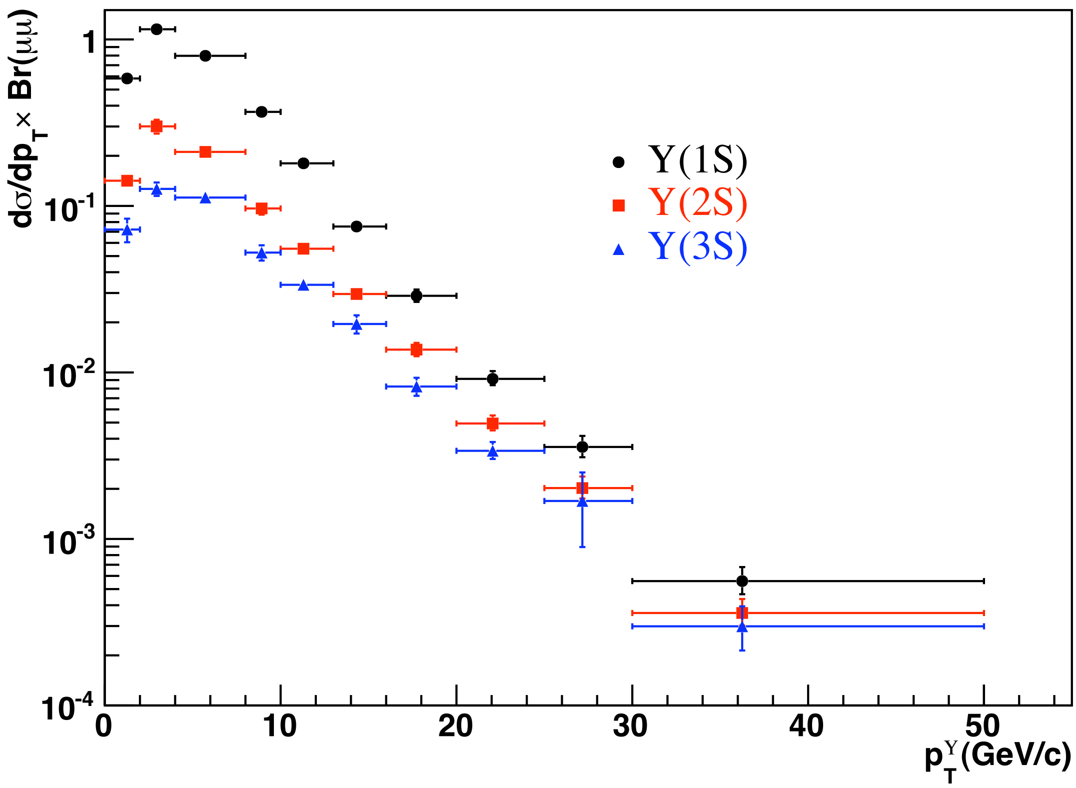

Figure 8.1: Differential cross sections of the $\Upsilon(nS)$ as a function of p_T integrated over the rapidity range $|y| < 2.4$. The uncertainties include both statistical and systematic.

Table 8.1: Fit parameters for the differential cross sections of the $\Upsilon(nS)$ as a function of p_T integrated over the rapidity range $|y| < 2.4$.

Fit Function; $a \times \exp(-bx + cx^2)$			
	a	b	c
$\Upsilon(1S)$	4.7289 ± 0.4079	0.3123 ± 0.0126	0.0016 ± 0.0004
$\Upsilon(2S)$	0.8699 ± 0.0981	0.2544 ± 0.0146	0.0011 ± 0.0004
$\Upsilon(3S)$	0.4249 ± 0.0652	0.2373 ± 0.0215	0.0010 ± 0.0006

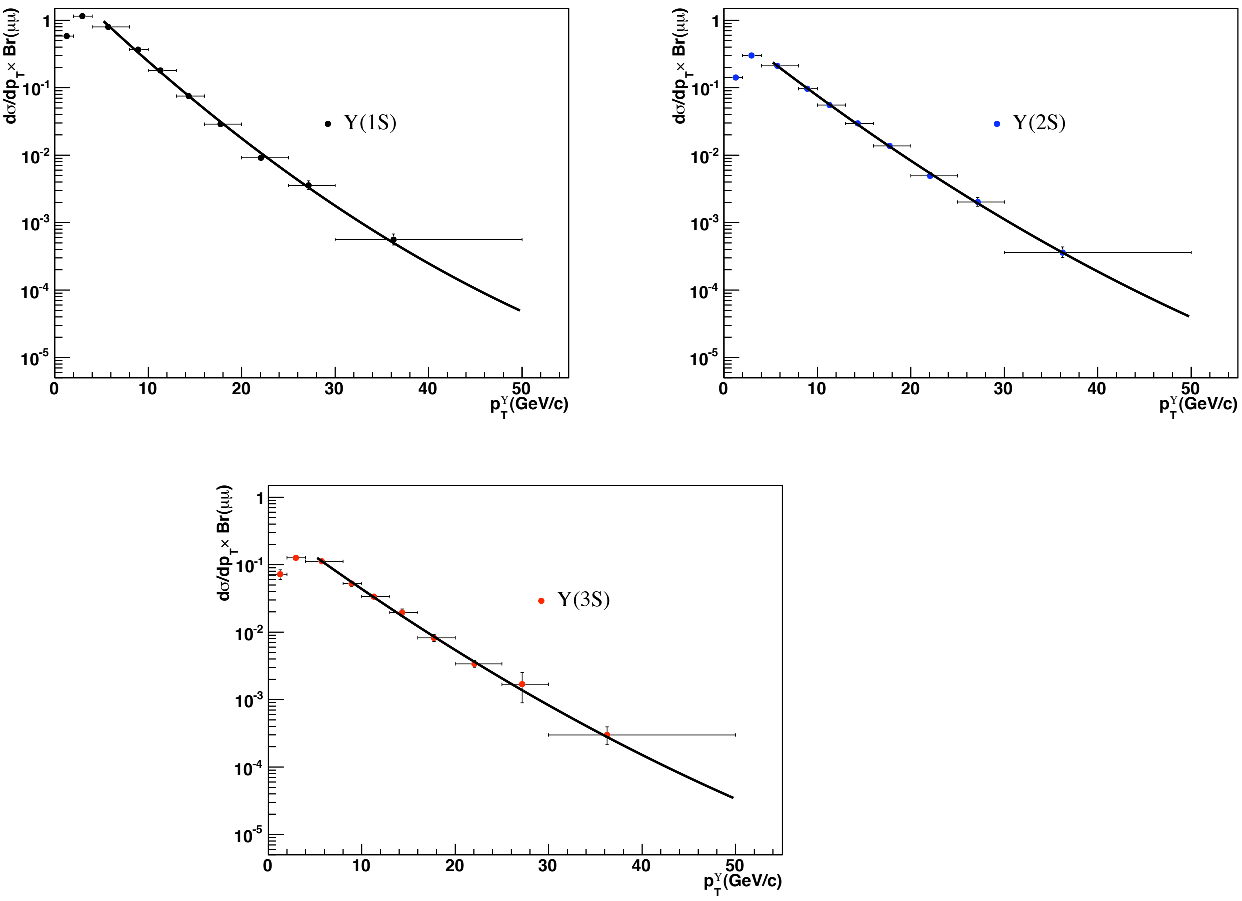

Figure 8.2: Fits to differential cross sections of the $\Upsilon(nS)$ as a function of p_T integrated over the rapidity range $|y| < 2.4$. Fit function; $a \times \exp(-bx + cx^2)$.

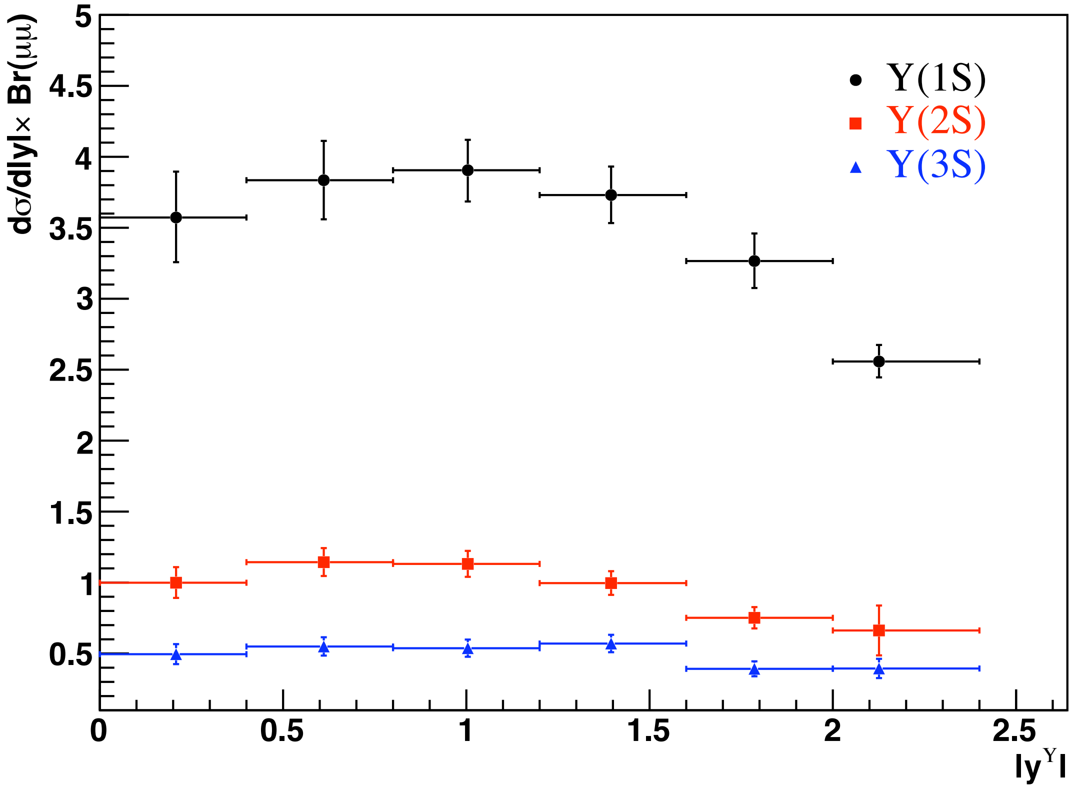

Figure 8.3: $\Upsilon(nS)$ p_T-integrated, rapidity differential cross sections. The uncertainties include both statistical and systematic.

Table 8.2: The $\Upsilon(1S)$ differential p_T cross sections and the relative statistical and systematic uncertainties from each source for the unpolarized scenario. The uncertainties from the signal shape, background shape, momentum correction, and bin migration are labelled as *sigPDF*, *bgPDF*, *msc*, and *mig*, respectively. The luminosity uncertainty of 4% is not shown in the table.

p_T(GeV/c)	p_T^{mean}(GeV/c)	σ(nb)	stat/σ	syst/σ	ϵ_{trig}/σ	ϵ_{muid}/σ	ρ/σ	sigPDF/σ	bgPDF/σ	msc/σ	mig/σ
0 - 2	1.27	1.166	0.017	$^{+0.043}_{-0.045}$	$^{+0.020}_{-0.019}$	$^{+0.009}_{-0.008}$	0.014	0.036	0.001	0.008	0.004
2 - 4	2.95	2.302	0.014	$^{+0.043}_{-0.043}$	$^{+0.019}_{-0.019}$	$^{+0.010}_{-0.008}$	0.004	0.037	0.002	0.000	0.003
4 - 8	5.72	3.188	0.012	$^{+0.038}_{-0.037}$	$^{+0.020}_{-0.019}$	$^{+0.013}_{-0.008}$	0.002	0.030	0.000	0.001	0.000
8 - 10	8.92	0.734	0.021	$^{+0.047}_{-0.045}$	$^{+0.022}_{-0.019}$	$^{+0.017}_{-0.008}$	0.012	0.038	0.003	0.000	0.000
10 - 13	11.30	0.541	0.020	$^{+0.052}_{-0.045}$	$^{+0.023}_{-0.019}$	$^{+0.023}_{-0.008}$	0.007	0.040	0.001	0.000	0.001
13 - 16	14.32	0.226	0.029	$^{+0.052}_{-0.042}$	$^{+0.028}_{-0.019}$	$^{+0.024}_{-0.008}$	0.002	0.036	0.000	0.001	0.007
16 - 20	17.73	0.115	0.034	$^{+0.085}_{-0.073}$	$^{+0.039}_{-0.018}$	$^{+0.026}_{-0.007}$	0.003	0.032	0.062	0.002	0.004
20 - 25	22.06	0.046	0.049	$^{+0.103}_{-0.068}$	$^{+0.074}_{-0.020}$	$^{+0.036}_{-0.009}$	0.019	0.016	0.058	0.006	0.006
25 - 30	27.16	0.018	0.071	$^{+0.149}_{-0.112}$	$^{+0.095}_{-0.019}$	$^{+0.048}_{-0.008}$	0.035	0.103	0.001	0.005	0.015
30 - 50	36.25	0.011	0.084	$^{+0.197}_{-0.143}$	$^{+0.126}_{-0.019}$	$^{+0.061}_{-0.008}$	0.030	0.097	0.098	0.000	0.005

Table 8.3: The $\Upsilon(2S)$ differential p_T cross sections and the relative statistical and systematic uncertainties from each source for the unpolarized scenario. The luminosity uncertainty of 4% is not shown in the table.

p_T(GeV/c)	p_T^{mean}(GeV/c)	σ(nb)	stat/σ	syst/σ	ϵ_{trig}/σ	ϵ_{muid}/σ	ρ/σ	sigPDF/σ	bgPDF/σ	msc/σ	mig/σ
0 - 2	1.27	0.283	0.046	$^{+0.031}_{-0.027}$	$^{+0.020}_{-0.019}$	$^{+0.008}_{-0.007}$	$^{+0.016}_{-0.003}$	0.015	0.004	0.002	0.005
2 - 4	2.95	0.601	0.033	$^{+0.090}_{-0.090}$	$^{+0.018}_{-0.017}$	$^{+0.009}_{-0.007}$	$^{+0.003}_{-0.003}$	0.051	0.071	0.003	0.003
4 - 8	5.72	0.844	0.029	$^{+0.049}_{-0.048}$	$^{+0.019}_{-0.018}$	$^{+0.012}_{-0.008}$	$^{+0.001}_{-0.003}$	0.044	0.000	0.002	0.000
8 - 10	8.92	0.193	0.049	$^{+0.069}_{-0.066}$	$^{+0.022}_{-0.019}$	$^{+0.017}_{-0.008}$	$^{+0.010}_{-0.002}$	0.050	0.038	0.000	0.004
10 - 13	11.30	0.166	0.044	$^{+0.041}_{-0.032}$	$^{+0.023}_{-0.019}$	$^{+0.024}_{-0.008}$	$^{+0.006}_{-0.001}$	0.022	0.006	0.005	0.006
13 - 16	14.32	0.089	0.060	$^{+0.044}_{-0.031}$	$^{+0.029}_{-0.019}$	$^{+0.024}_{-0.008}$	$^{+0.008}_{-0.006}$	0.021	0.001	0.000	0.003
16 - 20	17.73	0.055	0.061	$^{+0.076}_{-0.062}$	$^{+0.041}_{-0.018}$	$^{+0.026}_{-0.008}$	$^{+0.004}_{-0.002}$	0.032	0.048	0.004	0.011
20 - 25	22.06	0.025	0.069	$^{+0.095}_{-0.059}$	$^{+0.067}_{-0.019}$	$^{+0.034}_{-0.008}$	$^{+0.019}_{-0.000}$	0.054	0.001	0.002	0.011
25 - 30	27.16	0.010	0.099	$^{+0.142}_{-0.091}$	$^{+0.097}_{-0.019}$	$^{+0.049}_{-0.008}$	$^{+0.027}_{-0.015}$	0.086	0.001	0.011	0.005
30 - 50	36.25	0.007	0.107	$^{+0.184}_{-0.119}$	$^{+0.125}_{-0.019}$	$^{+0.060}_{-0.008}$	$^{+0.030}_{-0.001}$	0.109	0.043	0.002	0.004

Table 8.4: The $\Upsilon(3S)$ differential p_T cross sections and the relative statistical and systematic uncertainties from each source for the unpolarized scenario. The luminosity uncertainty of 4% is not shown in the table.

p_T(GeV/c)	p_T^{mean}(GeV/c)	σ(nb)	stat/σ	syst/σ	ϵ_{trig}/σ	ϵ_{muid}/σ	ρ/σ	sigPDF/σ	bgPDF/σ	msc/σ	mig/σ
0 - 2	1.27	0.144	0.079	$^{+0.141}_{-0.140}$	$^{+0.020}_{-0.019}$	$^{+0.008}_{-0.007}$	0.019	0.138	0.004	0.008	0.003
2 - 4	2.95	0.253	0.048	$^{+0.080}_{-0.079}$	$^{+0.019}_{-0.018}$	$^{+0.010}_{-0.008}$	0.006	0.075	0.016	0.003	0.001
4 - 8	5.72	0.449	0.032	$^{+0.064}_{-0.063}$	$^{+0.019}_{-0.018}$	$^{+0.012}_{-0.008}$	0.002	0.059	0.000	0.001	0.001
8 - 10	8.92	0.105	0.062	$^{+0.087}_{-0.084}$	$^{+0.021}_{-0.019}$	$^{+0.016}_{-0.008}$	0.011	0.069	0.042	0.005	0.001
10 - 13	11.30	0.101	0.047	$^{+0.046}_{-0.038}$	$^{+0.024}_{-0.019}$	$^{+0.022}_{-0.008}$	0.008	0.030	0.007	0.007	0.002
13 - 16	14.32	0.059	0.071	$^{+0.106}_{-0.101}$	$^{+0.029}_{-0.019}$	$^{+0.024}_{-0.008}$	0.003	0.099	0.001	0.000	0.003
16 - 20	17.73	0.033	0.058	$^{+0.114}_{-0.106}$	$^{+0.041}_{-0.018}$	$^{+0.025}_{-0.007}$	0.001	0.062	0.083	0.009	0.000
20 - 25	22.06	0.017	0.068	$^{+0.110}_{-0.080}$	$^{+0.068}_{-0.020}$	$^{+0.034}_{-0.008}$	0.019	0.077	0.002	0.002	0.001
25 - 30	27.16	0.008	0.044	$^{+0.482}_{-0.467}$	$^{+0.099}_{-0.018}$	$^{+0.051}_{-0.008}$	0.045	0.466	0.001	0.005	0.001
30 - 50	36.25	0.006	0.054	$^{+0.313}_{-0.277}$	$^{+0.128}_{-0.019}$	$^{+0.064}_{-0.008}$	0.037	0.270	0.055	0.003	0.004

Table 8.5: The $\Upsilon(1S)$ differential p_T cross sections and the relative statistical and systematic uncertainties from each source including different polarization scenarios (transversely polarized in the helicity frame (HX T), longitudinally polarized in the helicity frame (HX L), transversely polarized in the Collins-Soper frame (CS T), and longitudinally polarized in the Collins-Soper frame(CS L)). The luminosity uncertainty of 4% is not shown in the table.

p_T (GeV/c)	p_T^{mean} (GeV/c)	σ (nb)	stat/σ	syst/σ	HX T	HX L	CS T	CS L
0 - 2	1.27	1.166	0.017	$^{+0.043}_{-0.045}$	0.220	-0.263	0.230	-0.271
2 - 4	2.95	2.302	0.014	$^{+0.043}_{-0.043}$	0.225	-0.269	0.220	-0.263
4 - 8	5.72	3.188	0.012	$^{+0.038}_{-0.037}$	0.204	-0.252	0.156	-0.205
8 - 10	8.92	0.734	0.021	$^{+0.047}_{-0.045}$	0.182	-0.234	0.067	-0.085
10 - 13	11.30	0.541	0.020	$^{+0.052}_{-0.045}$	0.167	-0.220	0.018	-0.000
13 - 16	14.32	0.226	0.029	$^{+0.052}_{-0.042}$	0.154	-0.208	-0.006	0.046
16 - 20	17.73	0.115	0.034	$^{+0.085}_{-0.073}$	0.144	-0.199	-0.037	0.095
20 - 25	22.06	0.046	0.049	$^{+0.103}_{-0.068}$	0.120	-0.174	-0.029	0.079
25 - 30	27.16	0.018	0.071	$^{+0.149}_{-0.112}$	0.108	-0.161	-0.035	0.085
30 - 50	36.25	0.011	0.084	$^{+0.197}_{-0.143}$	0.092	-0.144	-0.038	0.087

Table 8.6: The $\Upsilon(2S)$ differential p_T cross sections and the relative statistical and systematic uncertainties from each source including different polarization scenarios (transversely polarized in the helicity frame (HX T), longitudinally polarized in the helicity frame (HX L), transversely polarized in the Collins-Soper frame (CS T), and longitudinally polarized in the Collins-Soper frame(CS L)). The luminosity uncertainty of 4% is not shown in the table.

p_T(GeV/c)	p_T^{mean}(GeV/c)	σ(nb)	stat/σ	syst/σ	HX T	HX L	CS T	CS L
0 - 2	1.27	0.283	0.046	$^{+0.031}_{-0.027}$	0.184	-0.236	0.200	-0.250
2 - 4	2.95	0.601	0.033	$^{+0.090}_{-0.090}$	0.204	-0.253	0.200	-0.249
4 - 8	5.72	0.844	0.029	$^{+0.049}_{-0.048}$	0.191	-0.242	0.156	-0.206
8 - 10	8.92	0.193	0.049	$^{+0.069}_{-0.066}$	0.172	-0.224	0.068	-0.089
10 - 13	11.30	0.166	0.044	$^{+0.041}_{-0.032}$	0.160	-0.213	0.027	-0.016
13 - 16	14.32	0.089	0.060	$^{+0.044}_{-0.031}$	0.143	-0.197	0.008	0.021
16 - 20	17.73	0.055	0.061	$^{+0.076}_{-0.062}$	0.137	-0.191	-0.029	0.079
20 - 25	22.06	0.025	0.069	$^{+0.095}_{-0.059}$	0.121	-0.174	-0.031	0.081
25 - 30	27.16	0.010	0.099	$^{+0.142}_{-0.091}$	0.099	-0.149	-0.022	0.061
30 - 50	36.25	0.007	0.107	$^{+0.184}_{-0.119}$	0.089	-0.140	-0.037	0.084

Table 8.7: The $\Upsilon(3S)$ differential p_T cross sections and the relative statistical and systematic uncertainties from each source including different polarization scenarios (transversely polarized in the helicity frame (HX T), longitudinally polarized in the helicity frame (HX L), transversely polarized in the Collins-Soper frame (CS T), and longitudinally polarized in the Collins-Soper frame(CS L)). The luminosity uncertainty of 4% is not shown in the table.

p_T(GeV/c)	p_T^{mean}(GeV/c)	σ(nb)	stat/σ	syst/σ	HX T	HX L	CS T	CS L
0 - 2	1.27	0.144	0.079	$^{+0.141}_{-0.140}$	0.176	−0.227	0.197	−0.246
2 - 4	2.95	0.253	0.048	$^{+0.080}_{-0.079}$	0.192	−0.242	0.198	−0.247
4 - 8	5.72	0.449	0.032	$^{+0.064}_{-0.063}$	0.180	−0.233	0.162	−0.211
8 - 10	8.92	0.105	0.062	$^{+0.087}_{-0.084}$	0.163	−0.217	0.080	−0.105
10 - 13	11.30	0.101	0.047	$^{+0.046}_{-0.038}$	0.150	−0.205	0.047	−0.046
13 - 16	14.32	0.059	0.071	$^{+0.106}_{-0.101}$	0.138	−0.192	0.014	0.010
16 - 20	17.73	0.033	0.058	$^{+0.114}_{-0.106}$	0.133	−0.187	−0.018	0.062
20 - 25	22.06	0.017	0.068	$^{+0.110}_{-0.080}$	0.115	−0.167	−0.020	0.064
25 - 30	27.16	0.008	0.044	$^{+0.482}_{-0.467}$	0.092	−0.140	−0.013	0.044
30 - 50	36.25	0.006	0.054	$^{+0.313}_{-0.277}$	0.084	−0.133	−0.032	0.073

Table 8.8: The $\Upsilon(nS)$ differential $|y|$ cross sections and the relative statistical and systematic uncertainties from each source for the unpolarized scenario. The luminosity uncertainty of 4% is not shown in the table.

$\Upsilon(1S)$											
$\lvert y \rvert$	$\lvert y^{mean} \rvert$	σ(nb)	stat/σ	syst/σ	ϵ_{trig}/σ	ϵ_{muid}/σ	ρ/σ	sigPDF/σ	bgPDF/σ	msc/σ	mig/σ
0.0 - 0.4	0.208	1.429	0.018	$^{+0.063}_{-0.059}$	$^{+0.025}_{-0.024}$	$^{+0.021}_{-0.006}$	0.007	0.053	0.000	0.001	0.000
0.4 - 0.8	0.611	1.534	0.017	$^{+0.050}_{-0.049}$	$^{+0.023}_{-0.022}$	$^{+0.016}_{-0.007}$	0.014	0.041	0.000	0.000	0.000
0.8 - 1.2	1.004	1.562	0.015	$^{+0.037}_{-0.039}$	$^{+0.020}_{-0.019}$	$^{+0.010}_{-0.008}$	0.016	0.029	0.000	0.006	0.001
1.2 - 1.6	1.395	1.492	0.014	$^{+0.037}_{-0.035}$	$^{+0.019}_{-0.016}$	$^{+0.010}_{-0.009}$	0.004	0.030	0.000	0.001	0.001
1.6 - 2.0	1.786	1.306	0.015	$^{+0.041}_{-0.039}$	$^{+0.020}_{-0.016}$	$^{+0.011}_{-0.010}$	0.004	0.034	0.002	0.000	0.000
2.0 - 2.4	2.126	1.023	0.022	$^{+0.028}_{-0.025}$	$^{+0.020}_{-0.016}$	$^{+0.011}_{-0.010}$	0.001	0.013	0.010	0.000	0.002
$\Upsilon(2S)$											
$\lvert y \rvert$	$\lvert y^{mean} \rvert$	σ(nb)	stat/σ	syst/σ	ϵ_{trig}/σ	ϵ_{muid}/σ	ρ/σ	sigPDF/σ	bgPDF/σ	msc/σ	mig/σ
0.0 - 0.4	0.208	0.400	0.034	$^{+0.074}_{-0.070}$	$^{+0.026}_{-0.024}$	$^{+0.022}_{-0.006}$	$^{+0.007}_{-0.000}$	0.065	0.000	0.001	0.001
0.4 - 0.8	0.611	0.457	0.034	$^{+0.057}_{-0.054}$	$^{+0.023}_{-0.022}$	$^{+0.016}_{-0.007}$	$^{+0.008}_{-0.007}$	0.048	0.002	0.000	0.001
0.8 - 1.2	1.004	0.453	0.035	$^{+0.052}_{-0.051}$	$^{+0.021}_{-0.019}$	$^{+0.010}_{-0.008}$	$^{+0.007}_{-0.009}$	0.046	0.003	0.001	0.000
1.2 - 1.6	1.395	0.398	0.037	$^{+0.053}_{-0.052}$	$^{+0.020}_{-0.016}$	$^{+0.010}_{-0.009}$	$^{+0.001}_{-0.003}$	0.048	0.000	0.000	0.000
1.6 - 2.0	1.786	0.301	0.042	$^{+0.065}_{-0.063}$	$^{+0.018}_{-0.012}$	$^{+0.010}_{-0.008}$	$^{+0.000}_{-0.001}$	0.055	0.026	0.000	0.001
2.0 - 2.4	2.126	0.265	0.063	$^{+0.182}_{-0.182}$	$^{+0.019}_{-0.013}$	$^{+0.011}_{-0.009}$	$^{+0.001}_{-0.001}$	0.050	0.173	0.022	0.002
$\Upsilon(3S)$											
$\lvert y \rvert$	$\lvert y^{mean} \rvert$	σ(nb)	stat/σ	syst/σ	ϵ_{trig}/σ	ϵ_{muid}/σ	ρ/σ	sigPDF/σ	bgPDF/σ	msc/σ	mig/σ
0.0 - 0.4	0.208	0.198	0.036	$^{+0.098}_{-0.095}$	$^{+0.026}_{-0.024}$	$^{+0.022}_{-0.006}$	0.008	0.092	0.000	0.001	0.001
0.4 - 0.8	0.611	0.220	0.036	$^{+0.080}_{-0.077}$	$^{+0.024}_{-0.022}$	$^{+0.016}_{-0.007}$	0.015	0.073	0.002	0.000	0.000
0.8 - 1.2	1.004	0.215	0.055	$^{+0.071}_{-0.068}$	$^{+0.021}_{-0.018}$	$^{+0.010}_{-0.008}$	0.016	0.065	0.003	0.006	0.000
1.2 - 1.6	1.395	0.228	0.044	$^{+0.070}_{-0.068}$	$^{+0.021}_{-0.016}$	$^{+0.011}_{-0.009}$	0.003	0.066	0.000	0.002	0.001
1.6 - 2.0	1.786	0.157	0.058	$^{+0.086}_{-0.084}$	$^{+0.021}_{-0.013}$	$^{+0.011}_{-0.008}$	0.000	0.077	0.031	0.001	0.001
2.0 - 2.4	2.126	0.158	0.074	$^{+0.110}_{-0.108}$	$^{+0.024}_{-0.016}$	$^{+0.013}_{-0.010}$	0.002	0.098	0.042	0.008	0.002

Table 8.9: The $\Upsilon(nS)$ differential $|y|$ cross sections and the relative statistical and systematic uncertainties from each source including different polarization scenarios (transversely polarized in the helicity frame (HX T), longitudinally polarized in the helicity frame (HX L), transversely polarized in the Collins-Soper frame (CS T), and longitudinally polarized in the Collins-Soper frame(CS L)). The luminosity uncertainty of 4% is not shown in the table.

$\Upsilon(1S)$								
$\lvert y\rvert$	$\lvert y^{mean}\rvert$	σ(nb)	stat/σ	syst/σ	HX T	HX L	CS T	CS L
0.0 - 0.4	0.208	1.429	0.018	${}^{+0.063}_{-0.059}$	0.222	-0.265	0.134	-0.164
0.4 - 0.8	0.611	1.534	0.017	${}^{+0.050}_{-0.049}$	0.217	-0.262	0.109	-0.141
0.8 - 1.2	1.004	1.562	0.015	${}^{+0.037}_{-0.039}$	0.209	-0.256	0.121	-0.159
1.2 - 1.6	1.395	1.492	0.014	${}^{+0.037}_{-0.035}$	0.198	-0.247	0.149	-0.190
1.6 - 2.0	1.786	1.306	0.015	${}^{+0.041}_{-0.039}$	0.179	-0.231	0.202	-0.244
2.0 - 2.4	2.126	1.023	0.022	${}^{+0.028}_{-0.025}$	0.197	-0.244	0.284	-0.306
$\Upsilon(2S)$								
$\lvert y\rvert$	$\lvert y^{mean}\rvert$	σ(nb)	stat/σ	syst/σ	HX T	HX L	CS T	CS L
0.0 - 0.4	0.208	0.400	0.034	${}^{+0.074}_{-0.070}$	0.189	-0.238	0.116	-0.144
0.4 - 0.8	0.611	0.457	0.034	${}^{+0.057}_{-0.054}$	0.197	-0.247	0.106	-0.140
0.8 - 1.2	1.004	0.453	0.035	${}^{+0.052}_{-0.051}$	0.191	-0.243	0.116	-0.154
1.2 - 1.6	1.395	0.398	0.037	${}^{+0.053}_{-0.052}$	0.182	-0.234	0.134	-0.175
1.6 - 2.0	1.786	0.301	0.042	${}^{+0.065}_{-0.063}$	0.161	-0.214	0.181	-0.222
2.0 - 2.4	2.126	0.265	0.063	${}^{+0.182}_{-0.182}$	0.164	-0.216	0.277	-0.301
$\Upsilon(3S)$								
$\lvert y\rvert$	$\lvert y^{mean}\rvert$	σ(nb)	stat/σ	syst/σ	HX T	HX L	CS T	CS L
0.0 - 0.4	0.208	0.198	0.036	${}^{+0.098}_{-0.095}$	0.174	-0.225	0.105	-0.131
0.4 - 0.8	0.611	0.220	0.036	${}^{+0.080}_{-0.077}$	0.184	-0.237	0.099	-0.131
0.8 - 1.2	1.004	0.215	0.055	${}^{+0.071}_{-0.068}$	0.179	-0.232	0.103	-0.138
1.2 - 1.6	1.395	0.228	0.044	${}^{+0.070}_{-0.068}$	0.172	-0.226	0.127	-0.167
1.6 - 2.0	1.786	0.157	0.058	${}^{+0.086}_{-0.084}$	0.150	-0.204	0.175	-0.217
2.0 - 2.4	2.126	0.158	0.074	${}^{+0.110}_{-0.108}$	0.164	-0.214	0.275	-0.299

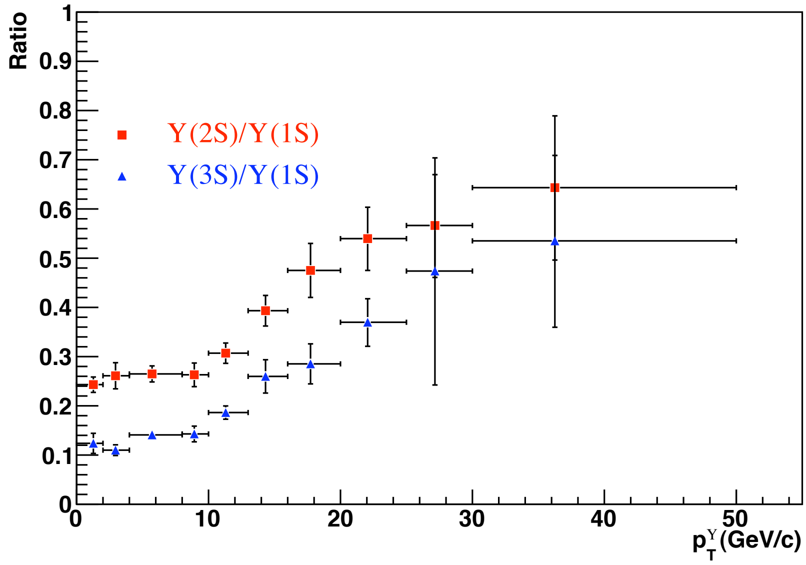

Figure 8.4: Ratio of the differential cross section times $B_{\mu\mu}$ of the $\Upsilon(2S)$ to $\Upsilon(1S)$ and the $\Upsilon(3S)$ to $\Upsilon(1S)$ as a function of p_T in the rapidity range $|y| < 2.4$ for the unpolarized scenario.

Table 8.10: Ratio of the differential cross section times $B_{\mu\mu}$ of the $\Upsilon(nS)$ cross sections for the unpolarized scenario. The uncertainties include statistical and systematic only.

p_T(GeV/c)	p_T^{mean}(GeV/c)	$\sigma(\Upsilon(2S))/\sigma(\Upsilon(1S))$	$\sigma(\Upsilon(3S))/\sigma(\Upsilon(1S))$
0 - 2	1.27	$0.243\ {}^{+0.015\ (0.012(stat),\ 0.010(syst))}_{-0.016\ (0.012(stat),\ 0.010(syst))}$	$0.124\ {}^{+0.020\ (0.010(stat),\ 0.018(syst))}_{-0.021\ (0.010(stat),\ 0.018(syst))}$
2 - 4	2.95	$0.261\ {}^{+0.027\ (0.009(stat),\ 0.025(syst))}_{-0.027\ (0.009(stat),\ 0.025(syst))}$	$0.110\ {}^{+0.011\ (0.005(stat),\ 0.009(syst))}_{-0.011\ (0.005(stat),\ 0.009(syst))}$
4 - 8	5.72	$0.265\ {}^{+0.016\ (0.008(stat),\ 0.014(syst))}_{-0.016\ (0.008(stat),\ 0.014(syst))}$	$0.141\ {}^{+0.011\ (0.005(stat),\ 0.009(syst))}_{-0.011\ (0.005(stat),\ 0.009(syst))}$
8 - 10	8.92	$0.263\ {}^{+0.024\ (0.014(stat),\ 0.019(syst))}_{-0.024\ (0.014(stat),\ 0.020(syst))}$	$0.143\ {}^{+0.016\ (0.009(stat),\ 0.013(syst))}_{-0.016\ (0.009(stat),\ 0.013(syst))}$
10 - 13	11.30	$0.307\ {}^{+0.021\ (0.015(stat),\ 0.014(syst))}_{-0.021\ (0.015(stat),\ 0.014(syst))}$	$0.186\ {}^{+0.013\ (0.010(stat),\ 0.009(syst))}_{-0.014\ (0.010(stat),\ 0.010(syst))}$
13 - 16	14.32	$0.393\ {}^{+0.031\ (0.026(stat),\ 0.017(syst))}_{-0.031\ (0.026(stat),\ 0.017(syst))}$	$0.260\ {}^{+0.034\ (0.020(stat),\ 0.027(syst))}_{-0.034\ (0.020(stat),\ 0.027(syst))}$
16 - 20	17.73	$0.475\ {}^{+0.055\ (0.033(stat),\ 0.044(syst))}_{-0.055\ (0.033(stat),\ 0.044(syst))}$	$0.285\ {}^{+0.041\ (0.019(stat),\ 0.036(syst))}_{-0.041\ (0.019(stat),\ 0.036(syst))}$
20 - 25	22.06	$0.540\ {}^{+0.064\ (0.046(stat),\ 0.045(syst))}_{-0.065\ (0.046(stat),\ 0.046(syst))}$	$0.370\ {}^{+0.048\ (0.031(stat),\ 0.036(syst))}_{-0.049\ (0.031(stat),\ 0.038(syst))}$
25 - 30	27.16	$0.566\ {}^{+0.103\ (0.069(stat),\ 0.077(syst))}_{-0.106\ (0.069(stat),\ 0.080(syst))}$	$0.474\ {}^{+0.230\ (0.040(stat),\ 0.226(syst))}_{-0.232\ (0.040(stat),\ 0.228(syst))}$
30 - 50	36.25	$0.643\ {}^{+0.146\ (0.088(stat),\ 0.116(syst))}_{-0.147\ (0.088(stat),\ 0.118(syst))}$	$0.535\ {}^{+0.174\ (0.054(stat),\ 0.165(syst))}_{-0.175\ (0.054(stat),\ 0.167(syst))}$
0 - 50	5.40	$0.268\ {}^{+0.019\ (0.004(stat),\ 0.018(syst))}_{-0.018\ (0.004(stat),\ 0.017(syst))}$	$0.135\ {}^{+0.013\ (0.003(stat),\ 0.012(syst))}_{-0.013\ (0.003(stat),\ 0.012(syst))}$

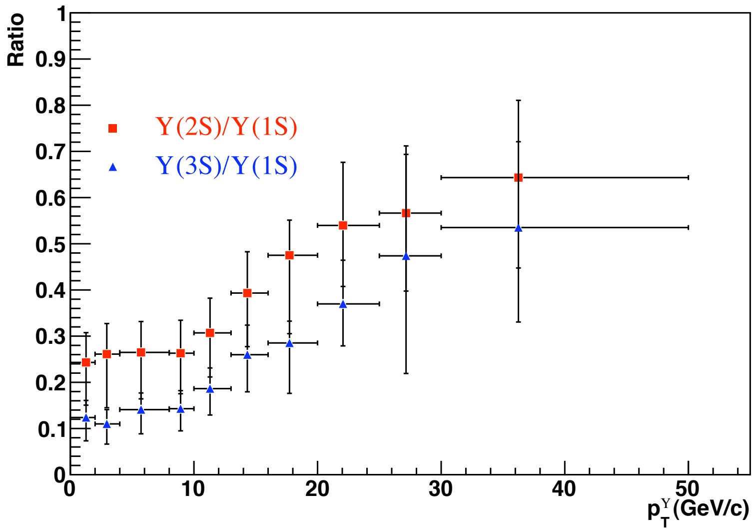

Figure 8.5: Ratio of the differential cross section times $B_{\mu\mu}$ of the $\Upsilon(2S)$ to $\Upsilon(1S)$ and the $\Upsilon(3S)$ to $\Upsilon(1S)$ as a function of p_T in the rapidity range $|y| < 2.4$ with the maximum variation in the polarization

Table 8.11: Ratio of the differential cross section times $B_{\mu\mu}$ of the $\Upsilon(nS)$ cross sections with the maximum variation in the polarization. The uncertainties include statistical, systematic and polarization.

p_T(GeV/c)	p_T^{mean}(GeV/c)	$\sigma(\Upsilon(2S))/\sigma(\Upsilon(1S))$	$\sigma(\Upsilon(3S))/\sigma(\Upsilon(1S))$
0 - 2	1.27	$0.243\,^{+0.064\ (0.015(stat+syst),\ 0.063(pol))}_{-0.093\ (0.016(stat+syst),\ 0.091(pol))}$	$0.124\,^{+0.037\ (0.020(stat+syst),\ 0.031(pol))}_{-0.051\ (0.021(stat+syst),\ 0.046(pol))}$
2 - 4	2.95	$0.261\,^{+0.066\ (0.027(stat+syst),\ 0.061(pol))}_{-0.116\ (0.027(stat+syst),\ 0.113(pol))}$	$0.110\,^{+0.031\ (0.011(stat+syst),\ 0.029(pol))}_{-0.044\ (0.011(stat+syst),\ 0.042(pol))}$
4 - 8	5.72	$0.265\,^{+0.067\ (0.016(stat+syst),\ 0.065(pol))}_{-0.101\ (0.016(stat+syst),\ 0.099(pol))}$	$0.141\,^{+0.036\ (0.011(stat+syst),\ 0.034(pol))}_{-0.052\ (0.011(stat+syst),\ 0.051(pol))}$
8 - 10	8.92	$0.263\,^{+0.071\ (0.024(stat+syst),\ 0.067(pol))}_{-0.088\ (0.024(stat+syst),\ 0.084(pol))}$	$0.143\,^{+0.039\ (0.016(stat+syst),\ 0.036(pol))}_{-0.048\ (0.016(stat+syst),\ 0.045(pol))}$
10 - 13	11.30	$0.307\,^{+0.075\ (0.021(stat+syst),\ 0.072(pol))}_{-0.095\ (0.021(stat+syst),\ 0.093(pol))}$	$0.186\,^{+0.045\ (0.013(stat+syst),\ 0.043(pol))}_{-0.057\ (0.014(stat+syst),\ 0.055(pol))}$
13 - 16	14.32	$0.393\,^{+0.089\ (0.031(stat+syst),\ 0.084(pol))}_{-0.116\ (0.031(stat+syst),\ 0.112(pol))}$	$0.260\,^{+0.064\ (0.034(stat+syst),\ 0.054(pol))}_{-0.080\ (0.034(stat+syst),\ 0.073(pol))}$
16 - 20	17.73	$0.475\,^{+0.076\ (0.055(stat+syst),\ 0.053(pol))}_{-0.170\ (0.055(stat+syst),\ 0.161(pol))}$	$0.285\,^{+0.047\ (0.041(stat+syst),\ 0.024(pol))}_{-0.109\ (0.041(stat+syst),\ 0.101(pol))}$
20 - 25	22.06	$0.540\,^{+0.137\ (0.064(stat+syst),\ 0.121(pol))}_{-0.132\ (0.065(stat+syst),\ 0.115(pol))}$	$0.370\,^{+0.095\ (0.048(stat+syst),\ 0.082(pol))}_{-0.091\ (0.049(stat+syst),\ 0.077(pol))}$
25 - 30	27.16	$0.566\,^{+0.127\ (0.103(stat+syst),\ 0.074(pol))}_{-0.169\ (0.106(stat+syst),\ 0.132(pol))}$	$0.474\,^{+0.238\ (0.230(stat+syst),\ 0.061(pol))}_{-0.255\ (0.232(stat+syst),\ 0.106(pol))}$
30 - 50	36.25	$0.643\,^{+0.167\ (0.146(stat+syst),\ 0.082(pol))}_{-0.196\ (0.147(stat+syst),\ 0.129(pol))}$	$0.535\,^{+0.186\ (0.174(stat+syst),\ 0.066(pol))}_{-0.204\ (0.175(stat+syst),\ 0.105(pol))}$
0 - 50	5.40	$0.268\,^{+0.076\ (0.019(stat+syst),\ 0.074(pol))}_{-0.094\ (0.018(stat+syst),\ 0.092(pol))}$	$0.135\,^{+0.038\ (0.013(stat+syst),\ 0.036(pol))}_{-0.048\ (0.013(stat+syst),\ 0.046(pol))}$

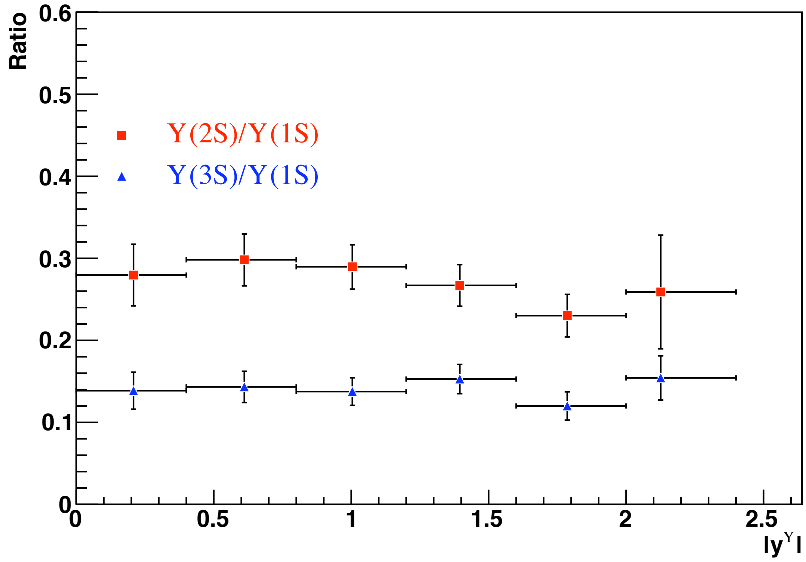

Figure 8.6: Ratio of the differential cross section times $B_{\mu\mu}$ of the $\Upsilon(nS)$ as a function of $|y|$ for $p_T < 50$ GeV/c for the unpolarized scenario.

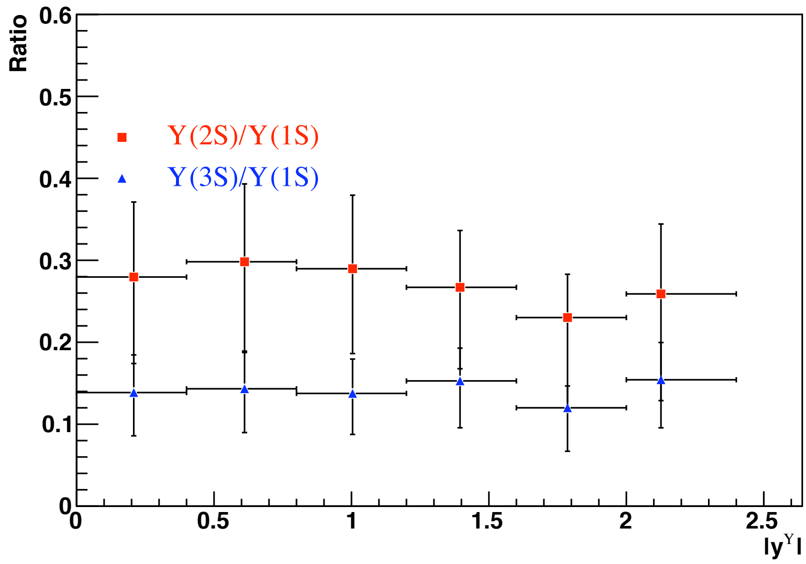

Figure 8.7: Ratio of the differential cross section times $B_{\mu\mu}$ of the $\Upsilon(nS)$ as a function of $|y|$ for $p_T < 50$ GeV/c with the maximum variation in the polarization.

Table 8.12: Ratio of the differential cross section times $B_{\mu\mu}$ of the $\Upsilon(nS)$ cross sections for the unpolarized scenario. The uncertainties include statistical and systematic only.

$\|y\|$	$\|y\|^{mean}$	$\sigma(\Upsilon(2S))/\sigma(\Upsilon(1S))$	$\sigma(\Upsilon(3S))/\sigma(\Upsilon(1S))$
0.0 - 0.4	0.208	$0.280 \begin{smallmatrix} +0.026\ (0.011(stat),\ 0.024(syst)) \\ -0.026\ (0.011(stat),\ 0.024(syst)) \end{smallmatrix}$	$0.139 \begin{smallmatrix} +0.016\ (0.006(stat),\ 0.015(syst)) \\ -0.016\ (0.006(stat),\ 0.015(syst)) \end{smallmatrix}$
0.4 - 0.8	0.611	$0.298 \begin{smallmatrix} +0.022\ (0.011(stat),\ 0.019(syst)) \\ -0.022\ (0.011(stat),\ 0.019(syst)) \end{smallmatrix}$	$0.143 \begin{smallmatrix} +0.013\ (0.006(stat),\ 0.012(syst)) \\ -0.013\ (0.006(stat),\ 0.012(syst)) \end{smallmatrix}$
0.8 - 1.2	1.004	$0.290 \begin{smallmatrix} +0.019\ (0.011(stat),\ 0.016(syst)) \\ -0.020\ (0.011(stat),\ 0.017(syst)) \end{smallmatrix}$	$0.138 \begin{smallmatrix} +0.013\ (0.008(stat),\ 0.010(syst)) \\ -0.013\ (0.008(stat),\ 0.010(syst)) \end{smallmatrix}$
1.2 - 1.6	1.395	$0.267 \begin{smallmatrix} +0.019\ (0.011(stat),\ 0.015(syst)) \\ -0.019\ (0.011(stat),\ 0.015(syst)) \end{smallmatrix}$	$0.153 \begin{smallmatrix} +0.013\ (0.008(stat),\ 0.011(syst)) \\ -0.013\ (0.008(stat),\ 0.011(syst)) \end{smallmatrix}$
1.6 - 2.0	1.786	$0.230 \begin{smallmatrix} +0.019\ (0.010(stat),\ 0.016(syst)) \\ -0.019\ (0.010(stat),\ 0.016(syst)) \end{smallmatrix}$	$0.120 \begin{smallmatrix} +0.013\ (0.007(stat),\ 0.011(syst)) \\ -0.013\ (0.007(stat),\ 0.011(syst)) \end{smallmatrix}$
2.0 - 2.4	2.126	$0.259 \begin{smallmatrix} +0.050\ (0.017(stat),\ 0.047(syst)) \\ -0.050\ (0.017(stat),\ 0.047(syst)) \end{smallmatrix}$	$0.154 \begin{smallmatrix} +0.020\ (0.012(stat),\ 0.017(syst)) \\ -0.020\ (0.012(stat),\ 0.017(syst)) \end{smallmatrix}$

Table 8.13: Ratio of the differential cross section times $B_{\mu\mu}$ of the $\Upsilon(nS)$ cross sections with the maximum variation in the polarization.

$\|y\|$	$\|y\|^{mean}$	$\sigma(\Upsilon(2S))/\sigma(\Upsilon(1S))$	$\sigma(\Upsilon(3S))/\sigma(\Upsilon(1S))$
0.0 - 0.4	0.208	$0.280 \begin{smallmatrix} +0.087\ (0.026(stat{+}syst),\ 0.083(pol)) \\ -0.102\ (0.026(stat{+}syst),\ 0.099(pol)) \end{smallmatrix}$	$0.139 \begin{smallmatrix} +0.043\ (0.016(stat{+}syst),\ 0.040(pol)) \\ -0.050\ (0.016(stat{+}syst),\ 0.048(pol)) \end{smallmatrix}$
0.4 - 0.8	0.611	$0.298 \begin{smallmatrix} +0.092\ (0.022(stat{+}syst),\ 0.090(pol)) \\ -0.108\ (0.022(stat{+}syst),\ 0.106(pol)) \end{smallmatrix}$	$0.143 \begin{smallmatrix} +0.044\ (0.013(stat{+}syst),\ 0.042(pol)) \\ -0.052\ (0.013(stat{+}syst),\ 0.050(pol)) \end{smallmatrix}$
0.8 - 1.2	1.004	$0.290 \begin{smallmatrix} +0.088\ (0.019(stat{+}syst),\ 0.086(pol)) \\ -0.102\ (0.020(stat{+}syst),\ 0.100(pol)) \end{smallmatrix}$	$0.138 \begin{smallmatrix} +0.040\ (0.013(stat{+}syst),\ 0.036(pol)) \\ -0.049\ (0.013(stat{+}syst),\ 0.054(pol)) \end{smallmatrix}$
1.2 - 1.6	1.395	$0.267 \begin{smallmatrix} +0.067\ (0.019(stat{+}syst),\ 0.065(pol)) \\ -0.098\ (0.019(stat{+}syst),\ 0.096(pol)) \end{smallmatrix}$	$0.153 \begin{smallmatrix} +0.038\ (0.013(stat{+}syst),\ 0.105(pol)) \\ -0.056\ (0.013(stat{+}syst),\ 0.105(pol)) \end{smallmatrix}$
1.6 - 2.0	1.786	$0.230 \begin{smallmatrix} +0.050\ (0.019(stat{+}syst),\ 0.046(pol)) \\ -0.110\ (0.019(stat{+}syst),\ 0.108(pol)) \end{smallmatrix}$	$0.120 \begin{smallmatrix} +0.024\ (0.013(stat{+}syst),\ 0.020(pol)) \\ -0.052\ (0.013(stat{+}syst),\ 0.050(pol)) \end{smallmatrix}$
2.0 - 2.4	2.126	$0.259 \begin{smallmatrix} +0.071\ (0.050(stat{+}syst),\ 0.050(pol)) \\ -0.121\ (0.050(stat{+}syst),\ 0.110(pol)) \end{smallmatrix}$	$0.154 \begin{smallmatrix} +0.042\ (0.020(stat{+}syst),\ 0.037(pol)) \\ -0.056\ (0.020(stat{+}syst),\ 0.052(pol)) \end{smallmatrix}$

Chapter 9

Comparison of Results with Theoretical Predictions and Other Experiments

The analysis presented in this thesis of the initial LHC collision data acquired by the CMS experiment in 2010, corresponding to an integrated luminosity of 36.7 ± 1.5 pb^{-1}, yields a measurement of the $\Upsilon(nS)$ integrated production (unpolarized scenario) cross sections times branching fraction at $\sqrt{s} = 7$ TeV for $|y| < 2.4$:

$$\sigma(pp \to \Upsilon(1S)X) \cdot \mathcal{B}(\Upsilon(1S) \to \mu^+\mu^-) = 8.347 \pm 0.056 \text{ (stat.) } {}^{+0.365}_{-0.350} \text{ (syst.) } \pm 0.334 \text{ (lumi.) nb}\,,$$
$$\sigma(pp \to \Upsilon(2S)X) \cdot \mathcal{B}(\Upsilon(2S) \to \mu^+\mu^-) = 2.274 \pm 0.034 \text{ (stat.) } {}^{+0.138}_{-0.130} \text{ (syst.) } \pm 0.086 \text{ (lumi.) nb}\,,$$
$$\sigma(pp \to \Upsilon(3S)X) \cdot \mathcal{B}(\Upsilon(3S) \to \mu^+\mu^-) = 1.175 \pm 0.021 \text{ (stat.) } {}^{+0.101}_{-0.098} \text{ (syst.) } \pm 0.046 \text{ (lumi.) nb}\,.$$

The $\Upsilon(nS)$ differential p_T cross sections, normalized to the total cross sections, are compared to the previous results from CDF [3] and D0 [2] in Figure 9.1. The results are in good agreement.

The comparisons of the $\Upsilon(1S)$ and $\Upsilon(3S)$ cross section results, for the unpolarized scenario and the rapidity region $|y^{\Upsilon}| < 2$ with the NLO and NNLO* predictions of the CSM model are shown in Figure 9.2. The CSM model predicts only direct production. In order to compare the direct + feed-down results for $\Upsilon(1S)$ with the CSM model, the CSM predictions are scaled up by the fraction of the direct production of $\Upsilon(1S)$: $F_{direct} = 0.51 \pm 0.12$ [52]. This correction is not needed for the $\Upsilon(3S)$ since it is always directly produced (no χ_b states above it). The comparison of the $\Upsilon(2S)$ is not shown, since the fraction of the direct production of $\Upsilon(2S)$ is not yet known. The NNLO* predictions are in reasonable agreement with the measurements at low p_T, but with increasing p_T the discrepancy becomes larger.

The comparison of the $\Upsilon(1S)$ cross section results for the unpolarized scenario, and the rapidity region $|y^{\Upsilon}| < 2$ with the predictions of the COM model up to $p_T = 30$ GeV/c is shown in Figure 9.3. The NRQCD predictions are in good agreement with the experimental measurements.

The $\Upsilon(1S)$ p_T-integrated differential y cross section results from CMS and LHCb [10] are shown in Figure 9.4. The LHCb detector covers the rapidity range; $2 < y^{\Upsilon} < 4.5$. Where the two measurements overlap, there is good agreement.

The $\Upsilon(nS)$ differential p_T cross sections for the rapidity region $|y^{\Upsilon}| < 2$ are compared to the earlier CMS results [11], using the first 3.1 pb^{-1} of data, in Figure 9.5. There is no overlap in data for the two results. The results are in good agreement.

The ATLAS collaboration published cross-section results for the $\Upsilon(1S)$ only within the fiducial acceptance of the ATLAS detector [88]. So, it is not possible to compare the results in this thesis with the ATLAS results.

The Pythia MC simulation, including color-singlet and color-octet mechanisms to leading-order, fail to predict the cross section measurements. Figure 9.6 shows the comparison of the $\Upsilon(nS)$ p_T- and $|y|$-differential cross sections, and the $\sigma(\Upsilon(3S))/\sigma(\Upsilon(1S))$ and $\sigma(\Upsilon(2S))/\sigma(\Upsilon(1S))$ ratios as a function of p_T and $|y|$ with the Pythia MC predictions. The Pythia predictions for the total cross sections are 16.4 nb, 5.939 nb, and 1.624 nb for $\Upsilon(1S)$, $\Upsilon(2S)$, and $\Upsilon(3S)$, respectively. Although these are off by factors of 2, 2.8, and 1.4 for $\Upsilon(1S)$, $\Upsilon(2S)$, and $\Upsilon(3S)$, the Pythia predictions have roughly the correct shape for both the p_T- and $|y|$-differential cross sections, as shown in Figure 9.7.

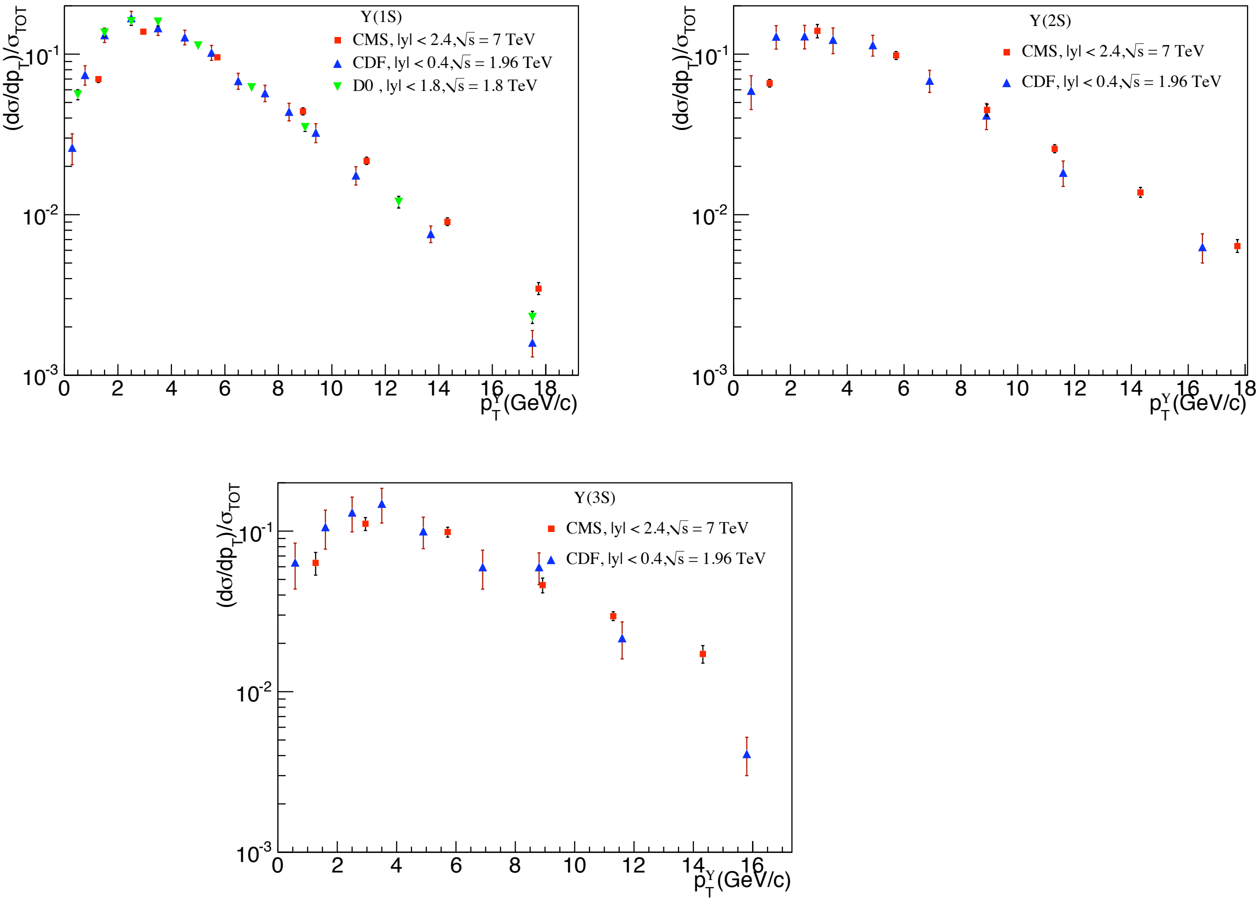

Figure 9.1: Comparison of the normalized differential p_T cross-section results. (Upper-left) $\Upsilon(1S)$ results from this thesis (CMS), CDF [3], and D0 [2]. (Upper-right) $\Upsilon(2S)$ results from this thesis (CMS) and CDF. (Bottom) $\Upsilon(3S)$ results from this thesis (CMS) and CDF. The uncertainties include statistical and systematic only.

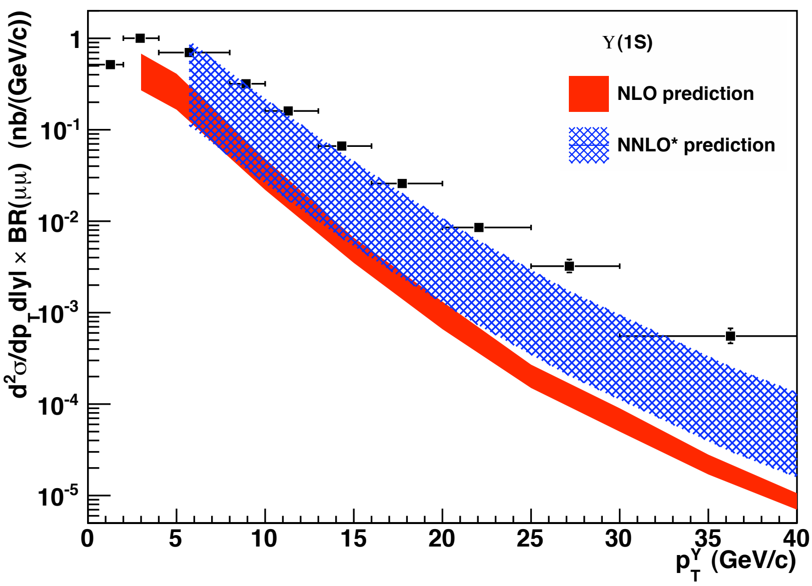

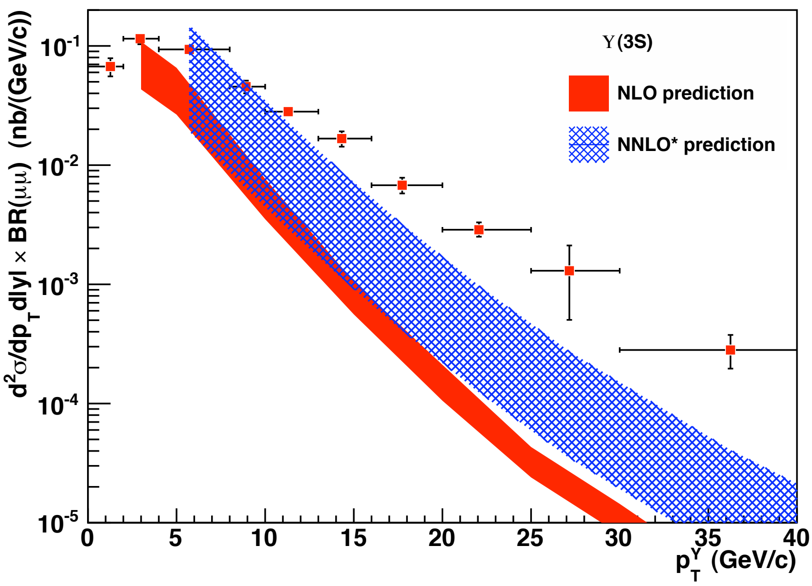

Figure 9.2: Comparison of the $\Upsilon(1S)$ (top) and $\Upsilon(3S)$ (bottom) differential cross sections as a function of p_T with the CSM predictions. The red band is the NLO prediction and its uncertainties, and the blue band is the NNLO* prediction and uncertainties. Both predictions for the $\Upsilon(1S)$ have been scaled up to account for non-direct production.

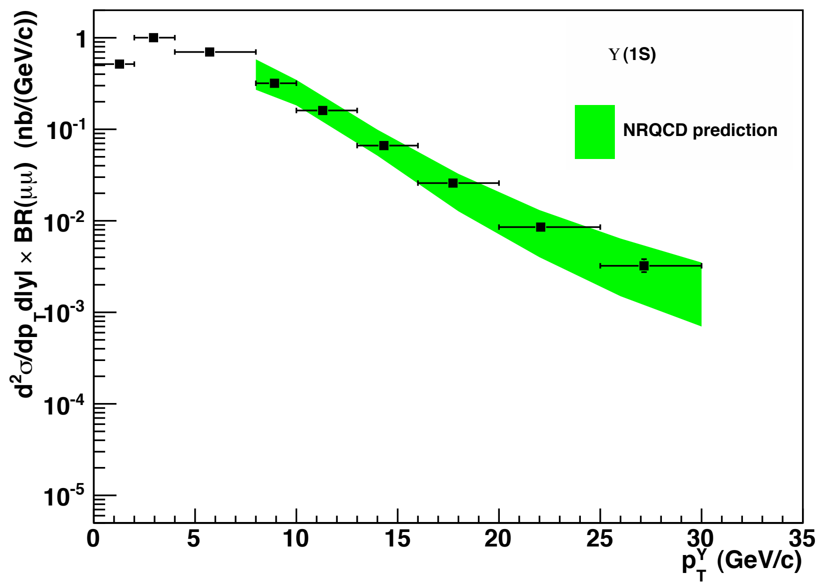

Figure 9.3: The comparison of the $\Upsilon(1S)$ differential p_T cross-section results with the NRQCD predictions. The band shows the uncertainties on the predictions.

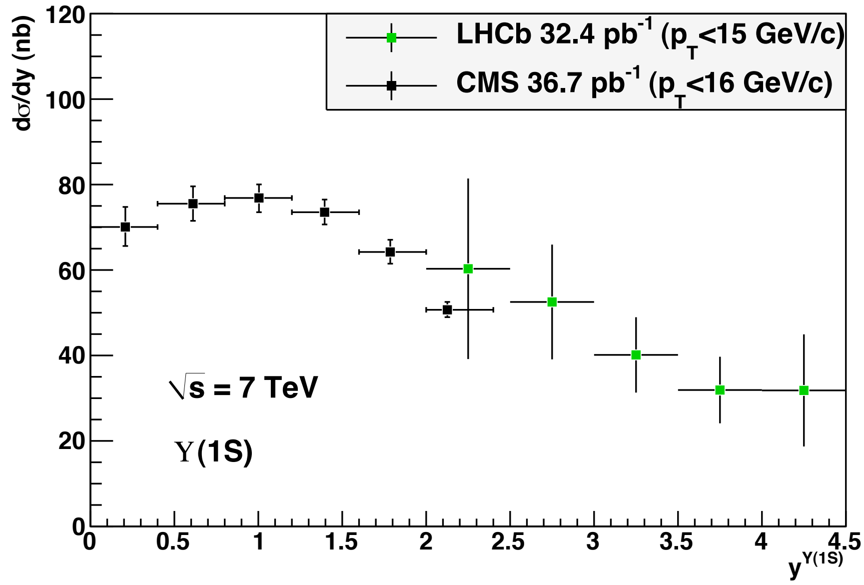

Figure 9.4: Differential $\Upsilon(1S)$ y^{Υ} cross-section results from this thesis (CMS) and LHCb [10].

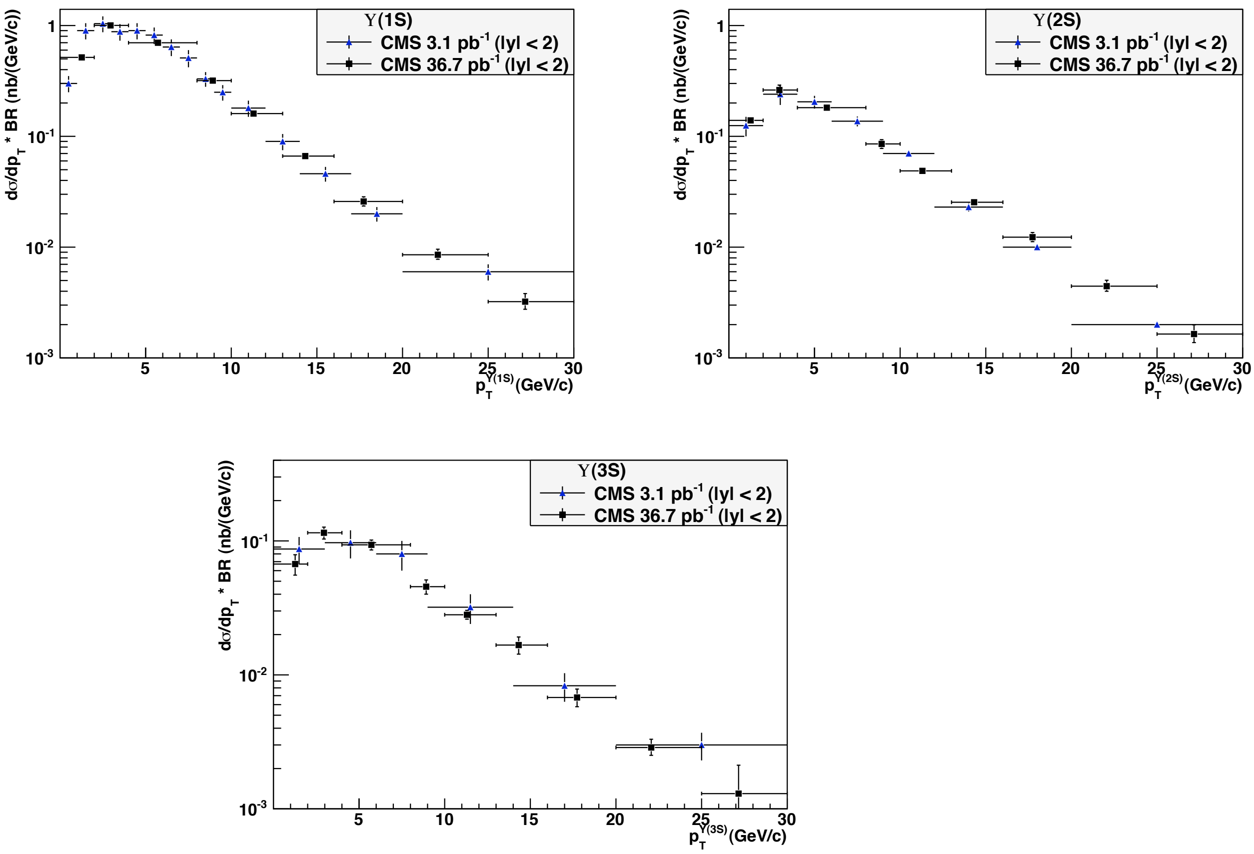

Figure 9.5: Comparison of the $\Upsilon(nS)$ differential p_T cross-section results from this thesis with the earlier CMS measurements [11]. (Upper-left) $\Upsilon(1S)$. (Upper-right) $\Upsilon(2S)$. (Bottom) $\Upsilon(3S)$.

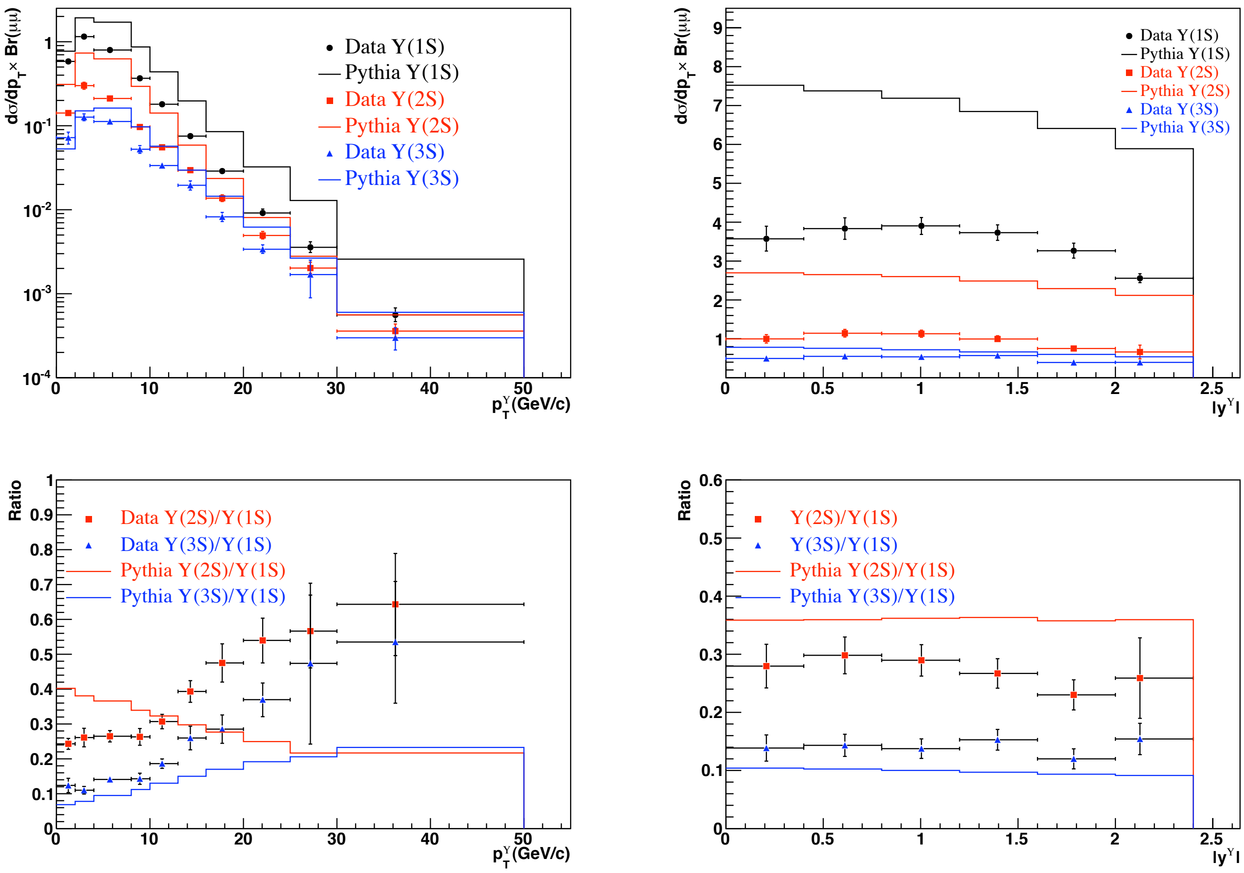

Figure 9.6: Comparisons of the $\Upsilon(nS)$ differential p_T (upper-left) and $|y^{\Upsilon}|$ (upper-right) cross-section results and the $\sigma(\Upsilon(2S))/\sigma(\Upsilon(1S))$ and $\sigma(\Upsilon(3S))/\sigma(\Upsilon(1S))$ ratios as a function of p_T (lower-left) and $|y^{\Upsilon}|$ (lower-right) with the predictions from Pythia.

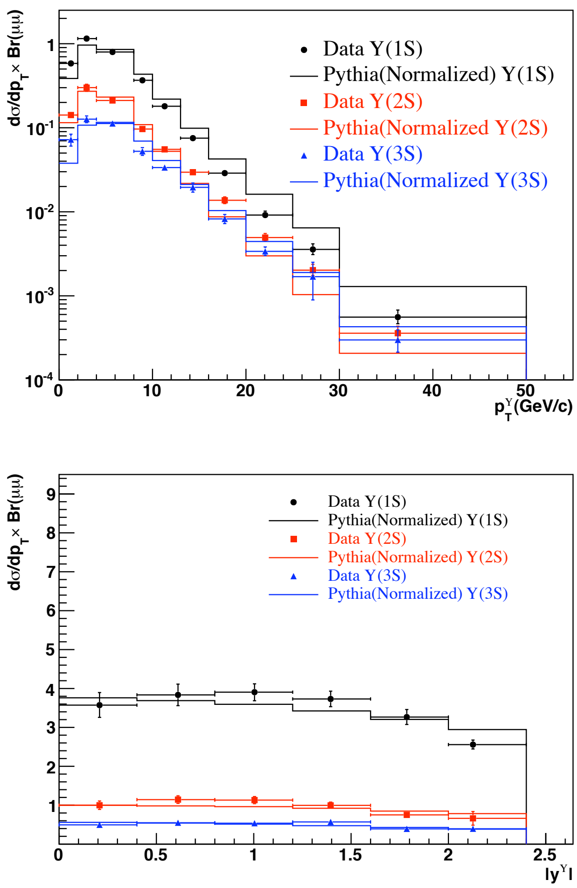

Figure 9.7: Comparisons of the $\Upsilon(nS)$ differential p_T (top) and $|y^{\Upsilon}|$ (bottom) cross-section results with the normalized predictions from Pythia.

Chapter 10

Summary and Conclusions

In this thesis, measurements of the $\Upsilon(nS)$ total production cross sections in the dimuon channel from pp collisions at $\sqrt{s} = 7$ TeV, with the CMS experiment have been presented. The differential cross section for each $\Upsilon(nS)$ state has also been measured as a function of p_T and rapidity. The differential measurements have been compared to theory and to previous experimental results. The NRQCD predictions with the COM mechanism agree with the results better than the CSM model predictions. The normalized p_T distributions are in agreement with previous Tevatron results. Finally, the cross section ratios of the three $\Upsilon(nS)$ have been measured. The cross section ratios increase with increasing p_T and are constant as a function of $|y^{\Upsilon}|$.

The dominant sources of systematic uncertainty on the cross-section measurements arise from the TNP determination of the muon identification and trigger efficiencies and from the signal function shape for high upsilon p_T. The nominal cross-section values obtained in this thesis assume unpolarized $\Upsilon(nS)$ production. Scenarios of extreme polarization variations have been studied also, yielding variations on the measured cross-section values of up to 20%. As the CMS data sample increases, a reduction in the size of these dominating systematic uncertainties should be possible. In particular, the extraction of the upsilon polarization simultaneously with the cross section will greatly decrease the systematical uncertainty from the polarization.

The measurements obtained in this thesis are in agreement with the other LHC Υ cross-section results, such as from LHCb. The results are also consistent with an earlier CMS measurements based on the first 3 pb^{-1} of data, and extend them in terms of the precision attained and the covered kinematic reach of $p_T < 50$ GeV/c and $|y| \leq 2.4$, compared to the earlier limits of 30 GeV/c and 2.0.

These Υ measurements give important information on the process of hadroproduction of heavy quarks. This thesis provides new experimental results that will serve as input to ongoing theoretical investigations of the correct description of bottomonium production.

References

[1] C. Amsler et al. *"Review of Particle Physics"*. *Phys. Rev. B* **667***, 1*, (2008).

[2] The D0 Collaboration. *"Measurement of inclusive differential cross sections for $\Upsilon(1S)$ production in $p\bar{p}$ collisions at $\sqrt{s}$ = 1.96 TeV"*. *Phys. Rev. Lett.* **94***, 232001*, (2005).

[3] The CDF Collaboration. *"Upsilon production and polarization in $p\bar{p}$ collisions at $\sqrt{s}$ = 1.8 TeV"*. *Phys. Rev. Lett.* **88***, 161802*, (2002).

[4] J.P. Lansberg P. Artoisenet, J. Campbell and F. Maltoni. *"Υ production at the Tevatron and the LHC"*. *Phys. Rev. Lett.* **101***, 152001*, (2008).

[5] Z. Conesa del Valle et al. *"Quarkonium production in high energy proton-proton and proton-nucleus collisions"*. *Nuclear Physics B* **214**, (2011).

[6] The CMS Collaboration. *"CMS Technical Design Report Volume I"*. *CERN/LHCC 2006-001*, (2006).

[7] The CMS Collaboration. *"The CMS experiment at the CERN LHC"*. *2008 JINST 3 S08004*, (2008).

[8] The CMS Collaboration. *"Tracking and Primary Vertex Results in First 7 TeV Collisions"*. *CMS Physics Analysis Summary, CMS-PAS-TRK-10-005*, (2010).

[9] J. Seixas P. Faccioli, C. Lourenco and H. K. Woehri. *"Towards the experimental clarification of quarkonium polarization"*. *ArXiv:1006.2738v1 [hep-ph]*, (2010).

[10] LHCb Collaboration. *"Measurement of the $\Upsilon(1S)$ production cross-section at sqrt(s) = 7 TeV in LHCb"*. *CERN-LHCb-CONF-2011-016*, (2011).

[11] CMS Collaboration. *"Measurement of the Inclusive Upsilon production cross section in pp collisions at sqrt(s)=7 TeV". Phys. Rev. D* **83**, *112004*, (2011).

[12] CLEO Collaboration. *"Measurement of the $\eta_b(1S)$ mass and the branching fraction for $\Upsilon(3S) \rightarrow \gamma\ \eta_b(1S)$". Phys. Rev. D* **81** *, 031104(R)*, (2010).

[13] S. Mrenna T. Sjostrand and P. Z. Skands. *"Pythia 6.4 physics and manual". Journal HEP* **05**, *026*, (2006).

[14] Michael Krämer. *"Quarkonium Production at High-Energy Colliders". Prog.Part.Nucl.Phys* **47**, *141*, (2001).

[15] M. Bargiotti and V. Vagnoni. *"Heavy Quarkonia sector in PYTHIA 6.324 : tuning, validation and perspectives at LHC(b)". CERN-LHCb-2007-042*, (2007).

[16] Trigger Study Group. https://twiki.cern.ch/twiki/bin/viewauth/cms/triggerstudies.

[17] J. J. Aubert et al. *"Experimental Observation of a Heavy Particle J". Phys. Rev. Lett.* **33**,*1404*, (1974).

[18] J. E. Augustin et al. *"Discovery of a Narrow Resonance in e^+ e^- Annihilation". Phys. Rev. Lett.* **33**, *1406*, (1974).

[19] S.W. Herb et al. *"Observation of a Dimuon Resonance at 9.5 GeV in 400-GeV Proton-Nucleus Collisions". Phys. Rev. Lett.* **39**, *252*, (1977).

[20] K. Ueno et al. *"Evidence for the Υ'' and a Search for New Narrow Resonances". Phys. Rev. Lett.* **42**, *486*, (1979).

[21] The CLEO Collaboration. *"Observation of a Fourth Upsilon State in e^+ e^- Annihilations". Phys. Rev. Lett.* **45**, *219*, (1980).

[22] G. T. Bodwin, E. Braaten, and G. P. Lepage. *"Rigorous QCD analysis of inclusive annihilation and production of heavy quarkonium". Phys. Rev. D* **51**, *1125*, (1995).

[23] F. Halzen and A. Martin. "Quarks and Leptons, An Introductory Course in Modern Particle Physics". John Wiley, (1984).

[24] D. J. Gross and F. Wilczek. *"Asymptotically Free Gauge Theories. 1". Phys. Rev. D* **8**, *3633*, (1973).

[25] H. D. Politzer. *"Reliable Perturbative Results for Strong Interactions". Phys. Rev. Lett.* **30**, *1346*, (1973).

[26] D. J. Gross and F. Wilczek. *"Ultraviolet Behavior of Non-Abelian Gauge Theories". Phys. Rev. Lett.* **30**, *1343*, (1973).

[27] H. D. Politzer. *"Asymptotic Freedom: An Approach to Strong Interactions.". Phys. Rept.* **14**, *129*, (1974).

[28] R. P. Feynman. "Quantum Electrodynamics". W. A. Benjamin, Inc., New York, (1961).

[29] S. S. Schweber. "QED and the men who made it: Dyson, Feynman, Schwinger, and Tomonaga". Princeton University Press, Princeton, N.J., (1994).

[30] Rith Povh, Scholz and Zetsche. "Particles and Nuclei: An Introduction to the Physical Concepts". Springer, (1993).

[31] H. Fritzsch. *"Producing Heavy Quark Flavors In Hadronic Collisions: A Test Of Quantum Chromodynamics". Phys. Lett. B* **67**, *217*, (1977).

[32] F. Halzen. *"Cvc For Gluons And Hadroproduction Of Quark Flavors". Phys. Lett. B* **69**, *105*, (1977).

[33] Amundson J. F et al. *"Colorless States in Perturbative QCD: Charmonium and Rapidity Gaps". Phys. Lett. B* **372**, *127*, (1996).

[34] Amundson J. F et al. *"Quantitative tests of color evaporation: Charmonium production". Phys. Lett. B* **390**, *323*, (1997).

[35] J. P. Lansberg. *"J/ψ, ψ' and Υ Production at Hadron Colliders: A Review". Int. J. Mod. Phys. A* **21**, *3857*, (2006).

[36] N. Brambilla et al. *"Heavy Quarkonium Physics". CERN Yellow Report, CERN-2005-005, 487 pp*, (2005).

[37] E. L. Berger and D. L. Jones. *"Inelastic Photoproduction of J/ψ and Υ by Gluons". Phys. Lett. D* **23**, *1521*, (1981).

[38] E. W. N. Glover F. Halzen, F. Herzog and A. D. Martin. *"J/ψ as a trigger in $\bar{p}p$ collisions"*. *Phys. Lett. D* **30**, *700*, (1984).

[39] R. Baier and R. Rückl. *"Hadronic Production of J/ψ And Υ: Transverse Momentum Distributions"*. *Phys. Lett. B* **102**, *364*, (1981).

[40] P. Artoisenetand others. *Phys. Rev. Lett.* **101**, *15201*, (2008).

[41] E. Braaten and T. C. Yuan. *Phys. Rev. Lett.* **71**, *1673*, (1991).

[42] W. E. Caswell and G. P. Lepage. *"Effective Lagrangians for Bound State Problems in QED, QCD, and other Field Theories"*. *Phys. Lett. B* **167**, *437*, (1986).

[43] P. Cho and A.K. Leibovich. *"Color octet quarkonia production"*. *Phys. Lett. D* **53**, *150*, (1996).

[44] P. Cho and A.K. Leibovich. *"Color-octet quarkonia production II"*. *Phys. Lett. D* **53**, *6203*, (1996).

[45] V.A. Fock. *"The Theory of Space, Time and Gravitation"*. *Macmillan*, (1964).

[46] The CDF Collaboration. *"Υ Production in $\bar{p}p$ Collisions at $\sqrt{s}$ =1.8 TeV"*. *Phys. Rev. Lett.* **75**, *4358*, (1995).

[47] S. Fleming E. Braaten and A. K. Leibovich. *Phys. Rev. D* **63**, *094006*, (2001).

[48] W. J. Stirling A. D. Martin and R. G. Roberts. *"Parton distributions updated"*. *Phys. Lett. B* **306**, *145*, (1993).

[49] A. D. Martin et al. *"Parton distributions: A new global analysis"*. *Eur. Phys. J. C* **4**, *463*, (1998).

[50] The CTEQ Collaboration. *"Global QCD analysis of parton structure of the nucleon: CTEQ5 parton distributions"*. *Eur. Phys. J. C* **12**, *375*, (2000).

[51] H. Fritzsch and P. Minkowski. *"Psi resonances, gluons and the Zweig rule"*. *Nuovo Cim. A***30**, *393*, (1975).

[52] The CDF Collaboration. *"Production of Upsilon(1S) Mesons from chi(b) Decays in p anti-p Collisions at $\sqrt{s}$ = 1.8 TeV "*. *Phys. Rev. Lett.* **84**, *2094*, (2000).

[53] The LHC Study Group. *"The Large Hadron Collider - Conceptual Design"*. *CERN-AC-95-05 LHC*, (1995).

[54] The ATLAS Collaboration. *"The ATLAS Experiment at the CERN Large Hadron Collider"*. *2008 JINST 3 S08003*, (2008).

[55] The LHCb Collaboration. *"The LHCb Detector at the LHC"*. *2008 JINST 3 S08005*, (2008).

[56] The ALICE Collaboration. *"The ALICE experiment at the CERN LHC"*. *2008 JINST 3 S08002*, (2008).

[57] O. S. Brüning et al. *"LHC Design Report"*. *CERN-2004-003-V-1*, (2004).

[58] Lyndon Evans and Philip Bryant (editors). *"LHC Machine"*. *2008 JINST 3 S08001*, (2008).

[59] The CMS Collaboration. *"The Magnet Project: Technical Design Report"*. *CERN/LHCC 97-10, CMS TDR 1*, (1997).

[60] The CMS Collaboration. *"The Tracker Project: Technical Design Report"*. *CERN/LHCC 98-06, CMS TDR 5*, (1998).

[61] W. Adam et al. *"Track reconstruction in the CMS tracker"*. *CMS NOTE-2006/041*, (2006).

[62] The CMS Collaboration. *"The Electromagnetic Calorimeter Project: Technical Design Report"*. *CERN/LHCC 97-33, CMS TDR 4*, (1997).

[63] R.M. Barnett et al. *"Review of particle properties"*. *Phys. Rev. D***54***, 1*, (1996).

[64] The CMS Collaboration. *"The Hadronic Calorimeter Project: Technical Design Report"*. *CERN/LHCC 97-31, CMS TDR 2*, (1997).

[65] The CMS Collaboration. *"The CMS Muon Project: Technical Design Report"*. *CERN/LHCC 97-32, CMS TDR 3*, (1997).

[66] The CMS Collaboration. *"The TriDAS Project Technical Design Report Volume 1: The Trigger Systems"*. *CERN/LHCC 2000-38, CMS TDR 6.1*, (2000).

[67] The CMS Collaboration. *"The TriDAS Project Technical Design Report Volume 2: Data Acquisition and High-Level Trigger". CERN/LHCC 2002-26, CMS TDR 6.2*, (2002).

[68] S. Agostinelli et al. *"G4 - a simulation toolkit". Comput. Phys. Commun.* **A506**, *250*, (2003).

[69] E. Barberio B. van Eijk and Z. Was. *"Photos - a universal monte carlo for qed radiative corrections in decays". Comput. Phys. Commun.* **66**, *115*, (1991).

[70] E. Barberio B. van Eijk and Z. Was. *"Photos - a universal monte carlo for qed radiative corrections: version 2.0". Comput. Phys. Commun.* **79**, *291*, (1994).

[71] The CMS Collaboration. *"Measurement of CMS luminosity. CMS Physics Analysis Summary, CMS-PAS-EWK-10-004*, (2010).

[72] S. Van der Meer. *"Calibration of the effective beam height in the ISR. CERN-ISR-PO/68-31, 250*, (1968).

[73] The CMS Collaboration. *"Performance of muon identication in pp collisions at* $\sqrt{s} = 7$ *TeV". CMS Physics Analysis Summary, CMS-PAS-MUO-10-002*, (2010).

[74] The CMS Collaboration. *"Alignment of the CMS silicon tracker during commissioning with cosmic rays". JINST, 5:T03009*, (2010).

[75] The CMS Collaboration. *"Precise mapping of the magnetic eld in the CMS barrel yoke using cosmic rays". JINST, 5:T03021*, (2010).

[76] The CMS Collaboration. *"Studies of tracker material in the CMS detector. CMS Physics Analysis Summary". CMS Physics Analysis Summary, CMS-PAS-TRK-10-003*, (2010).

[77] The CMS Collaboration. *"Measurement of momentum scale and resolution using low-mass resonances and cosmic ray muons". CMS Physics Analysis Summary, CMS-PAS-TRK-10-004*, (2010).

[78] M.J. Orelia. *"A Study of the Reactions psi prime → gamma gamma psi". Ph.D. Thesis, SLAC-R-236, Appendix D*, (1980).

[79] J. C. Collins and D. E. Soper. *"Angular Distribution of Dileptons in High-Energy Hadron Collisions". Phys. Rev. D* **16**, *2219*, (1977).

[80] The CMS Collaboration. *"Measurement of tracking efficiency". CMS Physics Analysis Summary, CMS-PAS-TRK-10-002*, (2010).

[81] Bora Akgün and Urs Langenegger. *"A study of muon selection efficiency determination with J/ψ and $\Upsilon(1S)$ decays". CMS Note, CMS-AN-09-144*, (2009).

[82] Bora Akgün and Urs Langenegger. *"A study of the muon selection bias and efficiency in J/ψ and $\Upsilon(1S)$ decays". CMS Note, CMS-AN-10-120*, (2010).

[83] CMS Collaboration. *"Prompt and non-prompt J/ψ production in pp collisions at $\sqrt{s}$ = 7 TeV". Eur. Phys. J. C* **71**, *1575*, (2011).

[84] CMS Collaboration. *"Prompt and non-prompt J/ψ and $\psi(2S)$ production in pp collisions at $\sqrt{s}$ = 7 TeV". CMS Note, CMS AN-11-098*, (2011).

[85] The CMS Collaboration. *Performance of CMS Muon Reconstruction in Cosmic-Ray Events, JINST, 5:T03022*, (2010).

[86] CMS Collaboration. *"Absolute luminosity normalization". CMS Detector Performance Summary CERN-CMS-DP-2011-002*, (2011).

[87] J.P.Lansberg. *"Total J/ψ and Υ production cross section at the LHC: theory vs. experiment". PoS ICHEP 2010, 206*, (2010).

[88] ATLAS Collaboration. *"Measurement of the Upsilon(1S) Production Cross-Section in pp Collisions at sqrt(s) = 7 TeV in ATLAS. CERN-PH-EP-2011-083*, (2011).